# Portable Blood Plasma Separation for Point of Care Diagnostics

by

**Tatyana A. Shatova**

B.S., California Institute of Technology (2008)

M.S.C.E.P., Massachusetts Institute of Technology (2011)

Submitted to the Department of Chemical Engineering

in Partial Fulfillment of the Requirements for the Degree of

Doctor of Philosophy in Chemical Engineering

at the

MASSACHUSETTS INSTITUTE OF TECHNOLOGY

June 2015

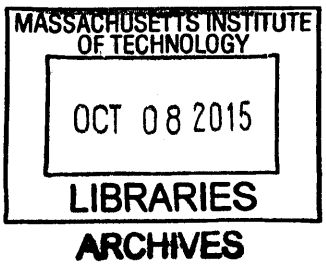




Author ..... Signature redacted

Tatyana A. Shatova
Department of Chemical Engineering
May 22nd, 2015

Certified by ..... Signature redacted

Klavs F. Jensen
Department Head, Chemical Engineering
Warren K. Lewis Professor of Chemical Engineering
Professor of Materials Science and Engineering
Thesis Supervisor

Accepted by ..... Signature redacted

Richard D. Braatz
Professor of Chemical Engineering
Chairman, Committee for Graduate Students

**PORTABLE BLOOD PLASMA SEPARATION FOR POINT OF CARE DIAGNOSTICS**

by

**Tatyana A. Shatova**

Submitted to the Department of Chemical Engineering on May 22nd, 2015 in Partial Fulfillment of the Requirements for the Degree of Doctor of Philosophy in Chemical Engineering

## ABSTRACT

Point of care testing is expanding the healthcare field towards personalized and early-detection medicine. Microfluidic platforms present an opportunity for low cost, portable diagnostic sensors through manipulation of small volumes of fluids on isolated, compact devices. One of the challenges of microfluidic sensors is the biological sample pretreatment steps that are manually performed prior to on-chip loading and sensing. This issue is especially prominent for human blood, which contains about a billion cells in one milliliter total volume. These blood cells can rupture, clog devices, block optical readouts, and foul electrodes. At the same time, the liquid portion of human blood, plasma, is rich in a variety of disease indicators, many of which have not yet been identified, and thus is an essential part in the diagnostic field.

This thesis focuses on the design of a small, around 1 cm long, microfluidic device that separates out blood plasma from undiluted human blood. This design does not require any external field or equipment, beyond a loading syringe and collection tubing. The separation results show 10-100 times improvement in plasma purity over the literature values for passive separation designs. This separation system was then combined with a colorimetric malaria sensor that produced a visually detectable colored result with a 7.5 nM limit of detection in whole blood. This thesis details the design of a low power point of care diagnostic process that is capable of blood processing and detection, and which eliminates the need for any external laboratory-scale equipment. Advantages and challenges of other low power, microfluidic sensor constructs are also discussed.

Thesis Supervisor: Klavs F. Jensen

Title: Department Head, Chemical Engineering
Warren K. Lewis Professor of Chemical Engineering
Professor of Materials Science and Engineering

## ACKNOWLEDGEMENTS

My biggest thank you goes out to my advisor, Professor Klavs F. Jensen. Klavs has been very patient and supportive throughout the years and different research "growth" stages. He has been very generous in allowing me to gradually define the direction of my thesis, and in supporting the exploration of a number of collaborations and project directions. Klavs allows students to go beyond the expected topics within the group, and really explore our research possibilities while providing constant advice and direction. He also prioritizes his availability towards his students, and always has a smile ready for us. Thank you, Klavs.

I have also been very fortunate in being able to work with Professor Hadley D. Sikes on multiple research applications. Her suggestions throughout the years have greatly improved the overall project outcome and have expanded my understanding of the research field. Hadley has been very supportive inside and outside of committee meetings; her optimism and enthusiasm are very contagious, as can also be seen in her group members. I'd like to also thank collaborators from her group: Brandon Heimer, Kaja Kaastrup, and Shefali Lathwal. Professor J. Christopher Love has been a great help in keeping my research goals and experiments in focus of the final outcome throughout the committee meetings. He has given me both large-scale direction suggestions, as well as provided quite a few tips and tricks to help with the small-detail problems when dealing with the subfield of bio-microfluidics.

I would also like to thank T. Allan Hatton for being such an enthusiastic proponent of the Practice School and the department. I have greatly enjoyed the industry experience provided by the program, and have developed life-long friends through the journey. I have also had the great pleasure of teaching assisting his undergraduate transport phenomenon course, where I got to interact and learn directly from him. His positive demeanor and friendly nature can motivate anyone to try their hardest. I would also like to thank Claude Lupis and his wife for providing the students with in-depth industrial advice and for guiding us in how to handle even high-stress professional situations throughout our Practice School experience. And I would like to thank Professor William Tisdale for being a great co-lecturer of undergraduate transport and for being responsive to both TA and student needs. Thank you to a number of people I have gotten to know through these experiences: Adekunle Adeyemo, Flora Cheng, Clare Dibble, Sravani Kanamarlapudi, Agustin Lopez Marquez, Illaria Mori, Kittipong Saetia, Sai Sandeep Tallam, and Matteo Tomei.

A great thanks goes out to Jonathon Weis and the Professor Timothy M. Swager group for the years of collaboration on resistance-based sensor applications. I'd like to thank Vivian Hsieh for being a great friend and for sharing her time and laboratory equipment in the Professor Alan P. Jasanoff lab. I'd also like to thank Stephen Shimizu and Professor Michael S. Strano group for a number of collaborative projects.

I'd like to thank the Jensen group members throughout the years for their friendliness, help, and positivity: Andrea Adamo, Jinyoung Baek, Jerry Keybl, Jen Lee, Kyoungmi Lee, Marcella Lusardi, Shirley Mao, Christopher Marton, Kevin Nagy, Everett O'Neal, Maryam Peer, Maria Jose Remacha, Fumihiro Sassa, Saurabh Shahane, Armon Sharei, Yanxiang Shi, Baris Unal, Nopphon Weeranoppanant, Jian Wen, Lisi Xie, Cuixian Yang, and Nikolay Zaborenko. I'd like to especially thank Yanjie Zhang for being the best office-mate and for all of the graduate school and life advice over the years! I'd also like to extend a warm thank you to Alina Haverty for taking care of our group each and every day. A big thank you to the hard-working undergrads who have helped me along the way, Marissa Engle and Eden Ford.

Also a great thanks to my classmates with whom I have shared the defining years of graduate school, especially Rachel Howden, Vivian Hsieh, Rosemary Kanasty, Cheri Li, Vasiliki Panagiotou, Eric Shiue, Jamila Yamani, Harry Ann, Simon Choong, and many many more. As well as a big thank you for those I've met through Sidney-Pacific and other MIT-avenues. Thank you!

A tremendous thanks to my life-long friends, most of whom I've known and love for more than a decade: Sachit Bhujange, Neha Das, E. Victoria Dydek, Gaurav Giri, Matt Glassman, Robbie Hunter, Jiwon Kim, Alina Kolomeyer, Hanna Komlos, Helen Lee, Eddien Medina, Shuang Meng, Deepak Mishra, Brigitta Miyamoto, Vivek Narsimhan, Askhay Singal, Christine Tung, Esther Wang, Karen Wang, Erin White, Jennifer Yim, Shawn Yu, Tracy Yutko, and more. Love you!

And an especially love-filled thank you to my parents, Irene and Alex, for their support and patience with a chatty-kid like me and for working extra hard to make sure I have every opportunity that I desire as I grew up. Spasibo for your many years of love and care! And a huge thank you to my husband-elect Tom McNicholas for bringing sunshine and love into my life. With you by my side, I've grown happier, warmer, and more confident with each day we spend together!

## Table of Contents

## List of Figures

## List of Tables

# CHAPTER 1. INTRODUCTION

Low power, portable diagnostic devices would advance early detection of disease beyond the hospital and laboratory to the patient bedside. The microfluidic field presents a great opportunity of manipulating small volumes of bodily fluids for both processing and diagnostic applications. Microfluidic devices have the potential to minimize the cost of material, training, external equipment, and provide an isolated environment that can improve reproducibility and minimize false-readouts. By focusing this work on the design of a portable, low power microfluidic device that is able to handle both processing of biological fluids and provide sensing results, we hope to come one step closer to the design of a clinically relevant point of care diagnostic device.

Blood circulates throughout our entire body and is rich in sugars, hormones, proteins, nucleic acids, and other analytes. Each year, the number of known diagnostic biomarkers circulating in the liquid portion of the blood, plasma, increases rapidly. Unfortunately, majority of disease detection systems cannot handle complex biological media, such as undiluted human blood. Blood contains a high density suspension of cells, around a billion of cells in a milliliter of blood. These cells encompass about 40-60% of the total blood volume and are generally in a flux between cell-cell aggregate formations, as well as cell-protein interactions. These cells present a challenge for sensing approaches, because they can physically block optical readouts, foul electrodes and alter readouts, as well as lyse under stress and release a large number of salts, proteins, and analytes.

At the same time, no other biological fluid matches bloods capacity to define the body's response to stress, dehydration, infection, disease progress, as well as treatment efficacy. This thesis focuses on a portable, low-power microfluidic blood plasma separation design which does not require any external field or equipment. The channel design was optimized to temporarily increase and collect the cell-free plasma layer near the channel walls. By studying a range of design angles and features, we present a range of separation values and blood behavior in microfluidic channels and compare them to the literature designs and results. The settings from the most reproducible separation results were then used for hand-driven on-chip blood separation, thus eliminating the need for any external pumps. The numerical methods advantages and limitations for blood behavior on the microfluidic are also

briefly discussed. The final microfluidic separation design produces continuous and high-purity blood plasma. The setup allows for a large range of plasma volumes to be collected, and therefore can be adapted to a wide range of sensor constructs, from small-scale to laboratory-scale.

This microfluidic blood processing component is then applied to a low power, colorimetric sensor of malaria infection, to show the applicability of this blood plasma separation step in point of care diagnostics. This sensing component applies a polymer amplification design to a sandwich enzyme-linked immunosorbent assay, which provides a visually detectable color change for the detection of *Plasmodium falciparum* histidine-rich protein-2. Other microfluidic sensing constructs and channel designs, such as removable microfluidic devices for amperometric carbon nanotube-based sensing, recycle microfluidic setup for hypermethylated DNA sensing, as well as nanopore replications for ion sensing, are also presented in this thesis. By designing a portable plasma separation device, incorporating a colorimetric malaria sensor, as well as discussing the challenges and advantages of a number of low-power microfluidic sensors, we hope to expand the clinical applicability of microfluidic constructs for point of care diagnostics.

# CHAPTER 2. BACKGROUND

## 2.1 Microfluidics

Microfluidic approaches focus on engineering devices that allow for manipulation of small volumes of liquid on the micrometer scale. The engineering of these devices provides an opportunity for miniaturization of complex diagnostic schemes, while minimizing the cost of the process. A subfield of microfluidic research, called micro total analysis systems (μTAS), focuses the design of the device on the elimination of any external or pretreatment steps that would require additional user training, equipment, and time.[1-5] The idea of completing every processing step on-chip aligns favorably with the healthcare advances in personalized diagnostics and treatment. By designing low-power, portable devices capable of processing complex biological samples, while giving an accurate sensor readout, the microfluidic field can be instrumental in expanding clinical approaches to point of care diagnostics.

## 2.2 Macroscale Blood Separation

The laboratory standard for blood separation is centrifugation of the blood sample. Spinning of the sample separates out the cellular components based on their densities, leaving a plasma solution near the top (density of 1030 $kg/m^3$), followed by a "buffy coat" of white blood cells and platelets, and then red blood cells in a high number near the bottom of the sample vial (density of 1050-1100 $kg/m^3$).[6, 7] The plasma is then manually decanted, while leaving the cells behind. This method is mostly used for separation of large volumes of biological sample, a few milliliters or larger, and requires training in both equipment use as well as manual plasma extraction.

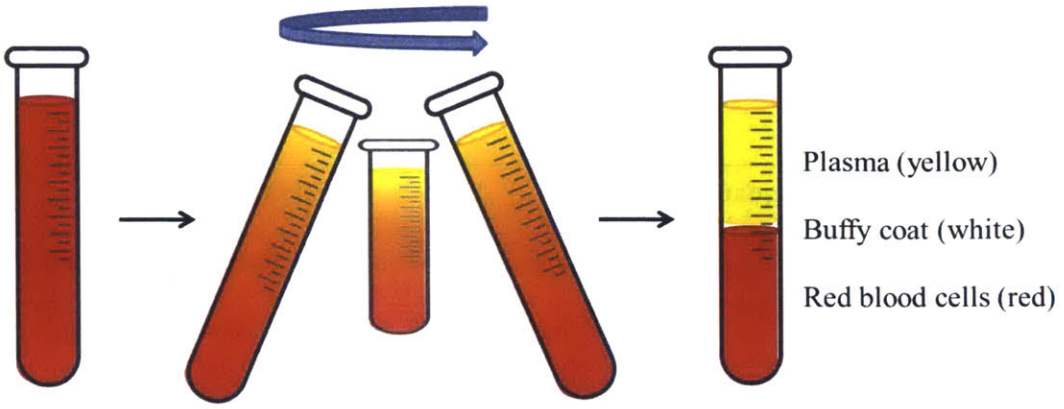


**Figure 2-1** A depiction of blood collected in the test tube, fully suspended on the most left. The blood is then spun down in a centrifuge, which pushes the plasma towards the top. On the right, blood is fully separated with 40-60% by volume plasma (yellow, at the top), less than 1% buffy coat (white blood cells, platelets, depicted in white), and the remaining portion red blood cells (red, at the bottom).

## 2.3 Microfluidic Plasma Extraction

Microfluidic approaches to handling biological fluids are advantageous for multiple reasons: devices can cut down on material, training, equipment, and false-result costs. As microfluidic sensors and other components become clinically relevant in their specificity and sensitivity, handling of biological fluids on-device has grown in importance. Ideally, μTAS can be designed such that all the handling and readout steps are on-chip. This would cut down on device footprint, readout time, training, and overall costs.

### 2.3.1 Evaluation Parameters

There has been a wide range of microfluidic approaches for sorting cells and solids in blood. In order to optimize the plasma for sensing, blood should be minimally diluted or undiluted, well separated, and have sufficient throughput for protein and cytokine sensing. Keeping that in mind, we define key parameters with which we compare our system to the current literature, in Table 2-1. These are the parameters we will use for the rest of the document. Beyond these parameters, microfluidic devices can be further broken down into two categories - active and passive separation. Active separation takes advantage of external

fields that are incorporated with the device; while passive separation takes advantage of the geometry and blood physical properties to encourage plasma separation.

| Term | Equation | Definition |
|---|---|---|
| Inlet cell count | $c_{inlet}$ | Number of cells in the inlet per standard volume. |
| Isolate/Plasma cell count | $c_{plasma}$ | Number of cells in isolate/plasma per standard volume. |
| Blood volume fraction | $V_{blood}/V_{total}$ | The volume fraction of blood relative to the total solution volume. Values range from 0-1. |
| Purity | $\left(1-\frac{c_{plasma}}{c_{inlet}}\right)\cdot 100\%$ | Percentage of cells that is present in the isolate/plasma relative to the inlet. Values range from 0-100%. |
| Isolate/Plasma cell ratio | $\frac{c_{inlet}}{c_{plasma}}$ | Ratio of cells in inlet relative to the isolate/plasma. This expression is similar, but more sensitive than the purity parameter. The larger the ratio, the fewer cells are present in the plasma. |
| Yield | $V_{plasma}/V_{total}$ | Ratio of plasma volume extracted from a total volume of blood injected. |
| Plasma flow rate | $Q_{Inlet}\left(\frac{V_{plasma}}{V_{total}}\right)$ | The plasma throughput of the device, typically given as μL/min. |
| Plasma final volume | $V_{plasma}$ | When the system depends on capillary, electroosmotic, or other very low throughput setups, sometimes only final plasma volume is available. |

**Table 2-1** Relevant evaluation parameters for microfluidic blood plasma extraction.

Beyond these evaluation parameters, it is also helpful to keep in mind the overall volumes of blood that are processed on-chip. Generally the volumes can be broken down into three categories – fingerprick (≤10 μL total blood volume), analytical volumes (1-5 mL), and blood transfusion volumes of around 500 mL.[8] Fingerprick volumes are commonly used for

highly concentrated analytes, such as glucose for diabetes testing, but overall are found to be too small for more rare proteins or nucleic acids that are relevant for most diagnostic applications. These volumes might become more relevant as the sensitivity of sensors is improved upon over the years, but currently volumes larger than 10 μL and even in the ~ mL regimes are most relevant for diagnostic applications. Therefore we focus on blood processing approaches that can be adapted for a range of blood volumes, in order to apply to the largest number of sensor constructs.

### 2.3.2 Active or External Field Plasma Separation Methods

Active microfluidic separation can be further broken down into three main external field approaches - magnetic, electric, and acoustic.[8] Magnetic fields do not require large instrumentation and are independent of solution ionic strength, pH, and surface charges.[9] Red bloods cells' magnetic properties are defined by the state of the hemoglobin within the cells. Hemoglobin carries more than 98% of the oxygen in the blood and is defined by four iron ions. As part of the protein, these iron ions can loosely and reversibly bind to oxygen species ($Fe^{2+}$-$O_2$).[10] If hemoglobin contains oxygen (oxyhemoglobin), then the red blood cells are diamagnetic (non-magnetic) and are weakly repulsed by the magnetic field.[9] In order to manipulate diamagnetic cells or particles, superconducting magnets are required in order to produce really high magnetic forces and gradients. (See Figure 2-2) So far the literature in this field centers around dilute suspensions of polymer particles ($10^5$ particles/mL) [9, 11], dilute cell suspensions in complex paramagnetic mediums [11], and fungi removal from diluted blood using super-paramagnetic beads with antibodies.[12] If however, hemoglobin contains no oxygen (deoxyhemoglobin), then the iron groups contain unpaired electrons and the cells are rendered paramagnetic.[13] This is most often accomplished using either additives and/or using a gas-permeable membrane.[8, 14-16] Even with additives, the method applies to blood with at most 0.1 blood volume fraction, features slow flow rates on the order of μL/hr, and produces purity of only up to 94% (16.7 plasma cell ratio) with no defined yield. [15, 16] Overall, the literature on microfluidic magnetic separation is very limited.

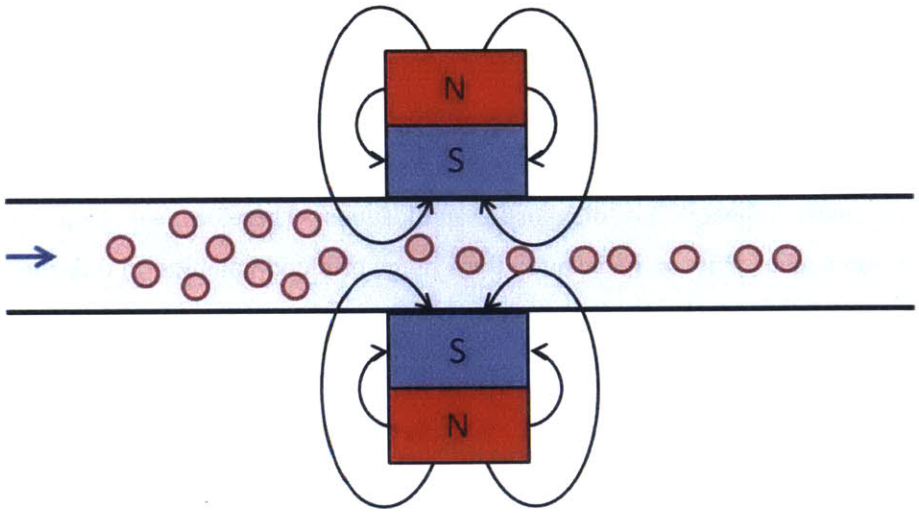


**Figure 2-2** A depiction of a channel experiencing a magnetic field due to the presence of two magnets. The particles flowing down the channel, depicted in pink, are assumed to be diamagnetic and therefore are repulsed by the magnetic field. This is a typical scenario for oxygenated red blood cells. If the cells are deoxygenated, the red blood cells would in turn be paramagnetic and therefore would be attracted to the magnetic field. In that case, the opposite behavior would be expected. Blue arrow indicates flow direction in channel.

Electric field separation is commonly applied in the microfluidic field for DNA or protein focusing and separation.[17] This type of separation can be broken down into two main categories: electroosmotic flow and dielectrophoretic separation. Electroosmotic flow (EOF) occurs when a potential is applied across a channel. The charges in the electric double layer (Debye layer) near the charge channel surface begin to move due to this applied potential, and this in turn causes solution flow. (See Figure 2-3) This effect most significant in small channels, therefore majority of the blood work in this field features blood volumes on the order of hundreds of nanoliters, and low blood volume fractions (around 0.0625).[18] This flow effect is not sufficient to create separation on its own. In order to create separation between the cells and solution, small side channels (perpendicular to the potential) were incorporated. Thus in effect, this approach took advantage of EOF and plasma skimming methods which will be discussed in more detail below.

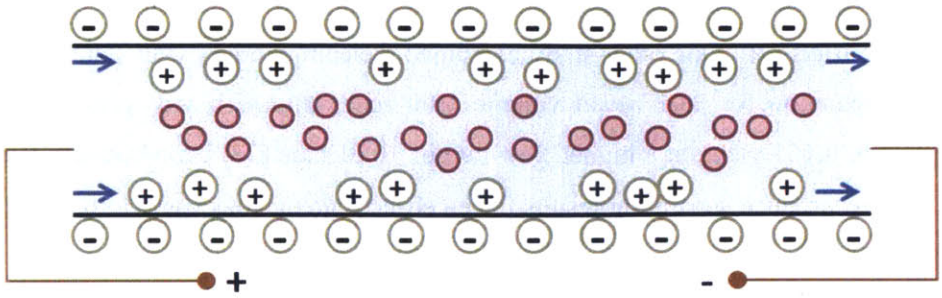

**Figure 2-3** A depiction of electrosmotic flow in a glass channel filled with ionic solution and particles or cells. The movements of positive ions (indicated by blue arrows) that collect near the negatively charged surface drag the rest of the solution in the channel.

Dielectrophoresis, on the other hand, induces movement of neutral particles through the interaction of a nonuniform electric field and the corresponding induced particle polarization. (See Figure 2-4) This nonuniform field is achieved by incorporating electrodes of non-equal shapes, or by incorporating insulating components into the channel - such as posts or other obstacles.[19, 20] In order to separate the particles from their surrounding medium, the particles need to be less or more polarizable than the solution (experience a different permittivity).[20, 21] Permittivity can strongly depend on the electric field frequency.[22] In the case of red blood cells and plasma, the cells have a lower permittivity than plasma and therefore cells move towards a weaker electric field. The most recent example of plasma extraction also featured finger-prick volumes of blood (5 μL), 0.11 blood volume fraction and yielded 300 nL of plasma overall (0.06 yield) with 97% purity (33.3 plasma cell ratio).[22] Another study combined dielectrophoresis with capillary action, therefore again focusing on very slow flow rates (varied blood velocity depending on the capillary drive, on the order of ~ μm/s), but was able to produce 89% pure plasma, with a high 0.28 yield for minimally diluted blood.[23]

Majority of blood work with dielectrophoresis focuses on separation of platelets, cancer cells, or other cell types from other blood cells and is not generally applied to plasma separation. This approach is more advantageous for separation between different cell types using the differences in their permittivity. Most of the time, blood is significantly diluted (~0.05 blood volume fraction) using controlled conductivity buffers.[24, 25] Usually dielectrophoresis is combined with one or more pumps or capillary action to drive the flow. One study combined both dielectrophoresis and elecroosmotic flow, but again much progress needs to be made

before it can applied to plasma separation instead of diluted suspensions of cells in low conductivity buffers.[26] One other study combined dielectrophoresis with slanted obstacles to provide separation for 0.01 blood volume (100 times diluted blood) giving 94% pure diluted plasma, 0.165 yield, at a higher flow rate of 10 μL/min.[27] Unfortunately the group was not able to produce separation results once cell-cell interactions came into play for less diluted blood.

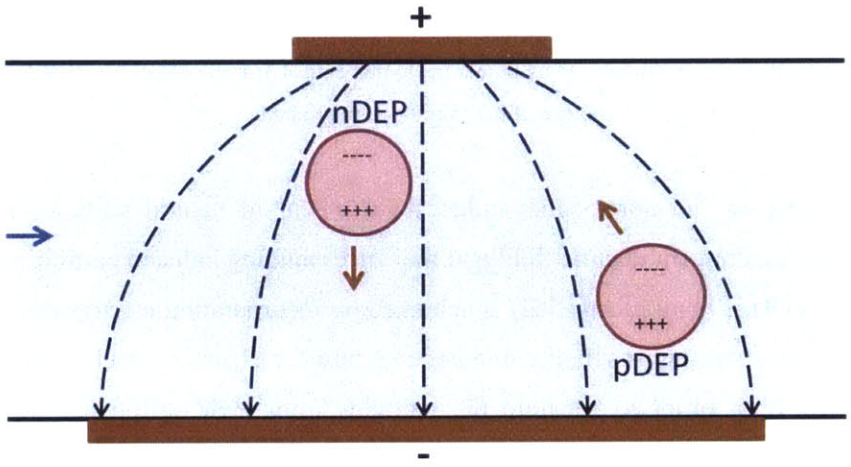


**Figure 2-4** A depiction of dielectrophoresis in a channel. Dielectrophoresis takes advantage of momentary induced dipoles in neutral particles. If the particle has a higher permittivity than the surrounding solution, then positive dielectrophoresis (pDEP) occurs, as depicted, and particle moves towards the stronger electric field. If the particle has lower permittivity than the surrounding solution then negative dielectrophoresis (nDEP) occurs, as depicted, and the particle moves towards the weaker electric field. Red blood cells generally have a lower permittivity than plasma or plasma diluted with PBS. Blue arrow indicates the flow direction, while orange arrows indicate net force coming from the electric field.

Acoustic cell separation in microfluidics, or acoustofluidics,[19] takes advantage of ultrasound standing waves (>MHz) that exert radiation forces on cells.[28, 29] These forces, from high intensity ultrasound waves, tend to present themselves in terms of vibration and pressure fluctuations across the channel.[30] Acoustic separation evolved from the ideas initially presented in the optical tweezers field, but requires ~$10^6$-$10^7$ smaller power density and the ability to focus many cells, instead of just one.[31] The force is inversely proportional to the wavelength, is proportional to the square of the pressure amplitude and volume of particle; the force is also dependent on the particle shape, density, and compressibility.[20] Particles that are more dense and less compressible than the surrounding liquid will move towards the pressure nodes, while particles that are less dense and more compressible than

the surrounding liquids will move to the pressure maximum. Therefore red blood cells are pushed towards pressure nodes, which are usually designed to be in the center of channels when the wavelength of the wave is equal to twice the channel width. (See Figure 2-5) If there are lipid vesicles in solution, they would then move towards the pressure maximum points near the channel walls.[32] The concentration of red blood cells near the center creates a cell-depleted region near the walls of the channels, and thus plasma can be collected by splitting the channel into three smaller channels. This approach however, can only handle about 5-10% of cells by volume before the focusing is very limited. Thus there are several approaches that have been developed in order to work around it. The most notable approach features sequential removal of concentrated red blood cells from the middle of the channel by the addition of small vertical channels near the pressure node. This setup has resulted in undiluted blood being separated at 20% yield, with plasma flow rate of 10 μL/min, and 100% purity, or more accurately 1000 plasma cell ratio, which is some of the best results in the field.[29] There are, however, a few issues with using acoustophoretic focusing. For one, the piezoceramic transducers tend to heat up and heat the glue and material that is used to attach them to the microfluidic devices. Thus oftentimes, water cooling, fans, or other cooling systems are incorporated with the microfluidic devices.[30] At the very least, a thermocouple or a visual temperature sensor should be incorporated into the device. Air bubble cavitation is another possible problem in acoustophoretic microfluidic devices. Although at high frequencies typically applied in these systems (>MHz), this is less likely, any gas in the solution and/or irregularities in the channel surface can encourage the formation of bubbles that can then grow and disrupt the standing waves, or worse - rupture cells. This effect is much more likely to occur at pressure antinodes (maximum pressure regions), and thus cells are protected by concentrating near the pressure nodes. [30]

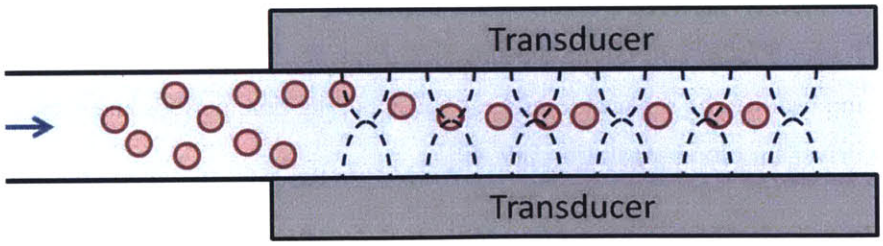


**Figure 2-5** A depiction of acoustophoretic focusing in a channel. Because red blood cells are more dense and less compressible than the surrounding plasma, they will migrate towards the center of the channel. Blue arrow indicates the flow direction.

An adapted rotation controller can also be applied for microfluidic devices featuring centrifugal separation. This construct often features a design with an overall CD-type profile. This approach has been added into the active separation section because it features a miniaturized version of the centrifuge behavior used in the hospital or laboratory setting. The behavior is the same as seen on the macroscale, with the more dense objects moving towards the outer edge of the CD while the blood plasma would stay relatively near the center. The separation component is one of the more natural features of the setup; the complexity arises in either plasma extraction or in incorporation of sensing components and valves on chip given that the centrifugal forces is the only driving force for the system.[8, 33-35] Surprisingly, few systems fully characterize the plasma purity as well as the cell health (lysing) in the system, majority focus only on the sensor design and characterization.[8, 33] The best literature values for this system feature a 33% yield of plasma from 150 μL of blood followed by subsequent virus detection, without mention of plasma purity; another study features processing of 2 mL of blood in 2.5 min to produce 99.9% pure plasma with no mention of yield.[36-38] Both of these methods do not characterize any cell lysing, and have shown images of pink plasma, although it is unclear if that is due to blood aging or due to device-induced lysing.[8]

### 2.3.3 Passive Plasma Separation Methods

Passive methods focus on separation that requires no external field, and can be broken down into the following categories: sedimentation or gravity methods, filtration methods, obstacles or cell deviation methods, curved channels methods, and straight channels methods.[8] Sedimentation methods are the most elementary and take advantage of gravity and the difference in density between plasma and blood cells, 1030 $kg/m^3$ and 1050-1100 $kg/m^3$ respectively. (See Figure 2-6) Given the slow sedimentation rate, 0.27 – 3.8 μm/s (depending on gender and health), the separation process requires long time periods and therefore cannot be the sole driver for blood separation.[39, 40]

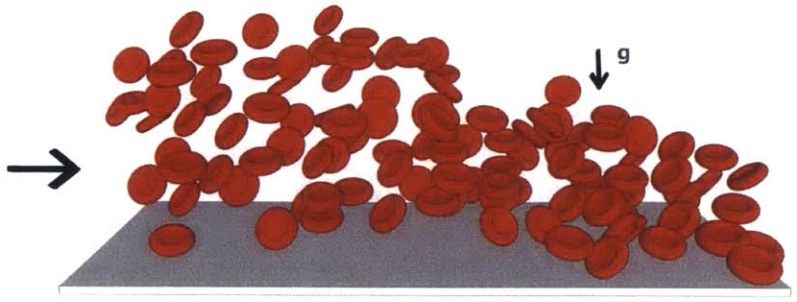


**Figure 2-6** A depiction of blood sedimentation, where cells move downward with the force of gravity.

Sedimentation is occasionally combined with other passive microfluidic methods, such as filtration or plasma skimming. Filtration can be broken down into two types: dead-end filtration that has a filter across the channel perpendicular to flow, and cross-flow filtration that has filters that are parallel to the channel and the flow direction. (See Figure 2-7) In order for filtration to be effective, the filter pore dimensions need to be around 1 μm or smaller, otherwise the very flexible red blood cells, which are around 8 μm in diameter and 2 μm in thickness, will be able to squeeze through the filters. This size limitation and the requirement of uniform pore formation, in order to ensure no red blood cells can squeeze through, increase the complexity of fabrication of these devices, and can cause increased cell lysis due to shear rates present against the cells at the filter region. Moreover, filters have a large surface area that interacts with blood, thus could increase the rate of nonspecific protein adsorption and loss.[41] The high number of cells in blood ($10^9$ cells/mL for red blood cells alone) limits the applicability of dead-end filtration due to the very quick fouling of the membrane, possible cell lysing, and requirement for frequent flow reversals in order to clean the filter. Some of the more recent work features filters that are either purchased or laser cut in lab before being incorporated into the channel construct, to cut down on cost of fabrication. Currently, even if whole blood is injected into the filtration device, a wash buffer is required in order to increase the volume of plasma that is filtered and collected, thus effectively diluting the blood. Fluid leakage around the filter is a factor noted in multiple publications and should be kept in mind.[8, 41]

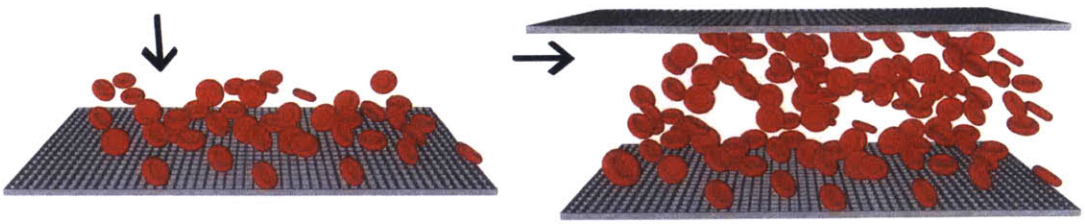

**Figure 2-7** A depiction of dead-end filtration (on the left), where the flow is perpendicular to the filtration membrane; and cross-flow filtration where flow is parallel to the filtration membrane (on the right).

Current literature of dead-end filtration features at most 0.167 blood volume fraction for a range of filters from 0.4-3 μm.[42] At the smallest pore size, 98% purity was achieved (50 plasma/isolate cell ratio) for a 23% yield. Blood was manually injected, while the wash solution was injected on the order of 200-500 μL/min. The system however was limited by fast clogging after 55 μL of plasma was collected. Chromatography paper was used for larger pore sizes filters. The paper allowed for longer device lifetime, but the purity quickly dropped to around 75%. Setups with similar pore sizes as well as the addition of latex microbeads, of 1-6 μm in diameter, for increased separation, have been presented, but show limitation of 0.1-0.3 blood volume fraction, and a maximum of 100 μL of solution processed by capillary force.[43] This system was also limited by volume processed and suffered from low purity at the 0.3 blood volume fraction.

Most recently, a group minimized the dilution of blood needed by combining dead-end filtration with sedimentation. In this setup, the blood is drawn up a vertical channel with a filter on top.[44] The flow rate is driven by initially degassing the channel, and the dimensions were optimized such that gravity plays a significant role against fluid drag and so that the red blood cells do not create a foul layer against the filter. The group was able to produce plasma at a rate of 0.12 μL/min in the first 20 minutes, for up to 0.9 blood volume fraction. The plasma fraction was approximated to be 0.2, although is it unclear for which blood volume fraction exactly.

Cross-flow filtration, which features a filter parallel to flow, can improve device lifetime and is generally preferred in more recent microfluidic approaches. This method allows for easier filter clean-up through the use of pulsating flow, for example, and takes advantage of some of the hydrodynamic forces that decrease the number of cells along the sides of the channel. This approach is also often run in parallel in order to increase the surface area of filters. Even

in parallel, this setup can suffer from low plasma fraction, on order of 0.003-0.009 for 0.45-1 blood volume fraction, and still suffers from short term clogging after around 50 nL of plasma is collected.[41] The purity is often assumed to be 100% for the filters with featured sized less than 1 μm and thus is not measured. Another group has increased the lifetime of the cross-flow filtration with 0.5 μm filter pores by parallel cycles of back pulsing to encourage removal of red blood cells and platelets (back-pulsing for 100 ms every 3 seconds for RBCs and for 5 seconds every 2.5min for platelets).[45] This increased the device lifetime for up to 1 hour, and has produced 8-14% plasma fractions for 0.71-0.24 blood volume fraction, respectively. Purity was again unclear, but assumed to be close to 100% due to the filter. The plasma flow rate is about 0.65 μL/min, although the flow rate decayed by about 45% in the first hour. Thus, even though this flow rate is significantly higher than other cross-filtration methods, it could be improved upon when compared to other methods. One method took advantage of a high parallel setup featuring 32 channels and produced consistent flow rates and minimal cell lysis for over 2 hours by soaking the devices and membranes in an anticoagulant, sodium heparin, as well as by adding significant anti-coagulant to blood to reduce coagulation and viscosity.[46] This setup produced 1-4 μL/min of plasma for 0.48-0.85 blood volume fraction, respectively. Unfortunately, all of the separation for this last study was done with sheep blood, which as the publication mentioned, features significantly different rheology and cell size (red blood cells in sheep blood have a diameter of around 4.8 μm).

Instead of fabricating filters along a channel, a few research groups studied the use of obstacles to deviate blood cells from plasma collection. In this setup, often coined deterministic lateral displacement, an array of pillars is fabricated such that each row is offset by a critical distance in order to create an asymmetric split at each obstacle. This is often designed such that large particles flow in a straight line while small particles zig-zag away. Similarly, slanted vertical weirs can be implemented such that large objects, such as cells, prefer a different path from plasma. Unfortunately, due to the high cell fraction in human blood, as well as the extreme deformability and small sizes of red blood cells, these applications are very limited in blood separation. Similarly to dead-end filtration, most of the applications feature complex fabrication steps requiring exact feature sizes, very high dilution numbers, very slow flow rates, and are prone to clogging.[8, 47] One work features a cascade system for 1 μL/min injection of undiluted blood in parallel with buffer sheath flow, which

visually shows pure plasma, but does not specify overall yield.[48] This procedure is more often applied to cell trapping of various cancer cells, which allow the majority of easily deformable red blood cells to move through while catching bigger, less flexible, rare cells.[7] Because size and deformability between white blood cells and cancer cells (or circulating tumor cells) tends to overlap, others have also incorporated antibody capture along with deviation methods in order to improve specificity.

Another passive separation method is a based on microfluidic channel hemodynamics, which incorporates inertial, viscous, cell-cell interaction, cell-protein interaction, and other forces stemming from the channel geometry, flow, and blood component interactions. Inertial vs. viscous effects can be characterized by the Reynolds number[49, 50]:

$$Re = \frac{\rho \cdot U \cdot D_H}{\mu} = \frac{\rho \cdot Q \cdot D_H}{\mu \cdot A} = \frac{\rho \cdot Q \cdot 2}{\mu \cdot (w + h)}$$

**Equation 2-1**

where $\rho$ is the solution density, $U$ is the average velocity, $D_H$ is the hydraulic diameter, which for a rectangular channel is $D_H = 2(w \cdot h)/(w + h) = 2 \cdot A/(w + h)$, where w is the width and h is the height, and A is the cross sectional area, $\mu$ is the solution viscosity, and $Q$ is the volumetric flow rate. Reynolds number can also be interpreted as the ratio of Re=inertial forces/viscous forces. Therefore, for Re>>1 inertial forces dominate, and for Re<<1 viscous forces dominate the system, even within the laminar regime that is generally present in microfluidics due to the small length scales of the system. One caveat that should always be kept in mind for our system is that blood is shear thinning for shear rates below 100 $s^{-1}$ or for diameters of 300 μm and smaller, therefore the apparent viscosity of blood decreases with increased flow rate until it plateaus at higher flow (and shear).[51] Despite this, we can still categorize the extremes of Reynolds numbers to discuss the dominant regimes.

For Re<<1, we are in the capillary (or Stokes) regime with very slow flow rates (small $U$ and small $D_H$). This regime would lead to slow throughput, and would most correlate with the sedimentation approaches mentioned previously. Particles of the same density and viscosity are observed to enter and leave the channel with the same configuration, as was seen in 1961, unless there was enough time for sedimentation to play a role.[51] However, as the flow rate was increased (and therefore the Reynolds number went up to 10-200 (or Re>>1), inertial forces began to dominate over viscous forces and for tubing diameters of similar order of

magnitude to particles, there was observed a thin annular region where particles collected.[51] Within this regime, there have been observed two types of behavior that depend on the relative size of the particle and the channel hydraulic diameter.[52] For particles that are much smaller than the channel dimension, neutrally buoyant particles move along with streamlines and leave the channel in the same configuration as they came in (assuming no other particle-particle interactions are at play). But as the particle size and channel dimension get closer (particle/channel dimensions of around 0.01-0.1), both rigid and deformable particles were observed to cross the streamlines and to equilibrate in an annulus or at four positions when the channel is rectangular.[52] This phenomenon is attributed to a balance of shear/inertial and wall lift forces. The shear force is pushing particles towards the wall (or towards lower shear rate) due to the parabolic flow profile, and the wall lift is resulting from the particle's wake and is directed away from the wall.[8, 53] At these high flow rates, the phenomenon does not seem to depend on particle rigidity or density, and sorting is mostly accomplished based on size.[52] This method, however, is limited to very dilute cell suspensions (blood volume fraction of around 0.02) or else other factors begin to dominate and the inertial sorting is not the only separation factor.[52] Also, most of the inertial focusing features channel sizes that are 10-100 times bigger than the cell-diameter and therefore does not feature steric-effects which also encourage cell movement towards the center of the channel.

The complex behavior of blood in smaller channels was initially seen *in vivo* in 1933 when blood viscosity of a large artery as well as small arteries that branched off the main artery in a canine hind leg was studied.[54] The group observed that the number of cells in the small branched arteries was much smaller than initially predicted. This work was the initial motivation for a large number of microfluidic devices that mimicked this type of branching profile, and termed it either "plasma skimming" or Zweifach-Fung bifurcation effect.[55] It was only recently that this bifurcation effect was proven to be driven by the same forces that were attributed to the plasma skimming methods, and it was shown that the distribution of blood cells in the channel is the main drive for the bifurcation effects *in vitro* as well as *in vivo*.[55] The plasma skimming term comes from the cell free region that forms near the channel walls, and therefore the plasma can be "skimmed off" the sides of the channel. (See Figure 2-8) The cell distribution in the channel can be partially attributed to some of the inertial separation forces described above, but the system quickly becomes a lot more complex due to such strong deformability of the red blood cells, cell-cell interaction, cell-

protein interaction, and also the high density of cells present in solution. The state of numerical analysis for blood flow behavior in a microfluidic channel is discussed in further detail in later chapters.

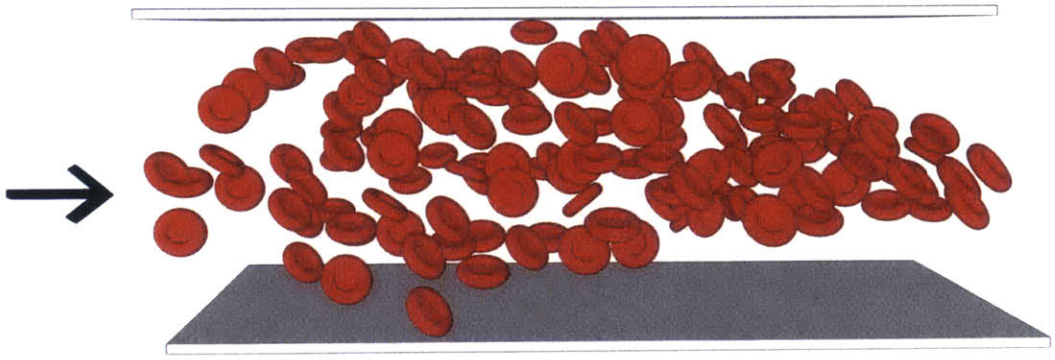

**Figure 2-8** A depiction of the development of the cell free layer near the channel walls (red blood cells moving towards the center of the channel). The arrow indicates solution flow direction in a channel.

Early literature focused on 10-20 times diluted blood (0.05-0.1 blood volume), slow flow, and only visual analysis of blood plasma.[56-59] More recent literature focused on higher flow (30-2000 μL/min) and featured undiluted blood plasma separation, although only producing 31-67% plasma purity (1.4-3 times isolate cell ratio).[60, 61] One literature study stands out in providing around 99% purity (~100 isolate cell ratio) for undiluted blood with a 0.05 yield by incorporating a constriction – expansion channel profile and thus temporarily improving the cell free region.[62, 63] Unfortunately, the improved separation was offset by smaller channels, on the order of 10 by 10 μm, and clogging was consistently reported as an issue after only a few experimental runs. This clogging is mostly likely due to high shear rates and possible aggregations in long small channels. Therefore, improvement in separation as well as the minimization of clogging is still a goal within this sub-field. Overall, the high deformability of red blood cells and the complexity of cell aggregation present an opportunity for further understanding of blood flow behavior and for passive plasma separation approaches.

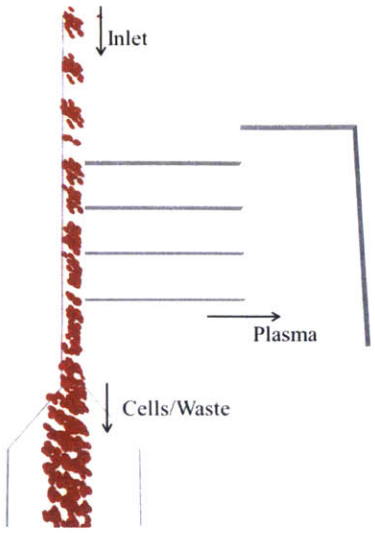


**Figure 2-9** A depiction of a plasma skimming device. A small "constriction" channel, often around 10-30 μm in size, develops a cell free layer depicted in the previous figure. If the flow rate is very slow, cell aggregates can also be seen. The plasma near the walls is "skimmed off" using small side-channels, while the rest of the blood is discarded.

Beyond the inertial and plasma skimming focusing, a secondary flow can be added by designing microfluidic channels with curvature. These secondary recirculation areas arise due to the fluid near the center of the channel moving faster when compared to the fluid near the walls.[8, 64-66] There is a balance between centrifugal forces due the curvature which forces more dense particles towards the outer wall and the recirculation areas which can add additional mixing or alter the separation. In general, the recirculation areas are quite interesting for particle separation in very dilute systems or for isolation of rare cells, but suffer greatly for dense suspensions, like blood. One study did feature trapezoidal cross-section of channels in order to create more room for a large number of red blood cells, but the work focused on white blood cell separation in 0.025-0.05x blood volumes (20-40 times diluted blood).[64] Majority of the literature was only able to show blood plasma separation for 20-100 times diluted blood (0.05-0.01x blood volume), with minimal discussion of plasma purity.[65] There has been some improvement in separation for minimally diluted blood, but additional forces were implemented, such as sedimentation (thus very slow flow rates), or cross-flow filtration steps using pillar arrays (spaced 1.7 μm apart) in order to improve the separation values for 12-20 times diluted blood.[66, 67] Dean's flow and filtration/pillars method produced very high plasma yield of around 50%, but had the issue of

clogging or bubble-trapping which would often lead to flow reversal and loss of separation, as well as required complex fabrication methods.[66]

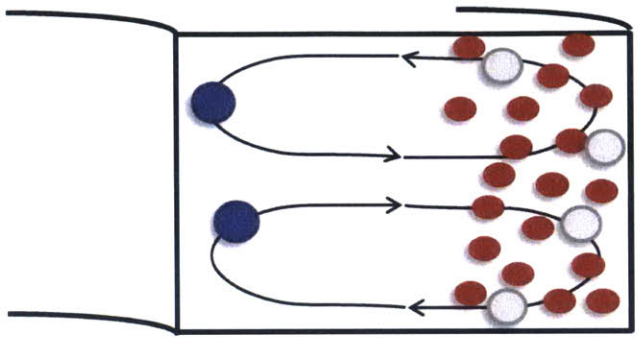

**Figure 2-10** Cross-sectional view of a spiral/curved channel. These channel curvatures create secondary flow patterns (Dean's flow) that can be used to separate out large particles such as circulating tumor cells (CTCs, blue). By adjusting inertial and Dean's flow forces, one can also separate out white blood cells (white), or separate out the plasma away from all cell types. The balance of these forces is hard to optimize once there is cell-cell interaction present and literature plasma separation relies on heavy dilution.

Paper-based blood separation is a common method for both glucose and pregnancy sensors.[8] Interestingly enough, red blood cells are small enough to go through the chromatography paper pores, which is one of the most common paper-sensor materials. Therefore in order to separate out the blood plasma by capillary forces, these paper sensor devices are spotted with coagulating agents which create cell aggregates that cannot penetrate the paper.[68] Other paper materials or the addition of wax can create interesting hydrophobic vs. hydrophilic regions and can allow for filtration or capillary wicking of blood plasma, but all of these methods can only handle very small volumes of blood, around 10 μL, with significant plasma loss as it wicks through the paper into the reaction zones.[69, 70] Therefore the majority of paper sensors for whole blood focus on analytes that are present in high concentrations, such as sugars, albumin, or other abundant factors. Over time, improvement in paper colorimetric sensor sensitivities and other methods could significantly expand the applicability of this approach.

## 2.4 Protein Sensing

Point of care protein sensing is based on the concept of disease detection at the patient bedside, ideally requiring only low power and minimal equipment for analysis. The two main categories for sensing can be broken down into optical and electrical approaches, both briefly discussed below.

### 2.4.1 Optical Sensing

A wide variety of sensors are available for measurement of biological compounds in blood and in interstitial fluids. The laboratory standard is the enzyme-linked immunosorbent assay (ELISA) which uses a variant of an antibody-antigen binding with a second antibody or substrate that is labeled to be fluorescent or chemiluminescent.[71] This is one of the most sensitive assays and it can measure presence of certain antibodies or antigens down to pico- to atto-molar range, depending on the strength of the antigen-antibody binding, the presence of other proteins in solution, and the complexity of the labeling and readout technique. This assay, however, requires training, time, and external instrumentation to measure absorbance or fluorescence.[60, 71] In microfluidic ELISA approaches, the channel is often peeled away from the sensor region in order to allow for fluorescence measurement, or if the channel is not removed, additional amplification steps using beads or other particles are applied to produce a detectable signal.[59, 72]

Current work centers on devising sensing schemes of comparable ELISA sensitivity but involving fewer required readout equipment, and limiting reaction time.[73, 74] More specifically, colorimetric amplification systems featuring nanoparticles, enzyme-linked amplification, and polymer amplification systems are of particular interest for portable protein sensing approaches.[74, 75] Among these methods, the polymer amplification system features a much more rapid sensing response, cutting down the detection step from around 30 minutes, down to about 3 minutes.[75-77] This decrease in sensing time minimizes the burden of the additional amplification steps beyond the sandwich ELISA system, thus proving truly advantageous due to lower overall sensing time and minimal external readout equipment required.

In parallel to these sensing schemes, there has also been a significant amount of work focusing on adapting cell phone cameras for result capture and analysis.[76, 77] By optimizing the light-emitting diode (LED) or lamp sources, controlling the manual camera settings, and capturing the image at a specific distance and angle, multiple colorimetric schemes have been adapted to the use of cell phone cameras.[78-83] By taking advantage of amplification schemes and cell-phone camera improvements, the optical sensing approach can move beyond the laboratory or hospital to portable sensing and analysis even in rural areas. There has been some work focusing on enzyme-amplified c-reactive protein (CRP) sensing in 96 well plates which were captured using a cell-phone camera; as well polymer amplification methods which allow for quicker colorimetric detection, also captured on cell-phone cameras.[75, 76, 84] The enzyme-linked horse-radish peroxidase (HRP) enzyme method is a more established approach for laboratory ELISA readouts, but features longer reaction and binding times when compared to polymer amplification procedures. Therefore both methods are of interest.

### 2.4.2 Amperometric Carbon Nanotube Sensing

Electrochemical and amperometric sensors have the possibility of providing real-time, label free and reversible responses.[85-90] Many of the low power sensors suffer from sensitivity issues since biological entities are on the nano- to micro-meter scale and the electrode's speed and resolution is inversely proportional to the electrode radius.[91, 92] This problem, however, is overcome with inorganic and organic semiconducting nanowires or nanotubes. The advantages of such an electronic circuit are that the diameters of nanowires (NW) and carbon nanotubes (CNT) are of comparable size to biomarkers that are measured and the surface to volume ratio is high.[86, 91, 93-96] Furthermore, most of the biological interactions are based on electrostatic attractions and both NW and CNT protrude from the surface and can be fully exposed in solution.[86, 91, 97] NW and CNT are 1-D electronic conductors and any surface interaction with a biological entity significantly changes cross-sectional conduction property of the material, allowing this to be one of the few setups of sufficient sensitivity for this biological interaction, without the need for amplification steps.[89-91, 94, 97]

Most of the biological molecules are charged at a biological pH. The interaction of these biomolecules with the semiconducting material changes the charge distribution on the CNT, and thus changes the overall conductance of the CNT or NW.[90, 91] This change in conductance can theoretically be sensitive enough to measure interaction between single molecules. Both NW and CNT have proven to have flexible and wide concentration ranges for sensing of biomolecules.[92] And through incorporation of many such distinct sensors involving different receptors in a microfluidic device, the system can measure the presence of multiple biomarkers in solution.[86, 97] More recently, however, it has been observed that the conductance changes in the same direction, no matter what the charge of the protein is in that solution with a specific pH value.[98] Therefore, this interaction has recently been called into question and further study of the CNT-protein interaction would improve the design of CNT-based sensors.

CNT have grown in popularity as a material for biological sensing over the past decade due to further understanding of the chemistry and improved synthesis methods. CNT conductivity depends on the nanotube chirality, and can be semiconducting or metallic.[91] Usually both forms are present after synthesis, and currently separation is very hard and thus expensive. CNTs can also be purchased commercially. Chemical vapor deposition (CVD), which bases the tube diameter on the diameter of the catalyst, has been applied for CNT study or sensing when a more precise control of CNT type and behavior is required.[99] These systems produce an isolated CNT-protein signal, but are burdened with higher production cost when compared to purchasing a mixture of CNTs commercially.[98, 100] If a sensing scheme uses a mixture of commercial CNTs, the sensor has to be calibrated each time due to possible variation in the system conductivity levels.[91, 101]

In order to minimize cost and provide a disposable sensor, modification of commercially available CNTs is of interest for sensing approaches. There are multiple gas sensor constructs that take advantage of either mechanical or liquid deposition of CNT meshes, which produce an aggregate signal.[102, 103] Therefore, applying CVD-grown CNT sensing approaches to these simple CNT sensor fabrication methods is of interest and is pursed further in this thesis. Another aspect of CNTs to keep in mind, however, is the strong variation in amperometric sensing capabilities with salt content of solution due to ionic effect on the electric double layer (Debye layer). The double layer can screen any charged interactions, requiring

significant dilutions of biological materials. Optical sensing approaches do not have this challenge.

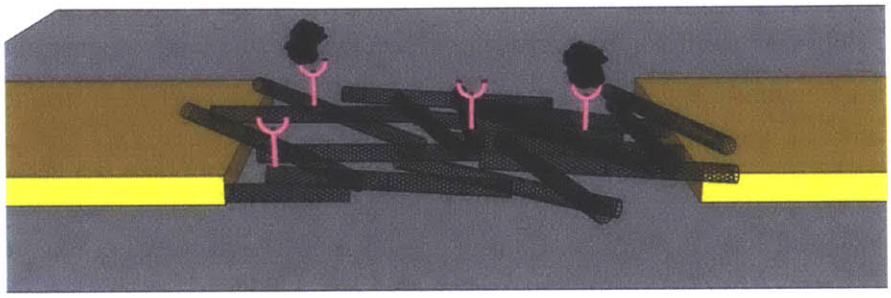

**Figure 2-11** A depiction of a mesh of functionalized CNTs between a pair of electrodes. Aggregate amperometric signal is measured.

It has also been observed that the interaction of the electrodes with the CNT (Shottky barrier) or directly with the proteins can alter the signal significantly or even dominate the system, as well as provide large areas for nonspecific binding.[90, 104-107] Thus, isolating the electrodes themselves, as well as the CNT-electrode interaction, is advantageous for the detection of the specific CNT-protein interaction. The microfluidic system is advantageous since the channel can be designed to physically block every region except the CNT-protein region, or a sheath buffer flow can be added to eliminate any protein presence near the sensor edges.[108, 109] The laminar flow regime in microfluidic devices minimizes diffusion across streamlines and finite element modeling can guide the design of optimal flow ratios between sample and sheath flow so that the protein is only able to interact with the CNT region, but does not get diluted.[107, 110, 111]

Beyond the device design, the sensor scheme needs to be optimized in order to feature specific protein responses. The antibody-protein interaction is one of the most specific and strong interactions available in biology, and is of particular interest. The antibody can also possibly be replaced with a cheaper, smaller, but possibly less specific aptamer component.[91, 92] The CNT sensor of interest can be functionalized by either covalent or noncovalent methods, taking into account that the distance between protein and CNT surface, spacing of the linkers, and modification of the CNT-charge distribution can all play a role in sensor response.[89-92, 98, 106, 112] Of specific interest is capturing the balance of nonspecific vs. specific interactions using noncovalent modification of the CNT surface by

modifying a triblock copolymer itself with the antibody of interest. This allows for CNT coverage to block nonspecific binding while also encouraging a specific antibody-protein interaction (or the model avidin-biotin interaction).[98, 106, 113, 114] In this CVD-grown CNT sensor study, the presence of 100 nM avidin in diluted 10 mM phosphate buffered saline (PBS) led to a significant signal response, for a biotin-modified Tween 20 triblock copolymer. The system also resisted nonspecific binding up to 1 μM protein concentration.

# CHAPTER 3. SYSTEM STABILITY FOR PLASMA SKIMMING DESIGNS

Microfluidics provides an enclosed, small-volume system that has the possibility of improving behavior and reproducibility, due to significant system isolation within the device. One of the biggest challenges in these systems, however, is the connection between the small device and the external equipment, tubing, and other components. Outside of focusing on minimizing the overall device and connections footprint, it is also important to ensure that any variation in sample loading, or solution-surface interaction does not lead to readout noise that dominates the results. We chose to develop the microfluidic devices using photolithography fabrication methods and polydimethylsiloxane (PDMS) polymer devices. This approach allows for a large number of device designs to be incorporated onto one master, which could then be reused to produce polymer PDMS designs. PDMS is also hemocompatible and visibly clear, and therefore is a natural choice for blood flow behavior study.

## 3.1 Fabrication and Design

The fabrication methods focused on high aspect ratio channels in order to create a constriction in one channel dimension, but allow for sufficiently high flow rate without producing a shredding-effect due to high shear. (See Figure 4-2) Due to these design considerations, we had to be especially careful in our clean-room fabrication methods, in order to ensure proper negative photoresist attachment and development, described in more detail in Section A.1.1. Along with that, we had to optimize the channel spacing and observed that 20 μm spacing between 100 μm high channels was not sufficient, a separation of at least 100 μm between channels ensured proper fabrication and channel development – as further shown in Section 4.3.2.

Outside of optimizing the photolithography methods, our initial device featured a PDMS device bonded to a glass surface on the bottom. Over time, this difference in surfaces, especially in the corners, encouraged a large number of bubble deposition that were really hard to dislodge. In order to discourage corner-deposition, a spin-coated layer of PDMS was added on top of the glass slide before bonding to the PDMS device. By ensuring that the

entire channel consisted of one material, we were able to minimize yield variations (initially for water, and then for blood).


**Figure 3-1** A cross-sectional view of a PDMS-defined channel bonded to a microscope glass on the left. On the right, is the final approach used for this system, where a PDMS-layer is spin-coated onto the glass and then a PDMS piece defining the channel is bonded. This improvement minimized corner bubble entrapment.

## 3.2 Bubble deposition

It was very important to create a system that could provide reproducible, reliable separation results. Many initial designs provided occasionally great separation, but the lack of reproducibility and reliability of the device would hinder any further study and often created data that were too stochastic for behavior analysis.

Bubble deposition anywhere in the channel causes significant flow disturbance and hinders plasma separation, and therefore should be minimized. Beyond ensuring that the entire channel was made of PDMS, we evaluated other modification approaches. We attempted to modify the device surface by initially soaking the device in pluronic solutions. Pluronic or poloxamer is a triblock copolymer containing one central hydrophobic chain composed of poly(propylene oxide) (PPO) and two edge hydrophilic chains composed of poly(ethylene oxide) (PEO), or more briefly (PEO)m(PPO)n(PEO)m. This method helped device stability, but was hard to implement once the device connections and tubing were incorporated. Also, any dust collected on the outside of the device could then possibly enter inside of the device, and would increase the channel clogging rate significantly. We therefore pursued a more permanent solution by impregnating the PDMS device with the pluronic triblock copolymer. The water or blood in the channel would then draw out the hydrophilic arms of the pluronic polymer, and thus would discourage bubble accumulation.[115] The hydrophobic region of the pluronic triblock copolymer favors PDMS-copolymer interactions and discouraged pluronic loss into solution. This method helped eliminate some of the variables in the system, but was not necessary after other setup components were optimized.

We also washed out small bubbles that would collect at channel constrictions using a variety of buffers, such as pluronic, dextran, glycerol, and hydroxypropyl methylcellulose (HPMC) dissolved in water or PBS. We aimed for a fine balance of sufficient viscosity, so that the bubbles and impurities would dislodge, but not too viscous, so that the device wouldn't clog. Finally, a 1-10% glycerol solution in phosphate buffered saline (PBS), with the concentration matching the overall apparent viscosity of the (diluted) blood sample was implemented.

The biggest setback in the system was the initial loading bubble whenever a syringe was connected to the device tubing. No matter what setup was used, the initial bubble from the tubing-syringe connection would deposit at different points in the device and would throw off the separation values. Therefore, we implemented an inlet tubing Y-splitter, such that blood and the entrance bubble could be initially loaded into the device, then the blood flow would be shut off, and the buffer would enter the inlet and wash out all the bubbles deposited in the device. Then the buffer channel would be shut off and the blood flow would be re-initiated without any entrance bubbles. The overall setup is visually depicted in Figure 3-2. Going through this setup before every experiment dramatically improved consistency and separation in our system. The glycerol buffer would be approximately matched to the viscosity of the (diluted) blood and would also contain a dye so that the plasma and blood could be easily distinguished from the buffer.

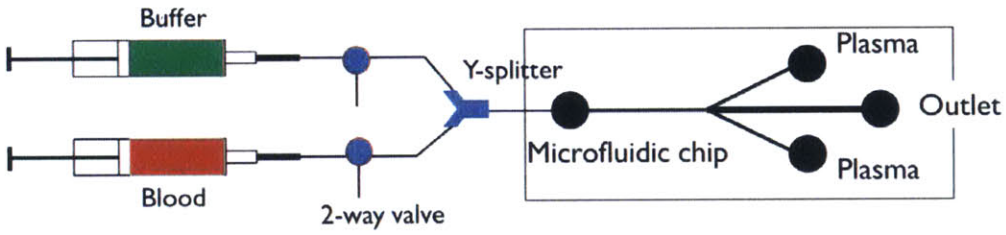


**Figure 3-2** Experimental setup for the plasma separation device, ensuring no bubbles are present in the device during the experiment. Initially, the syringe with blood is attached to the tubing and a small amount is loaded into the device (including the entrance bubble). Then the 2-way valve is closed, the buffer channel is opened, and the system is flushed with buffer, removing any residual bubbles. Then the buffer channel 2-way valve is shut off and the blood channel is reopened, now without any bubbles.

### 3.3 Interconnections and Outlet Setup

Initial device layout featured Gauge 23 stub adapter needle interconnections between the device and the tubing. Although this allowed for visual control for the depth of the insertion and for minimal leak issues due to the strength of the needle against the compression of the PDMS hole and tubing, this design limited long-term testing due to blood cell and clotting factor deposition on these metal components over time. Every material, corner, and high-shear area could eventually act as a clotting source, and therefore every non-essential component of the setup was eliminated, as can be seen in the photograph and schematic in Figure 3-3 and Figure 3-4, respectively.

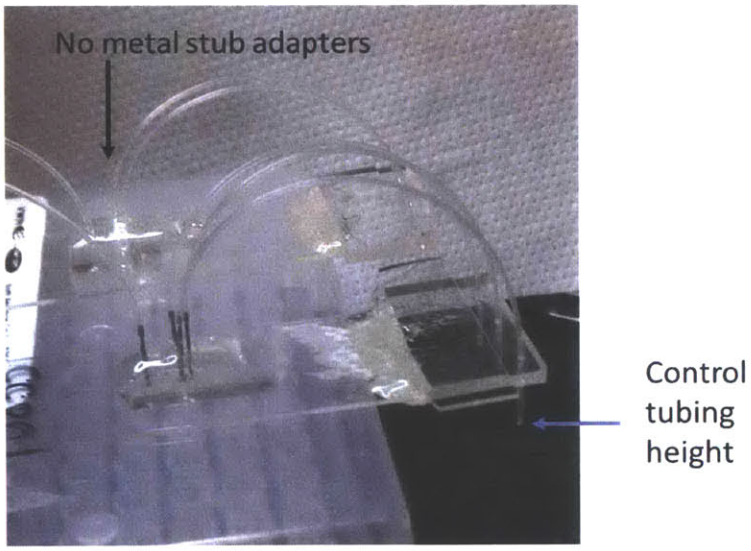


**Figure 3-3** A photograph of the older device design near the front, featuring metal stub adapters as the interconnection between the device and the tubing. In the background is the newer device with no metal components, the tubing is inserted directly into the device and (optional) epoxy is added to ensure no leaks. The outlet tubing height is controlled using a holder in order to further study pressure variation between plasma and outlet channels.

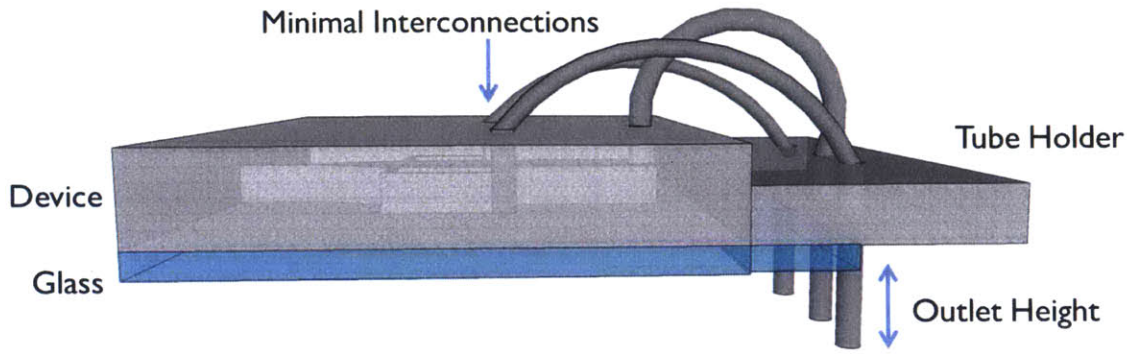


**Figure 3-4** A schematic of the simplified device design (the thin layer of spin coated PDMS on top of the glass is not depicted). A tube holder allows for better control of tubing height when collecting plasma fractions.

# CHAPTER 4. PLASMA SKIMMING – T CHANNEL DESIGN

Early plasma-skimming *in vitro* designs were inspired by an *in vivo* study first conducted in 1933.[54] In this work, blood viscosity in the large artery, small artery, and capillary was compared in a hind limb of a dog. The group observed that in these small arteries and capillaries, the apparent viscosity was smaller than predicted, and then correlated this effect to the lower number of cells (lower hematocrit) present in these small canine blood "channels". This work has inspired a detailed study of blood viscosity and its dependence on flow rate, vein or channel dimensions, cell percent volume, etc. A large number of the analyses and the effects, described below, stem from this initial *in vivo* study.

## 4.1 Zweifach–Fung Effect and Plasma Skimming

The Zweifach-Fung effect is a bifurcation law that was developed based on *in vivo* experiments which showed that, given a channel split with a daughter channel presenting significantly lower flow rate, majority of the blood cells would not go into this daughter channel.[56-58, 62] This effect was contributed to the asymmetric distribution of the pressure and shear forces on the cells reaching this bifurcation point, although the exact physics are still being debated. Based on the literature using this effect, for channels defined by the dimensions similar to the red blood cells (around 5-10 μm), a flow rate ratio of 2.5:1 for outlet to plasma is required for a low number of cells in the plasma skimming channel, even if the outlet and plasma channel diameters are about the same. Other experimental designs, with slightly larger channel dimensions, although still on the order of 10-20 μm, showed better separation values for 0.1 blood volume when the ratio was around 8-10:1 for outlet to plasma flow rates.[57]

There is a parallel set of work focusing on the apparent blood viscosity and the overall shear-thinning behavior of blood for certain shear rates and channel dimensions.[116] This behavior has been contributed to a lower channel hematocrit, or % cells by volume, and has been defined as the Fåhraeus effect, or the Fåhraeus-Lindqvist effect.[117] During the later decades, Pries et al. built upon this effect, and compiled as well as contributed to the study of hematocrit, and therefore viscosity, based on the tube or channel diameter.[118, 119] This

effect was especially prominent for tubing with diameters smaller than 300 μm, down to around 5-10 μm at which point the cell size and aggregation begin to dominate the flow behavior. At low shear rates, the effect was attributed to the formation of aggregates or rouleaux (linear, stack-of-coins- like aggregates) near the center of the tube, due to the strong cell-to-cell interactions and the protein concentration in solution. This led to a larger fraction of cells in the higher flow region near the center, thus effectively spending less time in the channel and creating an apparent lower hematocrit in the channel.[117] Overall viscosity relationship was not as clear, since the stack-like aggregates do provide lower hematocrit, but these now effectively larger particles could cause disturbances in the channel flow much more so than single cells. Therefore the apparent viscosity is affected not only by the hematocrit, aggregation, and shear rates, but by channel geometry, and other less dominant factors.[119] For very slow flow rates, such as capillary flow, the effect of gravity or sedimentation would also play a role in apparent viscosity.[118] Also, RBC re-suspended in buffer without proteins showed a significantly different viscosity vs. shear rate behavior.[119]

At higher flow rates, aggregation is no longer the dominant effect and is only present in local areas of low shear rate. Once inertial effects begin to dominate over the viscous behavior, the red blood cell movement towards the center (thus creating a local lower hematocrit, once again) is attributed to a balance of shear and wall lift.[6, 51-53, 120] This effect was further understood in inertial microfluidics where the cells move towards an equilibrium position in the channel once the forces are balanced. This effect is defined by flow disturbance due to the particle presence, as well as particle lagging the flow in the channel, which leads to addition center-directed particle movement (this effect plays a role especially when the particle diameter is comparable to at least one of the channel dimensions).[53] Of note, however, is the fact that inertial microfluidics focuses on very dilute suspensions such that there no cell-cell interactions, and the channel size tends to be much larger than the cell diameters in order to be able to split different cell types into separate streams.

In the blood separation literature, the channel dimensions that are closer in value to the diameter of the cells experimentally present a larger cell free layer. This has been in part attributed to the cell lag behind the fluid in laminar microfluidic flow.[53] In the case of human blood, the red blood cells are also highly deformable and discoid, and therefore

exhibit an even greater shift towards the center of the channel. The deformability of the cell allows for the particle to more easily match the shear rates across the cell membrane and therefore get pulled up towards the faster flow streams, while keeping the same shape as the cell tank treads; this force is defined as a viscoelastic force.[53, 55] There seems to be a general increase in cell movement towards the center with the increase of cell deformability. The discoid shape also helps the cell match these rates and adapt to the shear stresses present in the channel. These important physical differences in red blood cells and their behavior are a large component of why this type of separation is possible despite the high density of cells in solution and apparent complex behavior of blood.

In fact, the bifurcation law is often argued in the context of this cell distribution inside the channel. Beyond the cells favoring the middle, there is always a thin cell free layer near the wall due to the shape of the cell and the fact that the center of mass of the cell cannot get closer to the wall than one radius away. Therefore this overall distribution leads to enhancement of the cells present in the high flow rate channel.[55]

## 4.2 PEEK Tubing Plasma Skimming T-Design

### 4.2.1 T-Design Tubing Setup

The majority of the blood separation work in plasma skimming focus on the Zweifach—Fung effect and on the pressure drop ratios of channels, implying that as long as the resistance in the plasma channel was large enough, pure plasma could be skimmed off the side, no matter what the exact angle or design of the Y-bifurcation (for channel dimensions below 300 μm).[57] Therefore our initial design focused on the possible elimination of the microfluidic device in order to a lower cost and an easy to build design. We chose to use hard polyetheretherketone (PEEK) tubing and a plastic channel splitter in order to take advantage of a large number of inner diameters (ID) available and to minimize any contact with materials that might encourage blood clotting. The smallest UpChurch Microtee splitter available had an inner volume of 58 nL and 152 μm diameter channels. (Figure 4-1) The diameter and length of each of the tubes (especially the relative plasma and outlet tubing) was calculated such that the resistance ratio was around 9 to 1 for plasma to outlet, respectively, using the typical pressure drop equation for a pipe[49]:

$$\Delta P = R_H Q = \frac{8\mu L}{\pi R^4} Q$$

**Equation 4-1**

where $R_H$ is the hydrodynamic resistance, Q is the volumetric flow rate, μ is the dynamic viscosity, L is the length of the tube, and R is the inner radius. The inlet tubing ID was chosen to be as small as possible in order to recreate the constriction of the blood and thus enhance the cell free layer near the tubing surfaces. The length of the inlet tubing was also minimized in order to have a smaller pressure drop across the device.

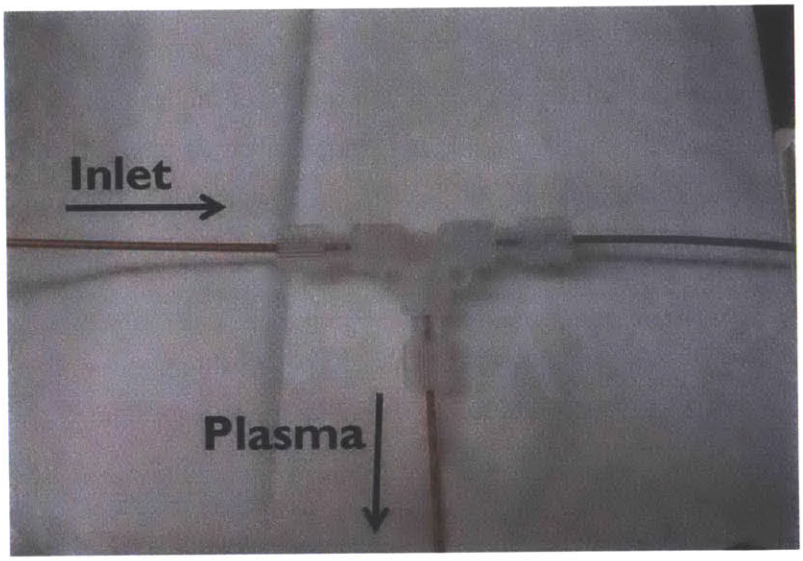


**Figure 4-1** A photograph of a typical T-split using PEEK tubing. The inlet tubing length required was defined by the syringe-fitting as well as the microtee fittings. The outlet and plasma tubing lengths and ID were defined by the resistance calculations.

### 4.2.2 PEEK Tubing Separation Results and Conclusions

The two inlet tubing sizes tested had 25 and 62 μm inner diameters. Due to the microtee and tubing-syringe fitting requirements, the minimum length of the inlet tubing was found to be 1.25 inches. Unfortunately, for the 25 μm inner diameter tubing, a syringe pump could not handle such a high pressure drop in the system and would consistently stall without showing proper separation. Due to the low separation results, a high-pressure system was not studied. The 62 μm inner diameter inlet tubing features around a 40 times decrease in the pressure drop (the pressure drop varies inversely with the radius to the fourth power, as seen above), and was easily run by hand or by a syringe pump. Unfortunately, despite the correct and

consistent mass fraction of around 0.11 collected from the plasma channel across various flow rates (10-200 μL/min), the separation results showed no significant decrease in the cell number for the plasma channel for 0.1x blood volume (10 times diluted blood). This could be due to the limited constriction using a 62 μm inner diameter tubing, possible vortices or instabilities inside the microtee expansion, or other variables that are not be clearly defined in the literature and for the current level of understanding of blood behavior. This initial test proved the advantage of using microfluidic systems in order to create smaller diameter channels, and have more precise control of the flow and separation, without being limited by a very high pressure drop.

## 4.3 High Throughput Microfluidics T-channel Design

### 4.3.1 Plasma Skimming Literature Designs

After confirming the importance of a small-volume microfluidic design in order to create a low power, low pressure drop, and possibly portable design, the literature T-channel plasma skimming designs were used as guidance. The layout featured a small constriction channel, followed by small plasma skimming channels that are perpendicular to the main channel flow. (See Figure 4-2)

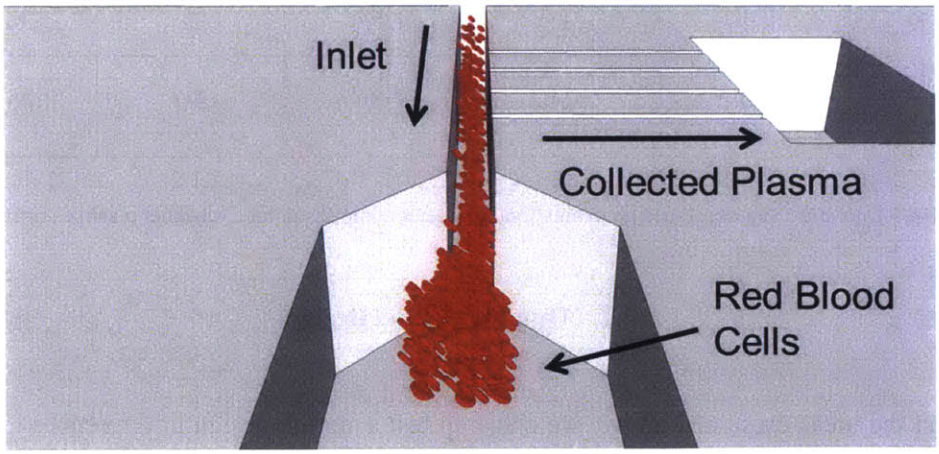


**Figure 4-2** A depiction of a typical T-channel plasma skimming design where small perpendicular plasma channels skim off the cell free layer created by an inlet constriction channel. The device design features a thin but tall inlet channel (high aspect ratio) in order to replicate the constriction behavior while allowing for a higher throughput.

Early *in vitro* plasma skimming work, published in 2006 - 2009, focused on very small channels with dimensions around 10-15 μm for each dimension and at most 0.1x blood volume (10 times diluted blood).[56-59] The flow rates were in the range of 0.5-10 μL/hour and the purity of the plasma was evaluated qualitatively by visual methods. (See Table 4-1) The same T-channel plasma skimming was also expanded to a much faster throughput (2-5 mL/min) using a very high aspect ratio (280-700, with a 14 mm width as the largest dimension), and a quantitative calculation of plasma purity, but unfortunately the separation values were not very high.[60] And much more recently, in 2013, a controlled study of the flow rate ratio of the outlet and plasma in a T-channel plasma skimming device was studied.[61] The best data points from the pertinent literature are summarized in Table 4-1.

| First Author (Year) | Flow Rate (μL/min) | Blood Volume Fraction | Plasma Purity | Isolate Cell Ratio | Plasma Yield |
|---|---|---|---|---|---|
| Yang[56, 57] (2006) | 0.17 | 0.1 | Visual Evaluation | N/A | 0.07 |
| Jaggi[60] (2007) | 2,000-5,000 | 0.1 | 92% | 12.5 | 0.025 |
| | | 1 | 31% | 1.4 | 0.04 |
| Qin[59] (2009) | 0.0096 | 0.1 | Visual Evaluation | N/A | 0.15 |
| Tripathi[61] (2013) | 150 | 0.1 | 97% | 33 | 0.018 |
| | | 1 | 67% | 3 | N/A |
| Our T-Design | 20 | 0.1 | 67-86% | 3-7 | 0.05-0.07 |

**Table 4-1** Literature and our T-design evaluation parameter comparison for T-channel plasma skimming.

### 4.3.2 Our T-Channel Design

Based on the ideas presented above, we chose to test a similar design to references [57, 59], but with high aspect ratio channels in order to increase the flow throughput in our device while still providing a constriction channel for increase in cell free layer. The inlet constriction featured either 15 or 30 μm wide channels, with 100 μm height dimension. There

were 5 plasma skimming channels on the side, each 10 or 20 μm wide, which collected to a single outlet exit. Due to the high aspect ratio fabrication, it was essential to space out the plasma channels sufficiently or else the SU-8 negative photoresist would not properly cross link and the plasma channels would not be properly separated or would vary in height in that region. Experimentally, it was found that the 20 μm space between the channels was not sufficient, while 100 μm spacing created clear, fully developed channels. (Figure 4-3) The resistance difference between the outlet and the plasma was varied with channel lengths defined on the photoresist mask, as well as with outlet and plasma tubing used for sample collection outside of the device.

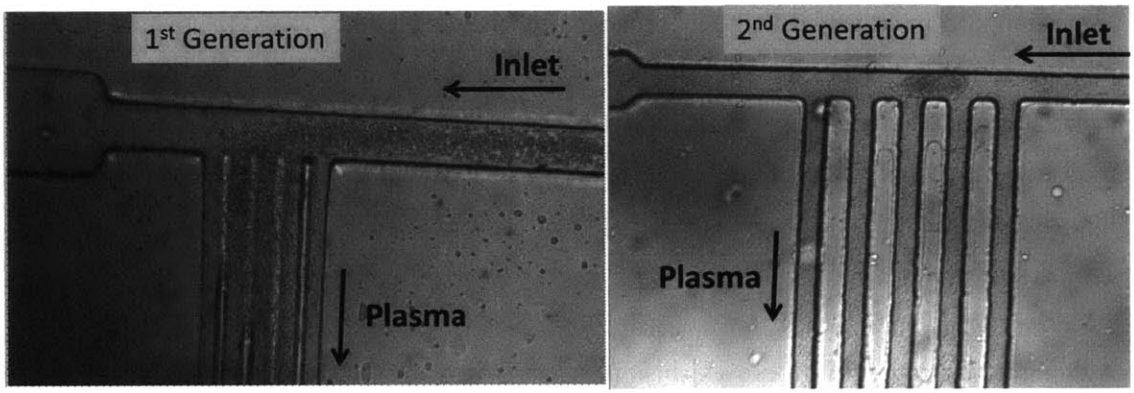


**Figure 4-3** A microscope image of a first generation T-channel skimming design without proper channel definition, on left. Later generation designs ensured channel spacing to be sufficiently large so that every feature was fully defined, on right.

After the introduction of pluronics-doped PDMS as described in CHAPTER 3, as well as removing any metal connections, the device showed good stability and reproducibility of mass fraction and separation. However, the best separation was around 3-7 isolate cell ratio, with plasma yield around 0.05-0.07 for flow rates around 20 μL/min for 0.1x blood volume (10 times diluted blood). Although this was comparable to some of the literature values, it was not a sufficient improvement and did not expand our understanding of blood behavior in these microfluidic devices. The channel dimensions of 15 μm for the inlet channel and 10 μm for the plasma channels caused some increase in device clogging, and thus only 1-3 experiments could be run before clogging or aggregate deposition altered the device behavior.

# CHAPTER 5. PLASMA SKIMMING – EXPANSION DESIGN

## 5.1 Background Literature

Along with T-channel plasma skimming, there is a parallel field of microfluidics focusing on rare cell isolation in blood. One of the approaches to rare cell isolation is through the use of channel expansion traps, which takes advantage of continuous inertial focusing of particles prior to the expansion, and then flow vorticity-fueled traps for rare cells, which are physically distinct from the bulk population of cells.[51, 120] In these expansion traps, one can experimentally visualize the temporary enhancement of the cell free layer right after the expansion, due in large part to the deformability of the red blood cells and the overall balance of shear gradient lift and the wall lift due to the asymmetry of the fluid profile around the cell, as discussed above. This temporary increase in the cell-free layer is the same approach used in the Kersaudy-Kerhoas, M. et al. work [62, 63], which showed significant increase in the purity of the plasma isolate over the literature results for T-channel plasma skimming. (See Table 5-1)

Although the vorticity in these expansions seems to enhance cell entrapment, this type of behavior could also be hard to control and could lead to irreproducibility or instability in the system if the number of cells in solution increases to the point of cell-cell interaction. These vortices are occasionally mentioned in blood skimming literature, but there hasn't been any in-depth study of these behaviors effects on the blood separation and reproducibility. These vortices could in fact have been limiting the flow rates the microfluidic system could sustain while producing meaningful results, as can be extrapolated from some of the discussion in Kersaudy-Kerhoas, M. et al.[63]

| First Author (Year) | Flow Rate (μL/min) | Blood Volume Fraction | Plasma Purity | Isolate Cell Ratio | Plasma Yield |
|---|---|---|---|---|---|
| Yang[56, 57] (2006) | 0.17 | 0.1 | Visual Evaluation | N/A | 0.07 |
| Jaggi[60] (2007) | 2,000-5,000 | 0.1 | 92% | 12.5 | 0.025 |
| | | 1 | 31% | 1.4 | 0.04 |
| Qin[59] (2009) | 0.0096 | 0.1 | Visual Evaluation | N/A | 0.15 |
| Tripathi[61] (2013) | 150 | 0.1 | 97% | 33 | 0.018 |
| | | 1 | 67% | 3 | N/A |
| Kersaudy-Kerhoas [63] (2010) | 33 | 0.1 | 95-100%* | 20-N/A | 0.05-0.3 |
| | | 1 | 99%* | 100 | 0.05 |
| Our Expansion Design | 50-200 | 0.1 | 100% | 1,000-10,000 | 0.05-0.15 |
| | | 1 | 100% | 500-10,000 | 0.05-0.12 |

**Table 5-1** Results comparison of evaluation parameters for the literature and our expansion plasma skimming. * indicates addition of oxalate in an undetermined amount, which could possibly alter physical parameters of the cell as well as cell-cell interaction.[121]

## 5.2 Expansion Design

Ideally this flow behavior could be understood and predicted using numerical methods. Unfortunately, blood is a very dense suspension, featuring on the order of $10^9$ cells/mL, is a shear thinning fluid, the apparent blood viscosity decreases with increasing shear rate, contains mostly red blood cells, which are discoid in shape and are highly deformable, and features cell-cell, cell-protein, and cell-wall interactions and steric effects. Therefore, a lot of model parameters are very sensitive to the system geometry, and would require the simultaneous solution of deformation, flow, and interaction effects. Although studies are ongoing in improving the simulation and understanding of red blood cell interactions to approximate and visualize the cell free layer and stability of flow, the experimental

applicability is still very limited to very specific geometries, and features significant assumptions, as further discussed in CHAPTER 6.[53, 120] There are some large-scale blood behavior models that approximate blood stability without including cells, such as the power-law or Carreau models, but they are more of a qualitative guide,[122] as can be visualized for our system in Figure 5-1. This model was applied to a number of geometries with a range of plasma fractions, but overall the results proved to be more of a qualitative guide in helping us define the angle range as well as the approximate flow rate range to test experimentally.

We chose to replicate these designs using polydimethylsiloxane (PDMS) and soft lithography, in order to experimentally study a range of designs, blood flow stability, and separation ability and reproducibility. Therefore, building from the two design limits, shown in Figure 5-1, we studied a range of angles, the extreme 90° expansion that's often used in the literature, as well as a range of angles from 5-30°, in increments of 5°. (Figure 5-3)

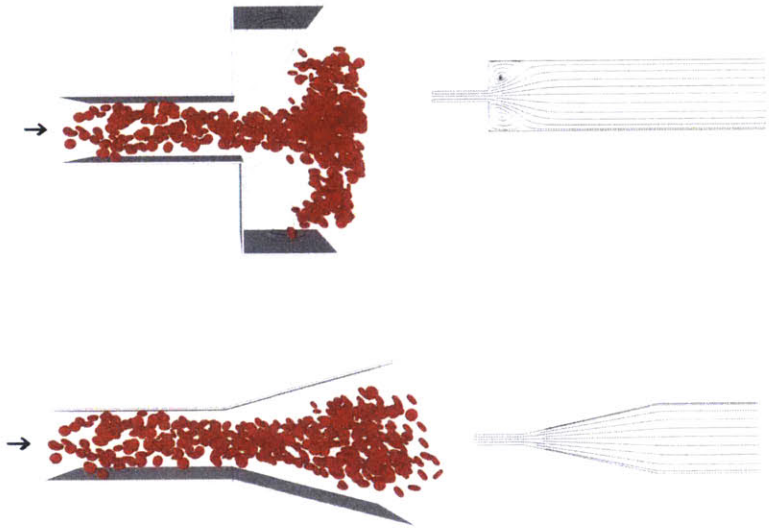

**Figure 5-1** Representation of hypothesized blood behavior in representative channel expansion designs.

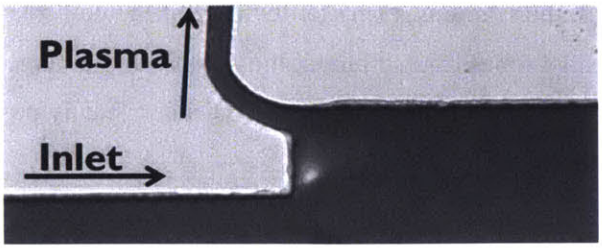


**Figure 5-2** Microscope image of an abrupt constriction-expansion design (90° expansion) showing flow vorticity and obvious high cell number in the plasma channel. The dark components are the red blood cells which help visualize the flow field. The small clear-region after the expansion is the center of a vorticy.

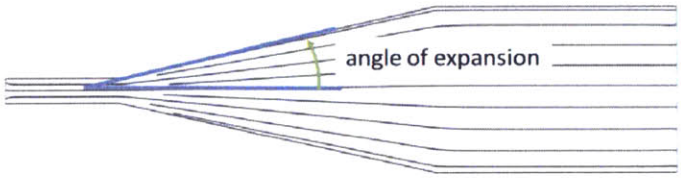


**Figure 5-3** The definition of the angle of expansion in our channel. Plasma was skimmed off using side-channels as soon as the channel width reached the specific outlet width.

## 5.3 Results and Discussion

Once the bubble instabilities were eliminated, it became clear which angles provided stable separation results. By studying a range of resistances and flow rates, we were able to establish a comparison of separation for multiple blood dilutions. Initial work focused on 10 times diluted blood (0.1x blood volume fraction), since 10-20 times diluted blood is the most common comparison point for separation devices in literature. Pretty quickly it became clear that any expansion angle larger than 20° produced very unstable, and generally low separation values on the order of ~10 for isolate/plasma cell ratio. This instability is most likely due to the vorticity in the expansion region. As presented in Figure 5-4, we observed that the 20° expansion gives good separation values for 0.1 blood volume, although it is hard to predict what mass fraction will be collected even for the same outlet vs. plasma resistance ratio. 15° and 10° expansions led to the most reproducible results, with little sensitivity to flow rates in the range of 75-200 μL/min, but produced a decrease in mass fraction with a larger resistance in the plasma channel, hence presenting a range of yields. 5° expansion gave strong results but was overall slightly less effective at separation. This might be because the

expansion is so gradual, thus there is a smaller increase of the cell free layer for this diluted blood sample. Thus for 10 times diluted blood, the optimal angle range was found to be 10-15° expansion, with 5° expansion being a close contender, but is possibly limited due to smaller cell free layer increase.

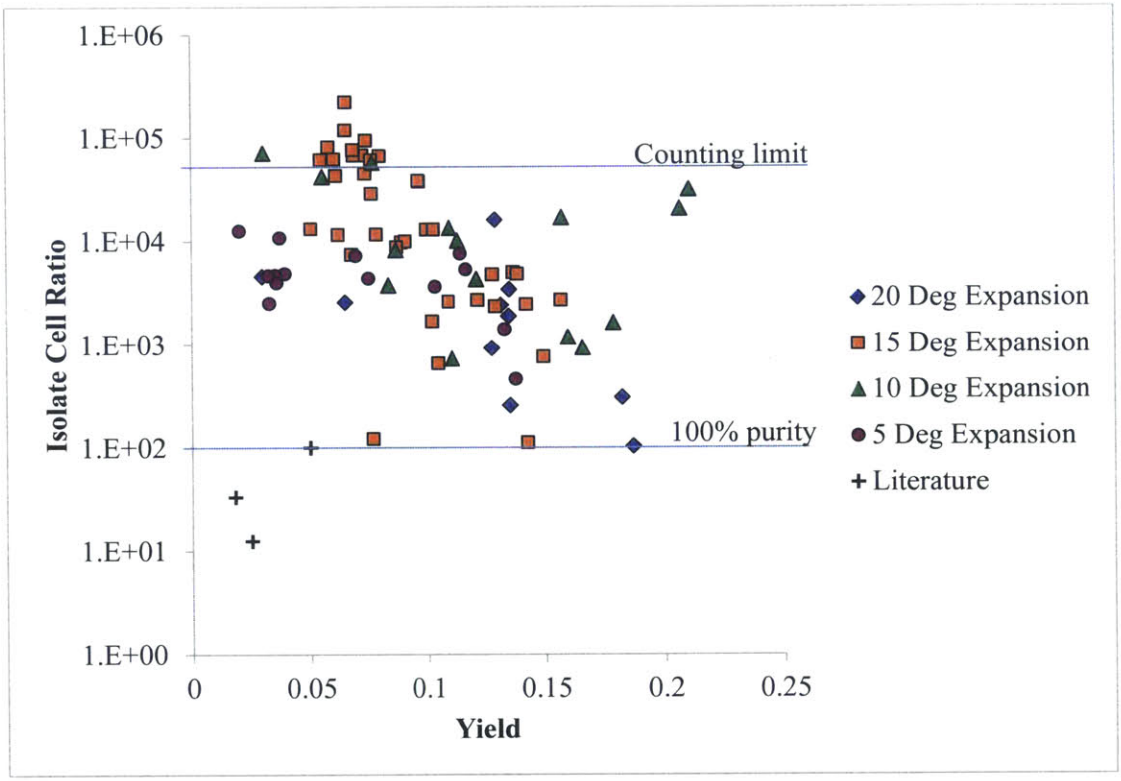


**Figure 5-4** Blood separation for 0.1 blood volume (10 times diluted blood) using different expansion angle designs. Literature value comparison is included. Ideally, the yield and isolate cell ratio should be as high as possible, meaning that a lot of plasma is collected with a low cell count present in the plasma.

Overall, the data show a significant improvement over the literature's best values for these types of systems. Kersaudy-Kerhoas, M. et al.[63] mentioned a possible 250x isolate separation value, without specifying a mass fraction value, for 10 times diluted blood (0.1x blood volume fraction), which is still significantly lower than the separation values we were able to show with these range of angles. The Kersaudy-Kerhoas, M. et al. work, however, used oxalate to improve blood stability and allow for the use of blood for an entire month without reported aging effects. Unfortunately blood cell deformability, hematocrit, viscosity and therefore behavior can significantly change depending on the amount of oxalate added.[121] It is unclear how much of an effect this had on their system. We used blood

without any anticoagulant except for the EDTA-coated vials for collection and storage. EDTA has not shown to have the same altering effect on blood cells and flow behavior. In the past, we have added acid-citrate-dextrose to test stability improvements, but we did not see any significant improvement for separation or storage. Most of the blood experiments were conducted within the first 10 days.

Similarly, for 0.333x blood volume fraction (3 times diluted blood), we observed that the 20° expansion angle provided some good results, but was not as reliable and was more sensitive to flow rate when compared to the 15° expansion, which provided good separation for flow rates 100-250 μL/min. Both 5° and 10° expansions showed comparable, but slightly lower separation values, relative to the 15° expansion. Although the literature only has one specific case for 3 times diluted blood, our results are once again significantly higher than the literature for either 3x or 10x diluted blood, and showed significant improvement above the 100% purity literature reports. The data are presented in Figure 5-5.

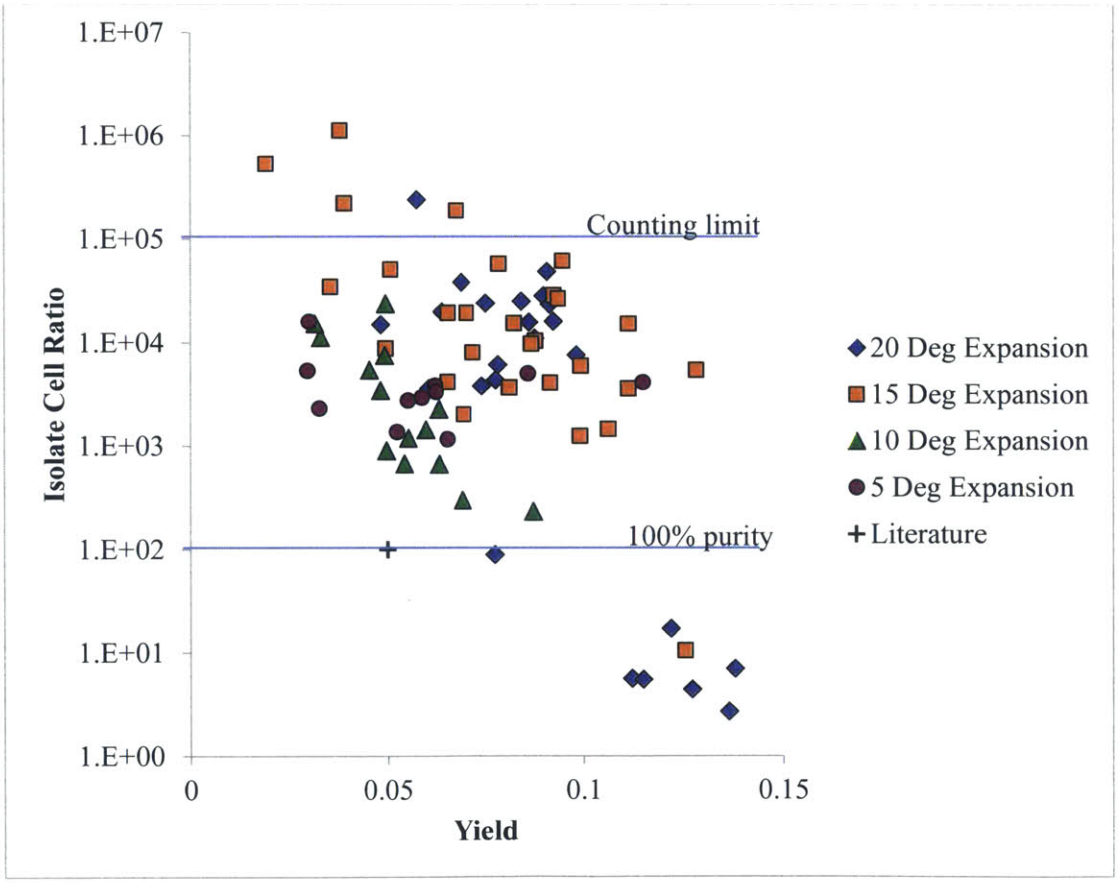


**Figure 5-5** Blood separation for 0.333x blood volume (3 times diluted blood) using different expansion angles in the system. Literature value comparison is included.

Undiluted blood presents a challenge far beyond 3-10 times diluted blood, due to the larger variation in viscosity of the solution depending on shear rates, and higher chance of clogging and clotting due to such a large number of cells and proteins present in solution. For undiluted blood, we observed that the system is much more sensitive to solution handling and to the flow rates used. Overall, both 10° and 15° showed very limited separation for the majority of the resistance ratios. Although the separation values are comparable in separation to some of the literature, but with a much higher yield, they still contain a large number of cells and would require a second separation step before any sensing component could be added. There were occasionally large isolate cell ratio values, but these values were hard to reproduce. We did find that the 5° expansion gave us the most reliable results, when the flow rate was around 25-75 μL/min for one specific resistance ratio between plasma and outlet. This flow rate is lower than for diluted blood (100-200 μL/min), but very comparable to the literature values. The best separation in the literature was done at 33 μL/min, showing around 100 isolate cell ratio, but again using oxalate. Overall, undiluted blood separation was improved 10-1000 times over the literature values, with larger yield results. Summary of 0.1x and 1x blood volume results are compared to literature in Table 5-1.

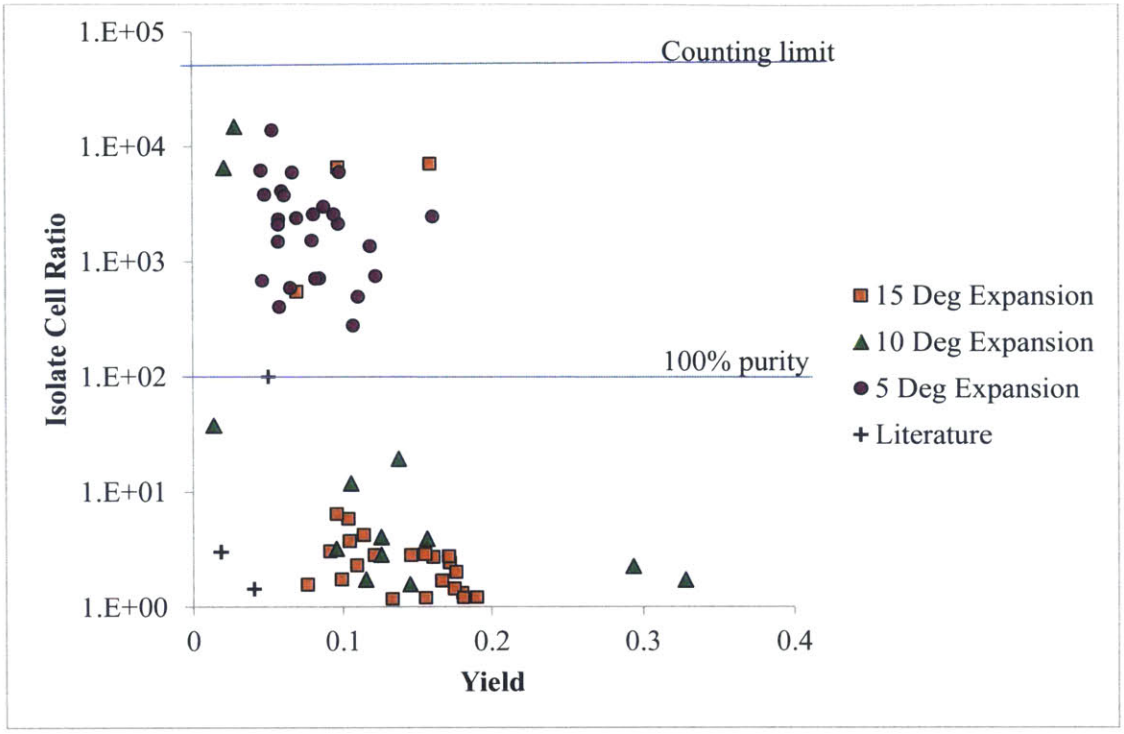


**Figure 5-6** Blood separation for undiluted blood using different expansion angles in the system. Literature value comparison is included.

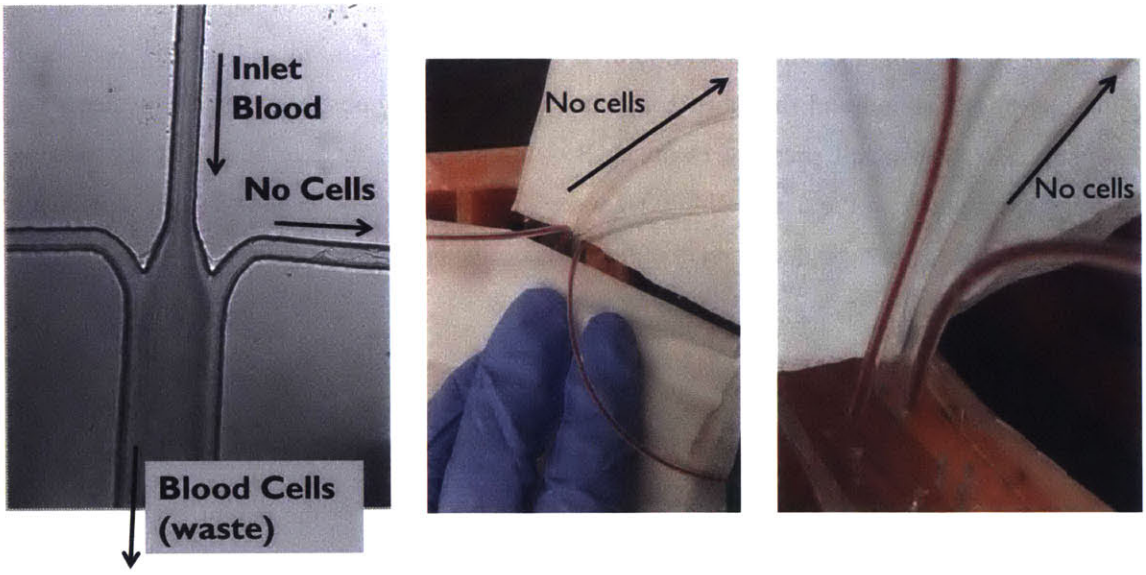


**Figure 5-7** On the left is a microscope image of blood flowing through the microfluidic channel, with clear cell plasma collected off of the sides. This is in sharp contrast to the 90° expansion image showing a large number of cells in the plasma channel. In the middle and most right is a photograph of the device (1 cm in length) with clear plasma collection off of the plasma channels.

## 5.4 Setup and Design Details

Our plasma yield is defined by the pressure drop ratios of the outlet/waste channel vs. the side plasma channels. The pressure drop can be calculated using the channel flow rate and fluidic resistance in a channel:

$$\Delta P = R \cdot Q$$

**Equation 5-1**

where $\Delta P$ is the pressure drop across a channel, R is the channel resistance, and Q is the volumetric flow rate. When we add external tubing to collect the plasma fractions, we essentially create resistances in series:

$$\Delta P_{total} = R_{total} Q_{channel} = (R_{channel} + R_{tubing} + R_{external}) Q_{channel}$$

**Equation 5-2**

where by manipulating the resistance defined by tubing or other external factors (such as a height different between the exit points of outlet and plasma tubing), we can expand the design study beyond what we define on the microfluidic mask. For example, certain tubing with very small inner diameters can dominate the overall resistance and lead to very high plasma mass fraction and therefore poor separation. We also observed that the system was sensitive to even small pressure changes. By increasing the relative height of the plasma tubing exit relative to the outlet tubing, we were able to see a significant change in the plasma yields. The pressure drop due to relative height is defined using the equation:

$$\Delta P = \rho g h$$

**Equation 5-3**

where $\rho$ is the fluid density, g is the gravity constant, and h is the height difference. An example of this pressure effect is plotted for a specific 15° expansion design and specific tubing, for 0.1x blood volume, with added pressure resistance to the plasma tubing measured in Pascals:

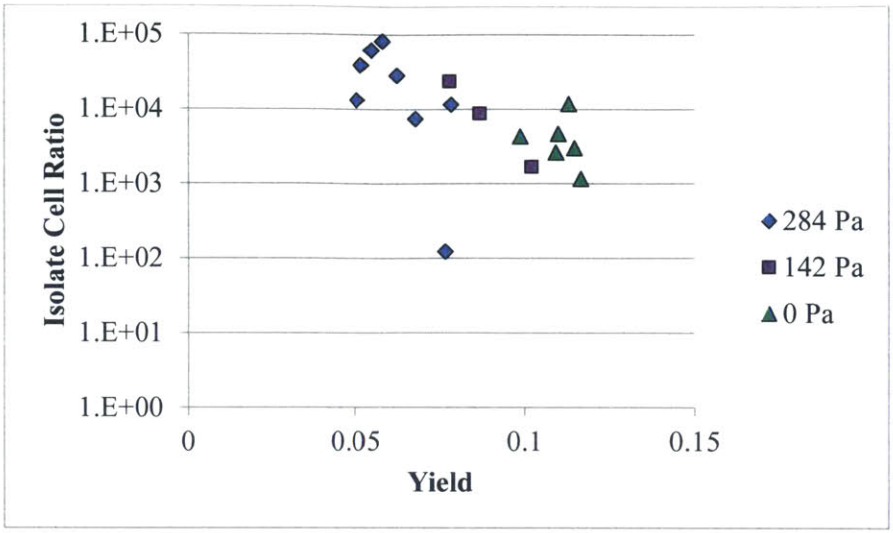


**Figure 5-8** Isolate cell ratio vs. yield for a range of plasma vs. outlet tubing pressures shows the system is sensitive to pressure for this case.

By using this type of data for each design, we are able to evolve each generation of devices to produce the range of yields that we are interested in. We evolve the design by using the following resistance equations:

$$R_{tubing} = \frac{8\mu L}{\pi R^4}$$

$$R_{squarechannel} = \frac{K\mu L}{wh^3}$$

**Equation 5-4**

where $\mu$ is the viscosity of the fluid, L is the channel or tubing length, R is the tubing inner radius, w is the channel width, h is the channel height, and K is a constant that depends on the ratio of w/h (and is equal to 12 for high aspect ratio channels, w<<h or w>>h).[49, 123, 124] K is an approximation that can be looked up in an engineering handbook or if a more exact value is needed, the full square channel resistance equation can be used:

$$R_{squarechannel} = \frac{12\mu L}{wh^3}\left(1 - \frac{h}{w}\cdot\left(\frac{192}{\pi^5}\sum_{n=1,3,5}^{\infty}\frac{1}{n^5}\tanh\left(\frac{n\pi w}{2h}\right)\right)\right)^{-1}$$

**Equation 5-5**

From these equations, we can calculate the needed resistance that we should incorporate into the channel so that it is equivalent to the added resistance due to height or due to tubing variation. The apparent blood viscosity changes significantly with different levels of dilutions and based on local shear rates, therefore experimental values for the volumetric flow rates and yields were also very helpful in designing the new microfluidic designs to produce the optimal yields.

## 5.5 Device Lifetime and Stability

The best separation reported in literature features channels with 10-20 μm width and height, with reported clogging after 2-3 experiments. For our larger channel dimensions, after proper optimization and buffer washes, we were able to reuse devices for weeks, yielding an opportunity to study a wide range of settings without clogging for diluted blood. Undiluted blood presented much more of a challenge and would occasionally lead to short device lifetime especially for harsher angles, and under certain lamps due to slight sample heating. The majority of device loss occurred early in the experiment, and was due to leftover photoresist pieces or due to small particles which were present from fabrication and inlet/outlet punching.

The main reproducibility issue is for undiluted blood, mostly due to the difficulty of removing all of the small bubbles in the solution. This would occasionally lead to flow instability and a loss of purity after around 30-50 μL of plasma is collected. This instability can be minimized with extra care when mixing and loading the syringe, but has to be optimized against the need to properly mix the suspension of cells for device loading. The other issue is the occasionally large number of platelets in the collected plasma fraction, especially for undiluted blood. The platelets are much smaller than and not as deformable as red blood cells and therefore can be found near the channel walls. Their small size and still low concentration does not seem to present an issue for optical sensing, but could possibly lead to some electrical sensor fouling.

## 5.6 Expansion Contraction Expansion Design

We hypothesized that skimming one plasma channel at a time could possibly improve our separation values and device stability, and therefore designed a "constriction-expansion-constriction-expansion" device with only one plasma skimming channel at each expansion. We did not see any significant improvement in separation compared to the initial "constriction-expansion" design described above. In fact, the device lifetime was often shorter mostly due to the second constriction which was much more prone to clogging with cell-aggregates, PDMS pieces from inlet/outlet punching, or possible leftover photoresist pieces embedded in the channel after PDMS device peeling. Therefore this design was not pursued further.

## 5.7 Cascade Design

A cascade, or a multistage design where separation steps are strung in series is an approach that has been applied to multiple other separation methods, such as deterministic lateral displacement.[48] We briefly tested this setup by connecting a second stage separation device to each plasma channel and by trying to balance that out with higher resistance at the outlet. The cascade design for this expansion-based separation is limited by the final yield. Blood plasma is 40-60% of blood volume. The entire plasma fraction is hard to collect even with a laboratory centrifuge due to solution trapping between cells. For our expansion approach, we are taking advantage of the cell and flow dynamics to temporarily increase the cell free layer at the expansion. This system would inevitably require a significant fraction of plasma to surround these red blood cells in flow. Therefore, we found it hard to push the yield fractions beyond the 10-20% of plasma (relative to total blood volume). Beyond a certain cell free region, we encounter red blood cells that are present at a higher concentration than the concentration average inside a blood collection tube. Therefore it is hard to replicate or exceed the separation values we present for undiluted blood in Figure 5-6, without also encountering the issue of very low plasma yield.

## 5.8 Cell Health

It is important to ensure that the cells are not getting ripped by the shear rates in the device or other setup connections. If cells are lysed in the process, they would release a large amount of salts and proteins, which would limit the applicability of this separation system for protein or other biological sensing, and would throw off our purity calculations.

Due to the red color of hemoglobin, which is present mostly in red blood cells and in limited amounts in the plasma, hemolysis can be detected by eye for any levels above 0.09%.[125] Approximating the color by eye is also commonly used in hospitals to assess the health of the blood for transfusions. In order to ensure that lysing was not the reason for good separation values, the plasma fraction and waste blood collected from the outlet were spun down in the centrifuge and checked against a white background for color. (Figure 5-9) The buffer wash step was found to be important in ensuring that the channels are clear of any debris between each experiment. Also, other factors such as certain natural-light lamps, which would lead to slight device heating, would cause undiluted blood clotting and occasionally significant lysing. Once the buffer wash steps were added, the blood cell count was consistent throughout the experiment and the plasma components stayed a healthy yellow.

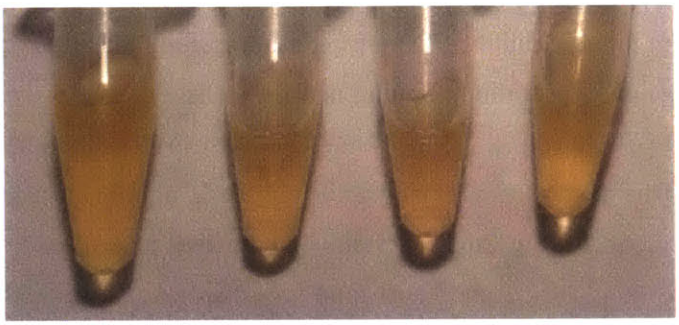

**Figure 5-9** An example photo of undiluted blood plasma for color comparison. From left to right - decanted plasma that experienced minimal user handling, plasma after flow through device at 50 μL/min, then 100 μL/min, and on the most right 300 μL/min.

In order to quantify blood lysing beyond the visual control, hemoglobin was measured by absorbance using the Cripps et al. method.[126] This method was found to be the most reliable for hemoglobin quantification and allows for subtraction of other proteins that could be interfering with the absorbance.[127, 128] The plasma collected from microfluidic devices

was compared with centrifuge separation and with decanting (where blood was allowed to settle overnight in the refrigerator). Centrifuging was very gentle, at 1,000 g for 10 minutes, twice, decanting plasma each time. The microfluidic plasma was tested for 10-300 μL/min flow rates, at the full range of dilutions. The absorbance measurements confirmed what was tracked by eye. Lysing was found minimal and exactly the same for microfluidic device and the centrifuge spin down method. The decanting method was slightly less disruptive to the cells, but all of the absorbance values were close to the background values and were at the lowest end of the absorbance range studied for hemolysis. Therefore the shear rates, balanced by the short residence time inside the device, do not seem to have a significant effect on blood lysis.

# CHAPTER 6. FINITE ELEMENT STUDY OF EXPANSION DESIGNS

Modeling blood flow in a channel presents an interesting challenge. Each milliliter of blood contains about $10^9$ cells, which interact with the walls, other cells, proteins, adapt to the shear profile of the flow solution, disturb flow profiles, and can dominate the overall viscosity of the solution.[51-53, 120, 129, 130] These interactions are complicated by the discoid red blood cell shape, as well as the significant deformability of the cell, and create a complex problem spanning multiple length scales. Even plasma itself was recently found to have a slight shear thinning, non-Newtonian behavioral profile.[131] The overall "apparent viscosity" aggregates all of these events into one measurement and thus is also hard to predict exactly without experimental methods. Both high detail and low detail modeling approaches are discussed below. Our focus is on inertia-dominant systems due our system featuring Reynolds numbers significantly larger than 1.

## 6.1 High Detail Numerical Analysis – Success and Limitations

The red blood cell is hard to model – it is discoid, with a diameter of around 6-8 μm and a thickness that varies from 2 μm at the edge, to 1 μm in the center. (Figure 6-1) Because of this high curvature, modeling the shape, especially when it is deformed due to shear rates or presence of walls, can be a challenge. If one looks at a billion, or even a few thousand cells in a milliliter of solution, the challenge grows significantly even if cell-cell and cell-protein interactions are disregarded. Beyond that, the physics of the cell-cell interaction has competing models and has not been exactly elucidated. The bridging model features cell-to-cell interaction due to adsorption of macromoleculars onto adjacent surfaces. It has been observed that red blood cells suspended in just buffer, not a protein-filled plasma, shows very limited cell-to-cell interactions, if any at all.[119] The other depletion model focuses on an osmotic gradient created when two cells are near each other, causing a localized decrease in protein concentration.[132-134]

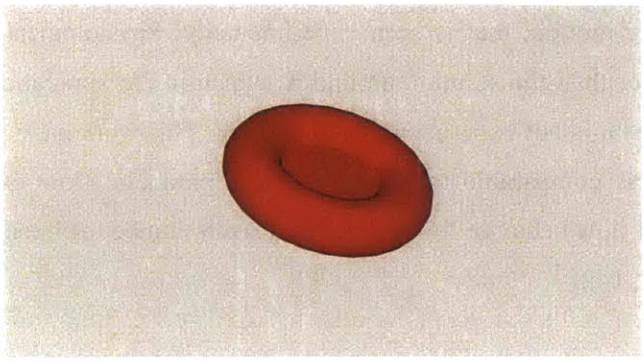

**Figure 6-1** A drawing of a typical red blood cell shape under no stress. The cell is discoid, with diameter around 6-8 μm and thickness of 2 μm near the edges, and 1 μm in the center.

Majority of the literature models plasma as an incompressible Newtonian fluid with a suspension of cells or vesicles. When the initial design of this project began, the numerical analysis in the literature featured at most 100-1,000 cells, with the assumption that the cells are rigid, or are elastic capsules.[135, 136] If any interactions were taken into account, the cell number that could be studied significantly dropped to 100 cells or less.[137, 138] All of these studies compared this behavior to experiments using only qualitative methods. The numerical methods presented new interaction behavior modeling, but are not yet able to predict experimental results. More recently, 512 deformable cells were simulated between two glass plates, 9 mm in diameter and 30 μm apart. The study compared the shape of the cell to experimental photo captures, as well as simulated aggregation formation for 10 $s^{-1}$, 60 $s^{-1}$, and 100 $s^{-1}$ shear rates. This study took 26 days of CPU time, on 96 cores, and showed that there was very limited aggregation for 100 $s^{-1}$ shear rates, but did not provide much insight beyond that.[134] The group combined finite volume methods for flow calculations, with finite discrete elements for the cell shape, as well as compared multiple cell-to-cell interaction models in a qualitative manner.

There has been further study of red blood cell shapes and alignment in similar channels to our system (around 30-40 μm in height), comparing cell curvature profiles near the wall vs. near the center.[139] More recently, there has also been work on hydrodynamic interactions of the cells near the channel wall. This study focused on Couette flow (shear flow where one wall is stationary while the other is moving) at near zero Reynolds numbers for quantifying cell free region for both spherical and aspherical vesicles.[140] The model had to use the same viscosity between the solution and vesicles in order to qualitatively reproduce cell tank

treading or swinging motion, that is seen experimentally. Physiologically, cell viscosity is around 5 times larger than the solution around it, which in the simulation would cause cell tumbling (rotation) that is not experimentally supported. This work gave an approximate cell free layer which was comparable to pressure driven parabolic flow experimental results. Other Couette based flow behavior for vesicles or a small number of interacting cells has also been published.[141, 142]

Further understanding of the physical system and addition of details, higher Reynolds numbers, proper cell behavior modeling, cell-protein interaction, and other complexity is needed for the full model of blood behavior. Given the large number of contributing variables, strong dependence on geometry, plasma-cell, and cell-cell interaction, the system parameters grow in number quickly. Although the high detail, large scale analysis has shown great progress in our understanding of certain cell behavior in shear flows, there is still further work ahead in combining all of these methods for high density suspensions before these models can be used as predictive tools.

## 6.2 "Apparent Viscosity" Numerical Analysis and Our Designs

We chose to qualitatively model our separation system in order to get a general understanding of what angles, flow profile regimes, and parameters would provide stable and reproducible results. From our initial experimental results, it became clear that recirculation areas cause separation instabilities as the cells get trapped in the recirculations and get pulled into the plasma channels. In order to have a better understanding which angles and flow profiles gave us optimal results, we modeled "low detail" apparent viscosity flow profiles in these systems. We used this low detail simulation as a very approximate guide, since cell presence would disturb the flow profiles and can significantly alter flow behavior.

Blood is shear-thinning, meaning apparent viscosity decreases as the shear rate increases. The overall viscosity reaches Newtonian behavior whenever the shear rate is over 100 $s^{-1}$. Our design features an inlet with a 30 μm wide constriction, and an average velocity of around 0.555 m/s, which leads to initial high shear rate of 18,000 $s^{-1}$. This shear rate drops off dramatically, however, as the channel expands, and that is the region we are most interested in. Therefore, we looked for a model that could reproduce the high shear Newtonian viscosity

value, but would also be accurate for low-shear or possibly stagnation regions at the expansion of the channel. Due to these requirements, we chose to model our system using the Careau model, which is defined by the equation:

$$\eta = \eta_\infty + (\eta_0 - \eta_\infty)(1 + (\lambda\dot{\gamma})^2)^{\frac{n-1}{2}}$$

**Equation 6-1**

where $\eta$ is the apparent viscosity, $\eta_\infty$ is the viscosity at high shear rate or the viscosity of the "Newtonian regime" and is equal to 0.0035 Pa·s, $\eta_0$ is the viscosity at zero shear and is set to 0.056 Pa·s, $\lambda = 3.313\ s$ and n=0.3568 based on previous literature, and $\dot{\gamma}$ is the local shear rate.[143, 144] We applied this model using a finite element solver in Comsol Multiphysics. The results gave us an approximate range of stable flow rate values for a range of designs, which was then used to support the experimental analysis and design as described in CHAPTER 5. In order to study a wide range of angles, flow rates, channel dimensions, and channel resistances, we set up an automated Matlab and AutoCAD system. The device designs were all defined in AutoCAD, the parametric sweep of model parameters were defined in Matlab, including boundary conditions etc., all of these components were uploaded into Comsol, and were run one after the other through the Matlab LiveLink System. An example flow profile for water vs. undiluted blood viscosity is presented in Figure 6-4. The Matlab code used for a typical Comsol model is presented in Section A.4.

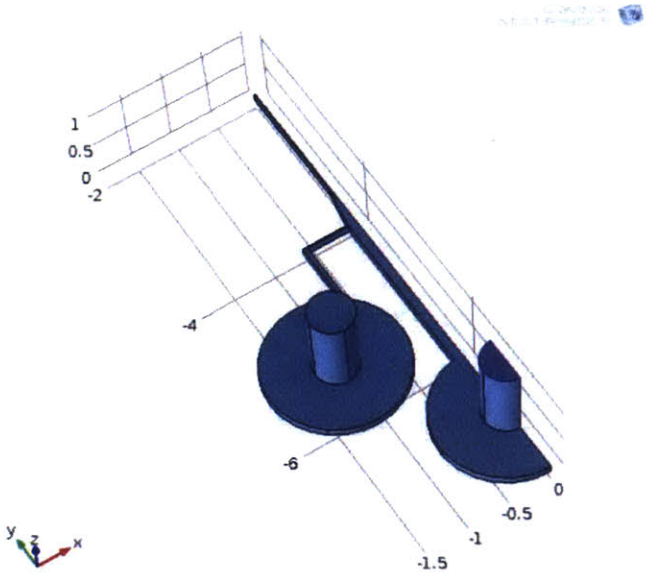


**Figure 6-2** A typical representation of the 3D Comsol design – inlet flow coming from the top. The design outlets can be defined using either resistance values, or can include microfluidic channel-tubing connections as depicted above.

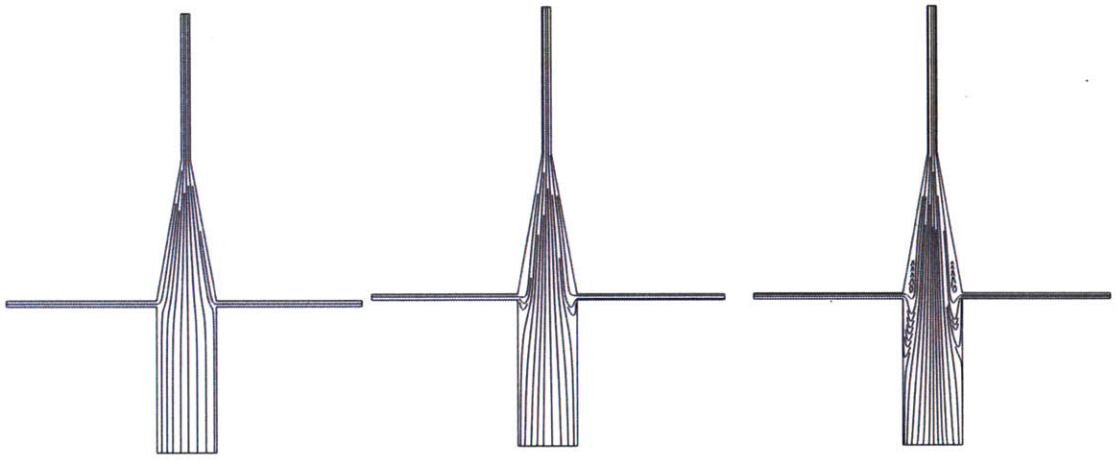

**Figure 6-3** Streamline depiction of a 2D cross-section of an expansion channel. Moving from left to right is a typical evolution of disturbances and recirculation areas with increased flow rate.

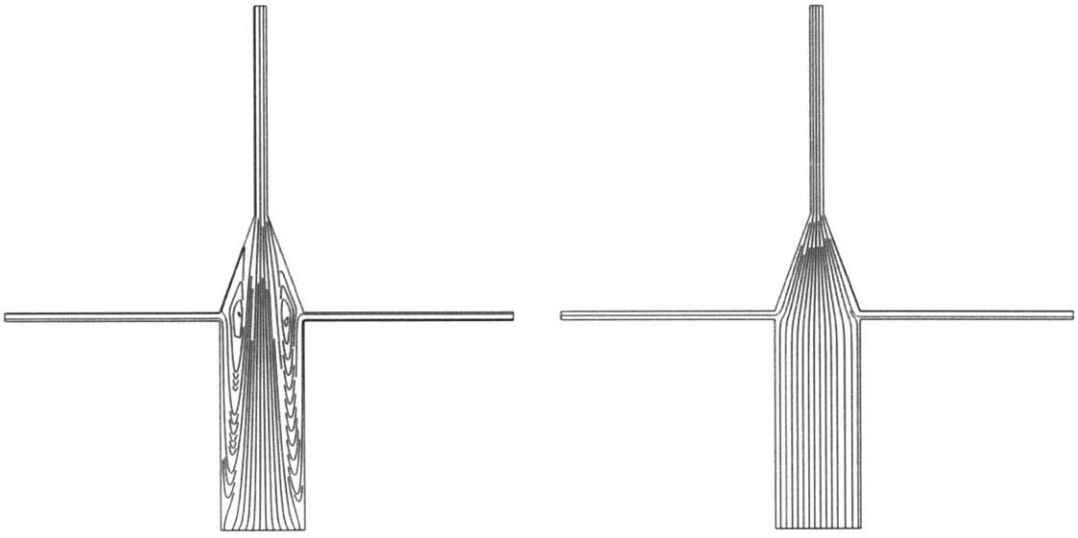

**Figure 6-4** Streamline comparison of water (left) vs. modeled blood viscosity (right) flow at high flow rates. The apparent blood viscosity model under-predicted the recirculation instabilities that were seen experimentally.

Although the Carreau model gave approximate stable system regimes, the model under-predicted the flow disturbances at the expansion region. We applied the modeling results as a guide for which expansion angles (5-30°) and flow rates did not produce expansion vortices. As we saw in CHAPTER 5, expansion angles of 5-20° were the most promising for our separation results. This is consistent with the model under-prediction of the flow vortices that were experimentally seen at expansion angles larger than 20° for ten times diluted blood, and for angles larger than 15° for 3 times diluted blood.

## CHAPTER 7. PORTABLE EXPANSION DESIGN STUDY

Although microfluidic devices tend to be small in footprint, the greatest burden is the macro-scale equipment required to drive flow through the system, or provide power or light capture for sensing analysis. The separation results in previous chapters were collected using the microfluidic device, tubing, and one syringe pump. The syringe pump produces precise flow rate control, and allows for optimization of system settings in the study of each expansion angle. For undiluted blood, we observed that the 5° expansion gave us significant improvement over the literature and was not sensitive to flow rates within a certain range.

In order to eliminate the syringe pump, we tested the separation capabilities by loading the (diluted) blood onto the device by hand. This minimized the separation device footprint to the microfluidic chip, tubing and collection tubes. Plasma separation was slightly better whenever the sample was loaded at a steady pace, instead of intentionally varying from fast to slow. For undiluted blood, separation was improved when the flow rates were slightly slower, whenever the hand applied light pressure to the syringe. We were able to collect consistent separation data even when the device was pushed by hand. As seen in Figure 7-1, the data are significantly above the separation values in literature, all of which require a syringe pump(s).

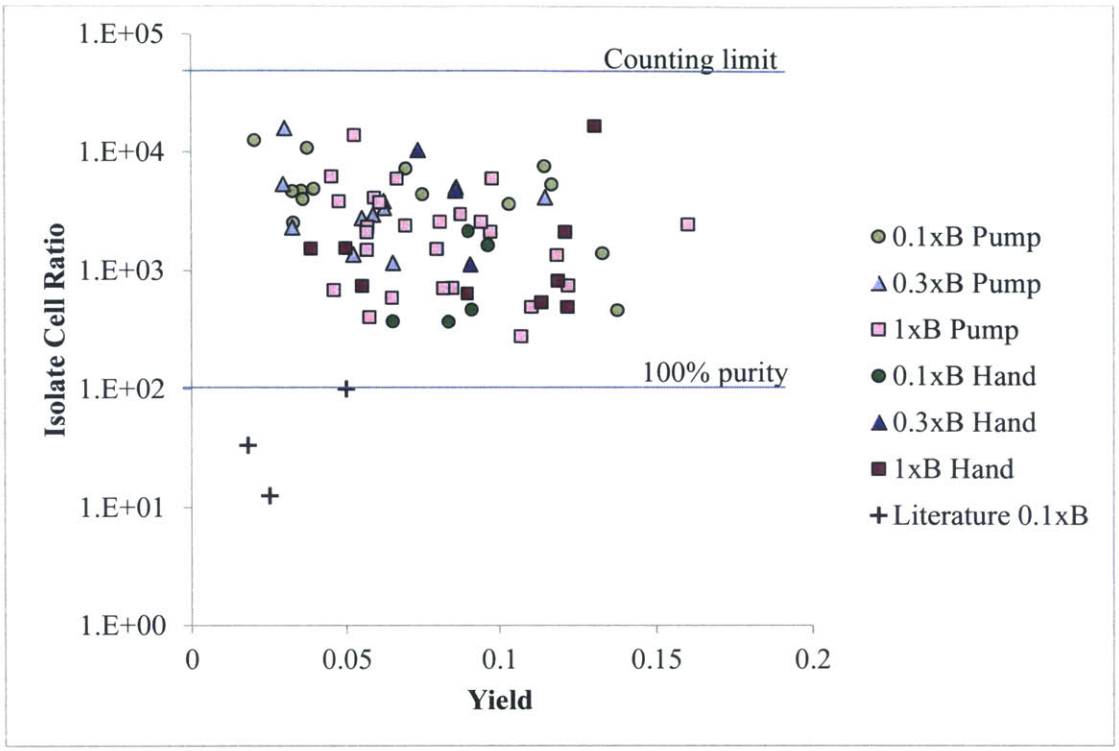


**Figure 7-1** 5° Expansion syringe vs. hand separation results, highlighting system robustness and portability. The data show 10-100 times improvement over literature results which require a syringe pump.

By studying a range of expansion angles after a channel constriction, we were able to significantly improve blood plasma separation when compared to literature results. These expansion ranges helped us find robust optimum settings such that the expansion is harsh enough to temporarily increase the cell free layer at the expansion, but is not too harsh such that vorticity comes into play. After this experimental study, we believe the vortices significantly reduce the reproducibility of data and separation. By focusing on flow rates around 100 μL/min, while ensuring minimal lysing, we were able to build a system that could be incorporated with a wide range of microfluidic or benchtop sensors. Thus, the expansion separation device is a step forward in the design of whole blood based point of care medical devices.

# CHAPTER 8. PORTABLE COLORIMETRIC PROTEIN SENSING

## 8.1 Colorimetric CRP Sensing

Portable colorimetric sensor constructs were evaluated for phone-camera based readout, as a possible point of care sensor addition to the blood separation system. The initial sensor design was for a c-reactive protein (CRP), which is an inflammatory cytokine released during tissue injury, infection, cardiovascular disease, chronic diseases, tissue rejection during surgery, etc. CRP concentrations can go up quite significantly. For example, for cardiovascular disease, a concentration of below 1 μg/mL is considered low risk, 1-3 μg/mL average risk, and anything above as high risk.

Initial work focused on FITC-glucose model solutions in order to set up reproducible camera readouts. Blue LEDs were aligned using LED holders and filtered for the FITC-excitement wavelength, while the phone camera was also placed behind a filter in order to eliminate any LED and minimize ambient light. A box with a black tarp helped limit the variations due to external light, and the camera settings were controlled using a Camera FV-5 application, which allows for manual settings.[145] Although this setup was promising for standard FITC-glucose solutions, the fluorescence signal was too weak for surface enzyme-linked immuno assay (ELISA) measurements of FITC labeled goat anti-CRP in PBS.

In order to amplify the signal and to better mimic the FITC-glucose solution standards, a colorimetric enzyme-based approach was pursued. The horseradish peroxidase enzyme (HRP) and a chromogenic substrate (3,3',5,5'-Tetramethylbenzidine, TMB), which acts as a hydrogen donor in the reduction of hydrogen peroxide to water, resulting in a blue diimine solution, was chosen. In this system, an anti-mIgG-HRP was added as the third antibody on top of the sandwich ELISA setup, as detailed in McGeough, C.M. et al.[76, 77]

For this setup, a lamp with natural light was applied from around a 50 degree angle, while the camera captured the photos from above. The sensing experiments were performed in 96 well plates, since the sensing procedure is more readily available for a batch system. A range of antibody concentrations, as well as HRP concentrations were tested, and both ultra-sensitive and regular TMB were used. Unfortunately, despite the variation of concentration, and the addition of extra washing steps, as well as Tween20 soaks, the background signal always

produced a visible color, and the wells containing proteins would often be spotty. A general trend of intensity in color would be seen for increasing CRP concentrations (Figure 8-2), implying at least partial success of the sandwich ELISA. However, the results were not reproducible and the colored background signal made it hard to differentiate the sensing response, given the limited optics of a phone camera. The results were improved with the channel-splitting of signal in ImageJ, as well as averaging of signal over the entire well, but the reproducibility of the calculated values was still an issue. It is unclear whether an alternative enzyme-system would be beneficial given that other enzymes can be sensitive to blood anticoagulants, such as EDTA, or other proteins in the blood plasma.[146] The addition of blood plasma could further complicate the signal differentiation and would possibly limit the sensitivity of the system. Therefore, the enzyme-based cell-phone camera systems were not pursued further.

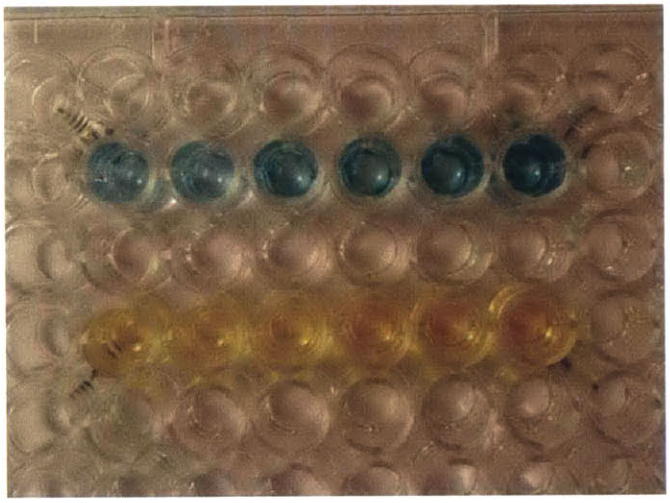

**Figure 8-1** Typical photograph of the colorimetric readout using a halogen lamp at 50° to the surface. The CRP concentration increases as one moves to the right, with the most left well is the background for both rows. The top row presents the blue diimine before the stop solution (HCl) is added. The bottom row is after the stop solution is added.

## 8.2 Malaria Colorimetric Sensing

Shefali Lathwal in the Professor Hadley Sikes Group has led the development and published a colorimetric *Plasmodium falciparum* histidine-rich protein 2 (PfHRP2) detection system on modified chromatography paper.[75] PfHRP2 protein is released in the blood stream during a malaria infection, and has been clinically used for disease detection.[147]

An aqueous oxidizing agent is used to convert some of the hydroxyl groups of cellulose to aldehyde groups. The paper is then taped to normal printer paper for support, and is covered with a wax layer on top using a Xerox Color Cube printer that uses solid ink. After printing, mild heating step is used to distribute the ink throughout the width of the chromatograpgy paper, leaving 3 mm diameter circular reaction regions. The reaction regions are spotted with the antibody of interest, and are then exposed to either the protein of interest or to a control sample with no protein. Then, using a typical sandwich ELISA method, a reporter antibody with an eosin tag is used for fluorescence measurement.

For colorimetric detection, an aqueous amplification solution with a pH of 7.9 was used, containing poly(ethylene glycol) diacrylate (PEGDA), triethanolamine (TEA), 1-vinyl-2-pyrrolidine (VP), phenolphthalein, and free eosin. The eosin and the tertiary amine (TEA) are the photoinitiators for the PEGDA-VP polymer, and can overcome oxygen inhibition and produce a colored polymer (with phenolphthalein) in under 100 seconds using LED light centered at the $\lambda$=522 nm, with 30 mW/cm$^2$. The polymerization time is chosen based on fluorescence of the control sample, so that the polymer controls are colorless. The pH was adjusted to be below 8 using hydrochloric acid to ensure that the phenolphthalein was colorless initially and eosin was the dominant photoinitiator absorbing light. After polymerization and wash steps, NaOH was added to raise the pH of the solution, and the results were imaged either by eye or using a cell phone camera. The full details of the procedure are written in the supplementary information of reference [75]. This system was applied to both buffer and blood serum systems. Blood serum is the liquid portion of blood (plasma) without any clotting factors.

## 8.3 Plasma Separation and Colorimetric Malaria Detection

We combined the colorimetric malaria sensing system with the blood plasma separation system in order to further the applicability of our system. The pfHRP2 protein was added to whole blood, based on the measured plasma volume. The cell volume in blood can vary between sexes and from person to person between 40-60%, approximately. Undiluted blood plasma was separated using our 5° expansion angle microfluidic device. For a high number of concentrations, multiple devices were run in parallel to minimize collection time.

Concentrations of 5-130 nM (or 0.38-10 μg/mL, respectively) were tested in whole blood. The protein was spiked into the whole blood based on plasma volume, not the total blood volume (procedure outlined in Section A.2.5). Plasma volume was calculated for each experiment, since it can vary between 40-60% of the total blood volume. The blood plasma containing the protein was then separated out using the blood separation device, and collected into Eppendorf tubes. The plasma was used on the paper sensing device, the fluorescence was read out on a microscope, and the polymer amplification color was captured using a cell phone camera. Fluorescence data are shown in Figure 8-3, without the subtraction of the background signal. Each concentration was replicated 3 times, while the background was replicated 9 times. We show significant sensor response even below the clinical standard of 28 nM.[147]

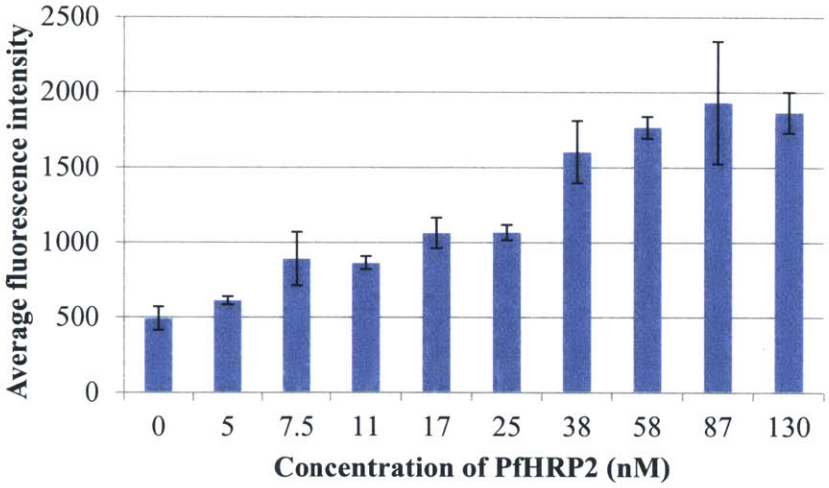


**Figure 8-2** Fluorescence readout from the eosin that is covalently attached to the second antibody, in a typical ELISA-sensing scheme. The error bars represent one standard deviation.

We also calculated the fluorescence data after subtraction of the background signal. The standard deviation for the subtracted values was done using the pooled variance calculation, given that the background and experimental data have different number of repeats:

$$s_p^2 = \frac{\sum_{i=1}^{k}(n_i - 1)s_i^2}{\sum_{i=1}^{k}(n_i - 1)}$$

**Equation 8-1**

where $s_p^2$ is the pooled variance (pooled standard deviation would be $s_p$), k is the number of sets we are combining (in our case it is only 2 – background and our measurement), $n_i$ is the sample size of the population set i (which equals 9 for background and 3 for our measurements), and $s_i^2$ is the variance of the population set i. Our equation simplifies to:

$$s_p = \sqrt{\frac{8 \cdot s_{background}^2 + 2 \cdot s_{sample}^2}{10}}$$

**Equation 8-2**

This equation calculates the standard deviation of each sample point minus the background value, which we plot below in Figure 8-4, on the logarithmic and linear scales.

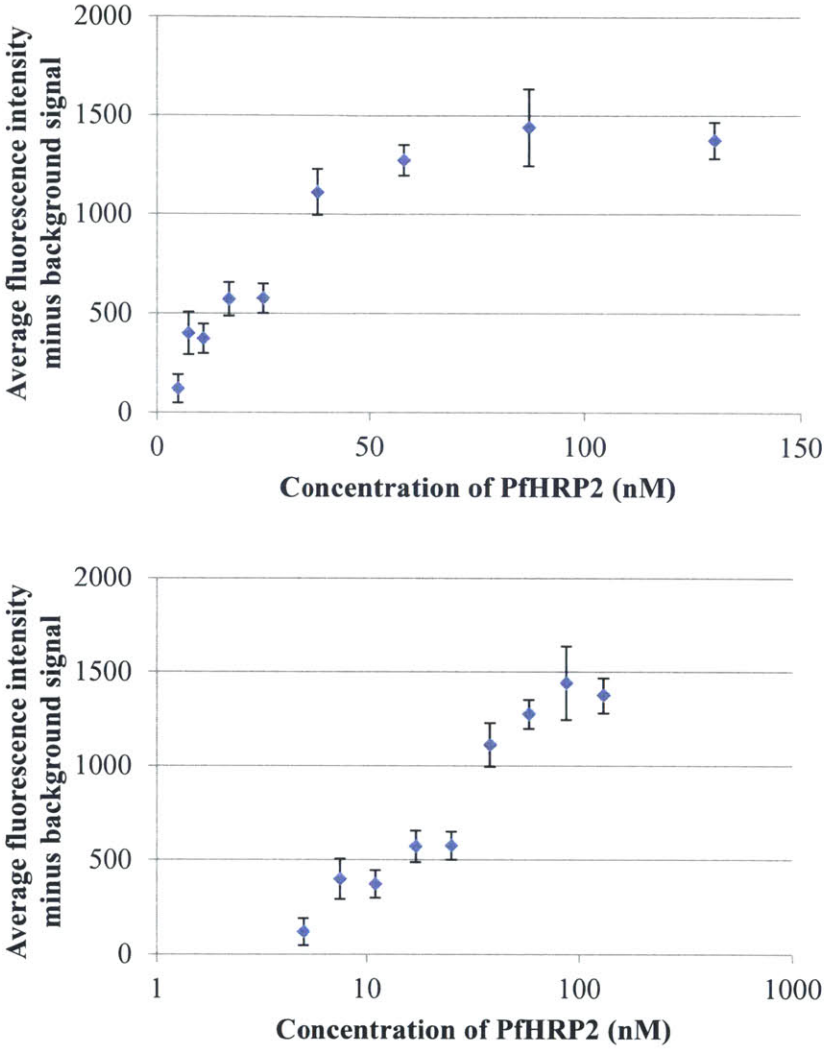


**Figure 8-3** Fluorescence sensing data with background subtracted from the data,+/- 1 standard deviation is calculated using a pooled variance approach.

We also tested the statistical significance of each measurement. Given that the background measurement had 9 repeats while the rest of the measurements only had 3, and given that the measurements have different variances, we used the unpaired Welch's t-test to calculate our t-values:

$$t = \frac{\overline{X_1} - \overline{X_2}}{\sqrt{\frac{s_1^2}{N_1} + \frac{s_2^2}{N_2}}}$$

**Equation 8-3**

Where $\overline{X_i}$ is the sample i mean, $s_i^2$ is the sample i variance, and $N_i$ is the sample size (number of repeats). For the p-value we also had to define the effective or "pooled degrees of freedom" using the Welch–Satterthwaite equation:

$$\nu_{effective} = \frac{\left(\frac{s_1^2}{N_1} + \frac{s_2^2}{N_2}\right)^2}{\frac{s_1^4}{N_1^2(N_1 - 1)} + \frac{s_2^4}{N_2^2(N_2 - 1)}}$$

**Equation 8-4**

Then we calculated the 1-tail p-value in order to decide whether the measurement of a higher concentration is statistically significant (95% confidence interval) when compared the measurement of one concentration lower, summarized in Table 8-1. The 5 nM fluorescence measurement was found to be statistically significant when compared to background. Not all the measurements were statistically significant when compared to one concentration lower, but all were observed to be above background value for a 95% confidence interval. Limit of detection was defined as the background signal plus three standard deviations of this background signal, which gives us a fluorescence value of 728, therefore setting the fluorescence limit of detection at 7.5 nM.

| Concentration of pfHRP2 (nM) | Average Fluorescence | Std Dev of Fluorescence | P-value Vs Background | P-value vs. Adjacent Lower Concentration |
|---|---|---|---|---|
| 0 | 492 | 79 | | |
| 5 | 612 | 25 | 0.0013 | 0.0013 |
| 7.5 | 891 | 179 | 0.0265 | 0.0557 |
| 11 | 865 | 44 | 0.0000 | 0.4125 |
| 17 | 1063 | 102 | 0.0019 | 0.0305 |
| 25 | 1067 | 52 | 0.0000 | 0.4774 |
| 38 | 1603 | 207 | 0.0044 | 0.0199 |
| 58 | 1767 | 72 | 0.0000 | 0.1528 |
| 87 | 1932 | 408 | 0.0123 | 0.2783 |
| 130 | 1866 | 136 | 0.0007 | 0.4059 |

**Table 8-1** Concentration of PfHRP2 vs. p-value for the 1-tail unpaired t-test. P value of less than 0.05 shows statistically significant difference between the current concentration fluorescence measurement and the lower or background point (assuming 95% confidence interval). This data show that the 5 nM fluorescence measurement is statistically significant when compared to the background measurement.

The colorimetric readout results for the polymer amplification system, described above are shown in Figure 8-5. The photographs were captured with a cell phone camera. Visual limit of detection is approximated to be around 11 nM where all of the replicates show clear polymerization. This concentration is below the clinically relevant concentration of 28 nM. For calculated limit of detection, we repeat the method above and define it as the background value plus three times the background standard deviation, which gives us the calculated limit of detection of 7.5 nM, the same detection limit as the direct sandwich ELISA fluorescence measurement. These results provide clear detection of malaria by visual methods, without any external equipment or power sources requirements, except for low power LEDs.

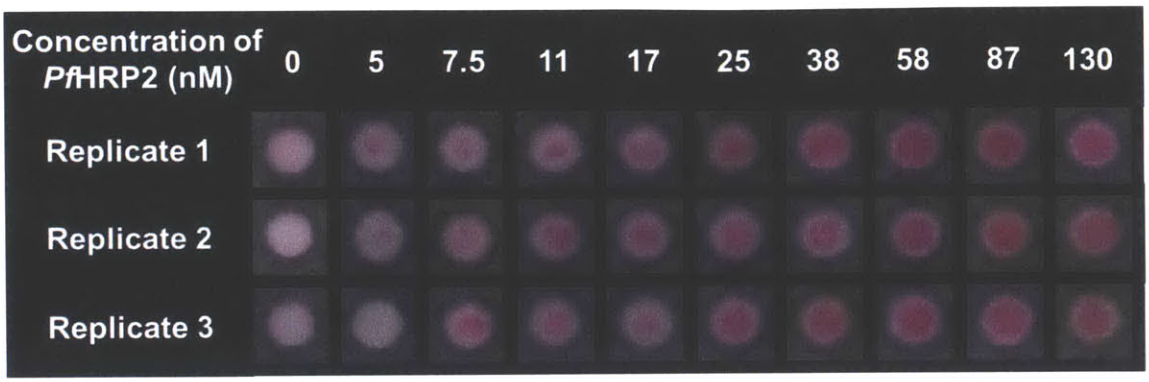


**Figure 8-4** Colorimetric readout of the PfHRP2 protein in plasma after plasma separation in the microfluidic device, in undiluted blood.

The exact color intensity values were acquired using ImageJ software and are plotted in Figure 8-6 and Figure 8-7. These values were also used for statistical analysis as described above, and are summarized in Table 8-2. There is some higher sensing variation and higher background in fluorescence when compared to published serum measurements, but that is to be expected for this more complex system and biological sample. The higher background signal required shorter polymerization time for plasma measurements, and hence contributed to the higher limit of detection. Some of the variance could also be due to the blood plasma volume measurement, possible variation in blood cell count when diluting protein into small blood sample sizes, as well as some protein loss due to attachment to the device, blood cells, or other surfaces. The colorimetric system shows comparable sensitivity (7.5 nM limit of detection vs. serum 5.8 nM limit of detection) and presents malaria detection at concentrations below clinically relevant levels.

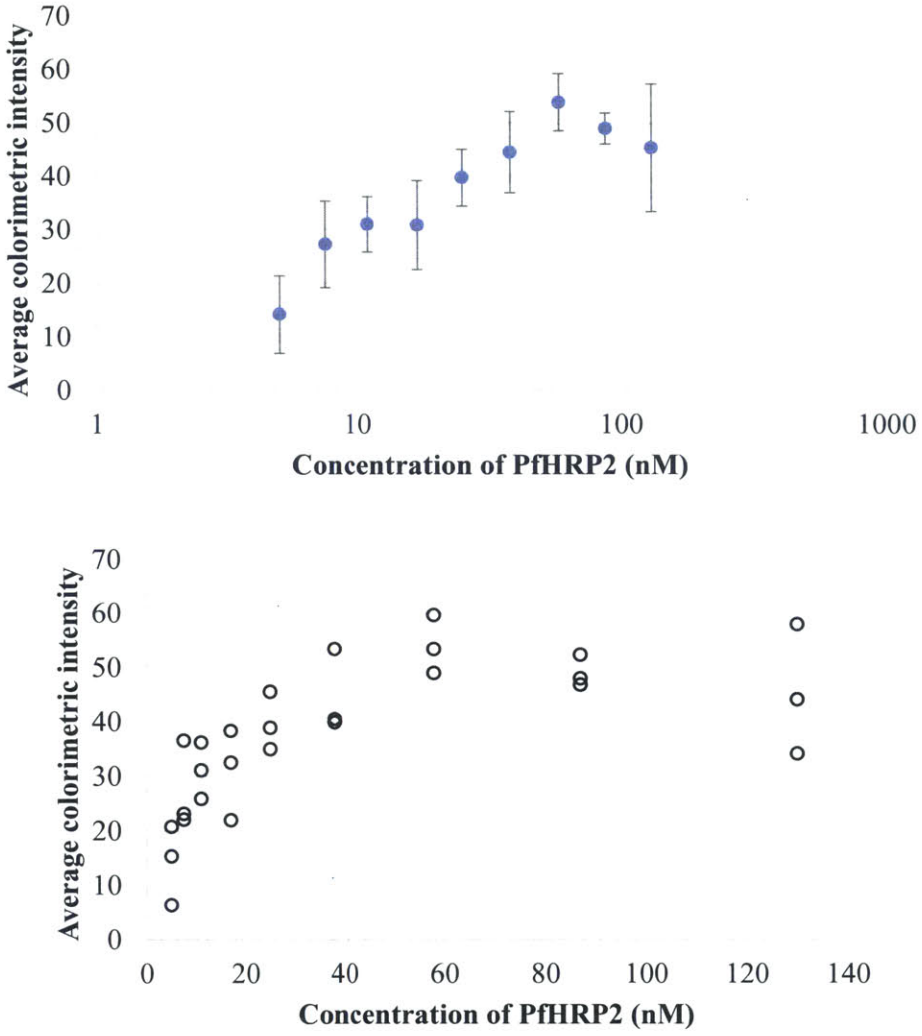


**Figure 8-5** Colorimetric intensity measurements using ImageJ software.+/- 1 standard deviation for the graph above, and each replicate plotted separately for the graph below.

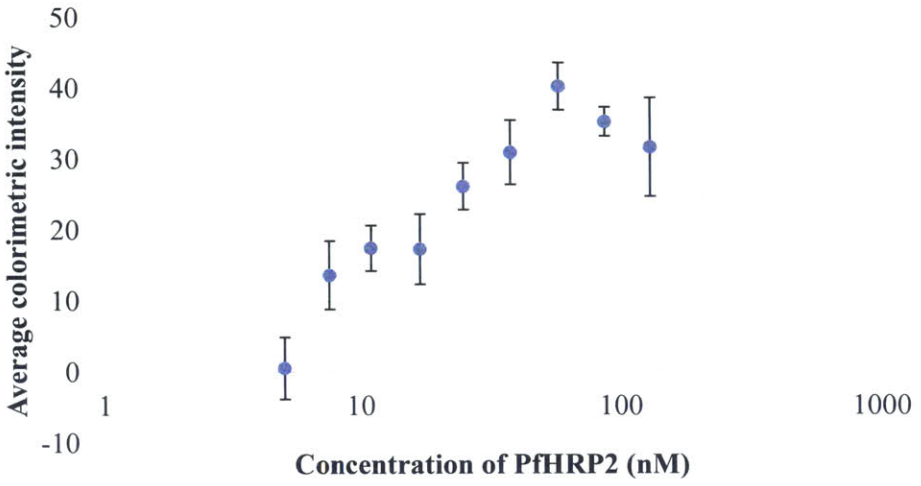


**Figure 8-6** Colorimetric sensing data with background subtracted from the data, using pooled variance.

| Concentration of pfHRP2 (nM) | Average Colorimetric Intensity | Std Dev of Colorimetric Intensity | P-value vs. Background |
|---|---|---|---|
| 0 | 13.60 | 2.02 | |
| 5 | 14.14 | 7.26 | 0.4554 |
| 7.5 | 27.24 | 8.09 | 0.0461 |
| 11 | 31.04 | 5.18 | 0.0088 |
| 17 | 30.91 | 8.32 | 0.0309 |
| 25 | 39.78 | 5.33 | 0.0036 |
| 38 | 44.57 | 7.62 | 0.0073 |
| 58 | 53.97 | 5.37 | 0.0012 |
| 87 | 49.02 | 2.91 | 0.0001 |
| 130 | 45.39 | 11.96 | 0.0204 |

**Table 8-2** Concentration of PfHRP2 vs. p-value for the 1-tail unpaired t-test. P value of less than 0.05 shows statistically significant difference between color intensity and background. Concentration of 7.5 nM and above was found to be statistically above the background value.

## 8.4 Micro Total Analysis System

Micro total analysis systems (μTAS) promote the idea of designing small-scale, portable, devices with every major step completed on-chip. The initial motivation for blood plasma separation on-chip using a passive method is to create a system that is adaptable with a wide range of small-scale sensors. Ideally, a system that is portable, low power, and does not require any hospital or laboratory equipment for readout is the goal for a point of care diagnostic systems.

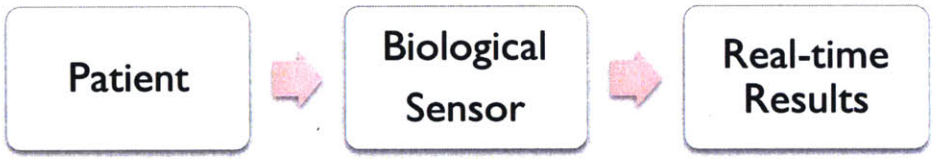


**Figure 8-7** Ideal sensor setup, where a portable, biological sensor gives real-time results at patient bed-side, without the need for external pretreatment or large equipment.

By studying a wide range of angles and flow rates, we were able to design a system that allows for blood plasma separation by hand. The plasma collected from the device was used for a portable colorimetric malaria detection system that showed visual detection of the malaria protein for concentrations of 11 nM and a calculated limit of detection of 7.5 nM. This result aligns well with the clinical test that measure the presence of this malaria protein in plasma for the concentrations of 28 nM and above.[147] And shows great progress towards clinically-relevant microfluidic constructs.

# CHAPTER 9. AMPEROMETRIC CARBON NANOTUBE SENSING

Carbon nanotubes (CNT) have 1-D electronic structure and any surface interaction with a biological entity significantly changes cross-sectional conduction property of the material.[148-150] In collaboration with Jonathan Weis in Professor Timothy Swager Group, we developed a drop-wise deposited carbon nanotube construct, which allows for an incorporation of CNT sensing components in microfluidic devices.[102, 151]

## 9.1 Microfluidic Setup

The sensor design contains 14-electrode pairs evaporated onto a standard microscope slide. Each electrode pair is either 300 μm or 1 mm apart and a suspension of pristine or modified carbon nanotubes were deposited between each pair, as seen in Figure 9-1. These droplets contain conductive carbon nanotube meshes that are very sensitive to their environment, since carbon nanotubes are made up of all surface atoms. The device is then plugged into a breadboard and the electrodes are kept at a constant bias during the exposure. The current measurements are acquired using PSTrace or Uniscan Software and then normalized using Matlab to present change in conductance vs. time for the data analysis:

$$-\frac{\Delta G}{G_0} = \frac{I_0 - I}{I_0}$$

**Equation 9-1**

where $\Delta G$ is the change in conductance, $G_0$ is the initial conductance, $I_0$ is the initial current, and I is the current during the experiment. Conductance, G, is defined as $G = I/V$, where V is the voltage bias for the system. Using literature as guidance, we studied a 0.01-0.5V range for voltage bias in this system, as well as a large salt concentration range. We chose to focus on 100 times diluted PBS, or 0.150 mM PBS, in order to increase the CNT response to charge near the surface (this value is close to the literature values of 15-100 times dilutions). We did not find a difference in the type of response based on the bias, only the intensity of the response change, therefore we chose to use 0.1V as our voltage bias.

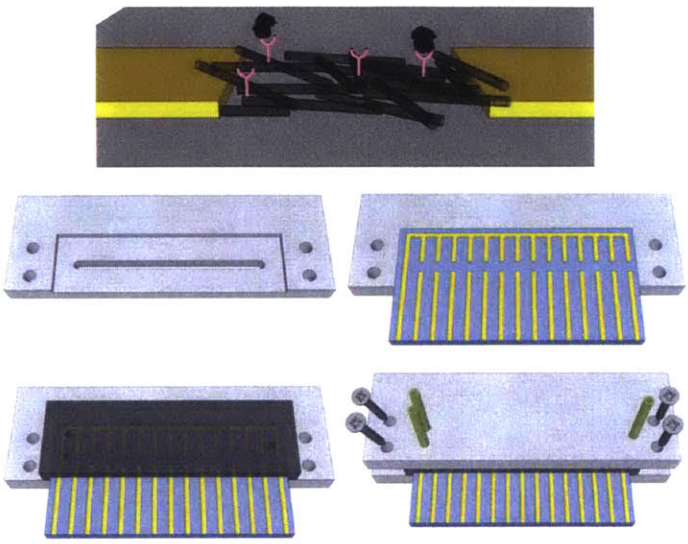

**Figure 9-1** Final setup of the microfluidic biosensor. On the top is the visualization of a mesh of carbon nanotubes deposited between each electrode pair. These CNTs can be modified with a linker and an antibody of interest in order to sense the presence of the respective protein. The final design of the chuck is depicted. The bottom component has a viewing window to ensure proper channel alignment. Then the glass with deposited electrodes along the with the PDMS T-channel device are added. And finally the top chuck component is attached. The top contains holes for inlet and outlet tubing.

A detachable microfluidic setup was chosen in order to allow for sensor reuse and exchange, without the need to manufacture new components. Polydimethylsiloxane (PDMS) was the material of choice due to its low-cost, biocompatibility, and easy evolution of designs. Initially, we chose to do a T-type channel in order to switch between two solutions of interest (such as analyte and a buffer or two analytes). In order to minimize CNT-PDMS channel interactions, the design featured a 2 mm wide channel that spanned the entire glass slide. The PDMS device was attached onto the glass slide using glass-slide supports and binder clips or C-clamps, but we found the system unstable, prone to leaking, and prone to CNT-stamping onto the channel. This temporary attachment method can be applied for many microfluidic devices in low-pressure applications, but was not sufficient for this 18 mm long channel, which required even compression throughout the entire glass slide.

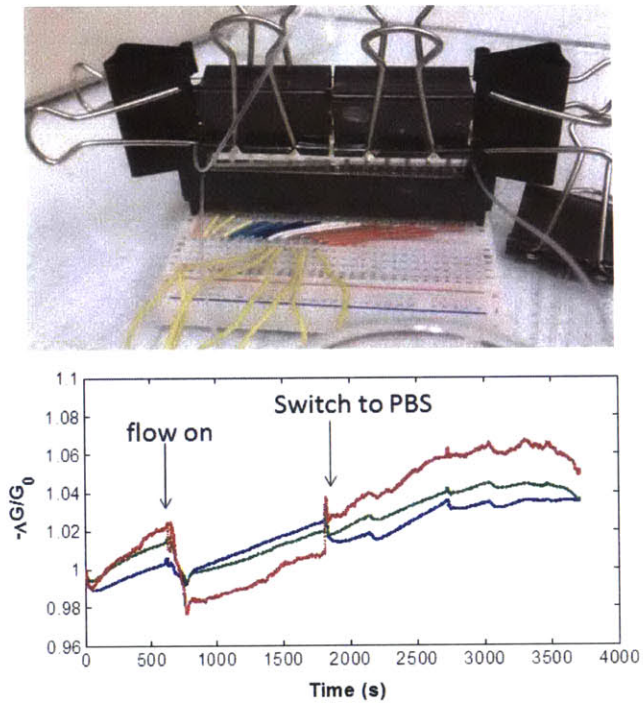


**Figure 9-2** Initial binder-clip setup, attached into the breadboard using an edge connector. Typical unstable results due to the binder clip setup, with a cyclic pump variation due to solution pushing instead of pump pulling.

In order to minimize the noise and to more evenly-attach the PDMS device to the glass, an aluminum chuck was designed, as depicted in Figure 9-1. Due to the long channel design, we had to use a metal material that would not bend under pressure from the four endpoints. Further support was provided through incorporation of glass within the PDMS device. We found no need for any gaskets after the PDMS crosslinking procedure was optimized so that the device was flexible enough to attach to the chuck, but strong enough to eliminate CNT stamping or loss, assuming a reasonable shear rate. After the system was optimized and we made sure that the PDMS device would not shift during the experiment, we were able to design a PDMS channel that was only 500 μm wide for the sensor design featuring a 1 mm gap between the electrodes. This allowed us to isolate the CNT-analyte interactions and cover the electrode-CNT junctions with the PDMS device, thus removing the junction from the response system.[107, 149, 150]

We chose to pull solution through the T-channel, in order to further minimize any pressure build-up during the switching process and to eliminate the cyclic variation seen in Figure 9-2. Pulling solution has the added benefit of eliminating any sample leaking onto the electronics

of the setup. If there are any leaks due to improper handling of the chuck, or the inlet being too close to the glass edge, only air is pulled in and we do not see any solution movement. This provided a much more robust system, and we were eventually able to isolate the leak points mostly to the T-channel inlets, since they were closest to the edges of the chuck and glass-support. Therefore, the system was redesigned to contain just a straight channel, where the inlet tubing was fit into a Y-splitter, and two 3-way valves were incorporated in order to turn on/off flow for the two solutions. This is similar to the setup used for blood separation, and can be seen in Figure 9-3. After the optimization of the device setup and materials used, we saw minimal disruption in the signal when switching between solutions. Therefore we developed a stable, removable microfluidic system designed for multiplexed sensing.

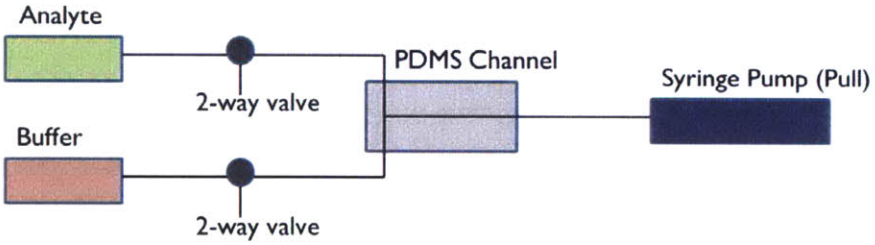


**Figure 9-3** Y-splitter setup for the PDMS microfluidic device. The syringe pump was set to pull the solution.

## 9.2 CNT Modification and Sensing

Once the signal was stable in a flow system, we functionalized the CNTs with biotin using an aminopropylaziridine linker, as depicted in Figure 9-4. The signal for the biotin-functionalized CNTs was compared to pristine CNTs, as well as linker-only functionalized CNT mesh signal. Although we would occasionally get a promising avidin-biotin response, the data were not reproducible and were often dominated by strong nonspecific response.

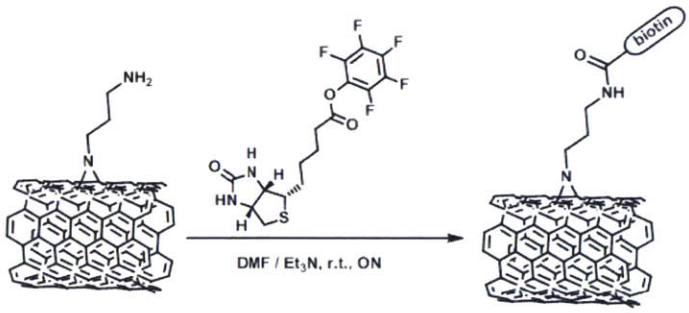


**Figure 9-4** Biotin-functionalized CNTs using an aminopropylaziridine linker.

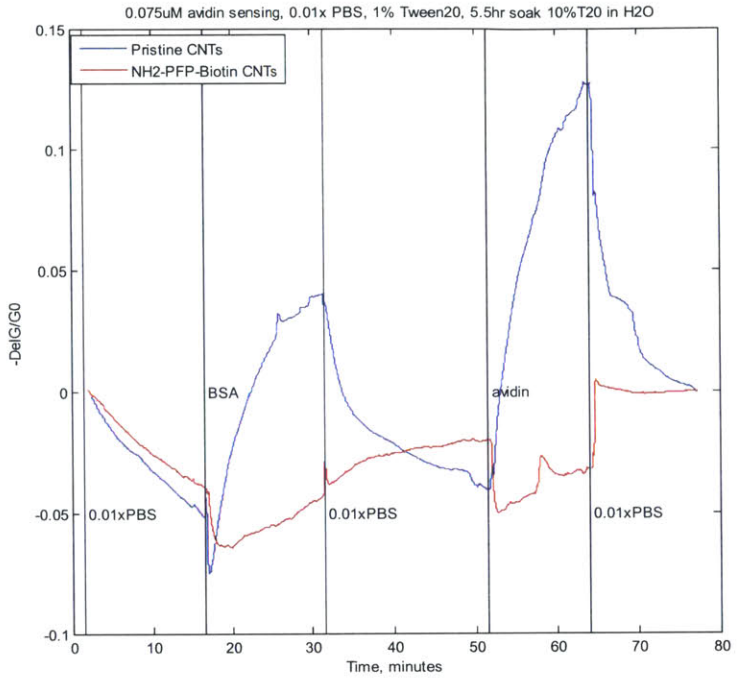


**Figure 9-5** An example of the data response comparing biotin-functionalized and pristine CNTs when exposed to a nonspecific protein (bovine serum albumin (BSA)) and to a specific protein, avidin. The data were often very noisy and not reproducible in not only the response amplitude, but also in the signal direction of the response.

In order to minimize nonspecific protein binding, we studied the coverage of Tween20 and Pluronic F127 on CNTs. Nonspecific binding of proteins occurs due to the irreversible interaction of the hydrophobic regions on a protein with the hydrophobic CNT surface. In order to isolate the selective response, the irreversible nonspecific binding is often retarded using either protein or polymer coverage of the CNT. Both Tween 20 and Pluronic 127 are triblock copolymers containing a hydrophobic region with hydrophilic polyethylene oxide chains. Both polymers are also found to irreversibly adsorb onto the CNT surface and to block nonspecific binding of proteins up to 1μM.[98, 114] Since our system has a simplified deposition of CNTs from a suspension, the exact procedure could not be replicated. Therefore, we tested a range of polymer solution w/v % as well as a range of adsorption times (10 minutes - 24 hours) .

We observed that the CNTs became very sensitive to flow disturbances and any rinse steps after about 2-4 hours in a polymer solution due to what we assume to be a slight increase in

CNT solubility. Therefore, in order to isolate the response signal for long polymer coverage experiments, we also used a static CNT sensing system where PDMS-based wells were clamped onto the glass device using a simple system of glass and binder clips, similar to the setup above. After CNTs were coated in polymer, the glass slide sensor was rinsed in water, the PDMS wells were attached, and buffer or polymer solutions were carefully added into the wells. We found that 0.1-1% w/v of polymer coating the devices for 30-90 min gave enough coverage to prevent nonspecific response, and limited disturbances introduced during flow or during the addition of solution to the well, thus allowing us to continue the use of a flow system (Figure 9-6). If the coating-time was too low, the CNTs would experience nonspecific binding. If the coating-time was too long or the polymer-concentration too high, the CNTs would be more soluble and we estimate that the polymer coating would no longer be a monolayer and thus would produce signal disturbance from any polymer movement due to flow.

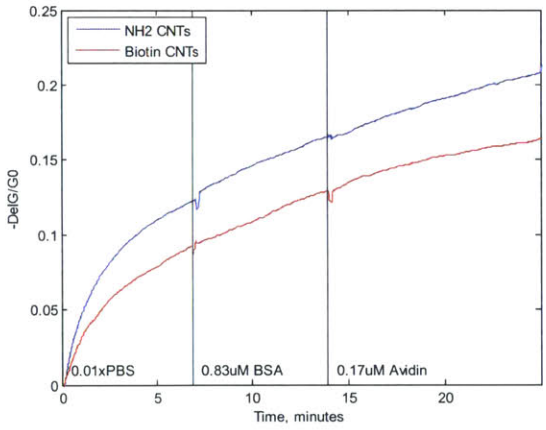


**Figure 9-6** Example data of CNTs coated in Pluronic 127 (1% soak for 60min with water rinse), showing resistance to nonspecific binding. Vertical lines indicate injection of the protein solution.

We tested specific versus nonspecific binding by coating both biotin-functionalized CNTs with an aminopropylaziridine linker and pristine CNTs with the polymers mentioned above. Although we could consistently block nonspecific response, we were not able to produce consistent specific response. When we used comparable w/v% of Tween20 and Pluronic 127 polymers for this setup, we observed that either both nonspecific and specific binding were blocked, or both nonspecific binding and specific binding were occurring.

In order to improve the specific binding response, we tested a similar setup as mentioned above using a pentafluorophenyl biotin linker but unfortunately did not find a consistent

selective response either. We therefore decided to functionalize the Tween20 itself with 1,1-carbonyldiimidazole (CDI), which could then be conjugated with biotin or a different biomolecule.[98, 113, 152] Although this occasionally produced selective biotin-responses, especially if the experiment initially injected BSA before avidin, the results are not reproducible and are far from being quantifiable. Two examples of the types of results that were collected are shown in Figure 9-7, each experiment compares the signal of a functionalized vs. control (polymer covered) signal channel.

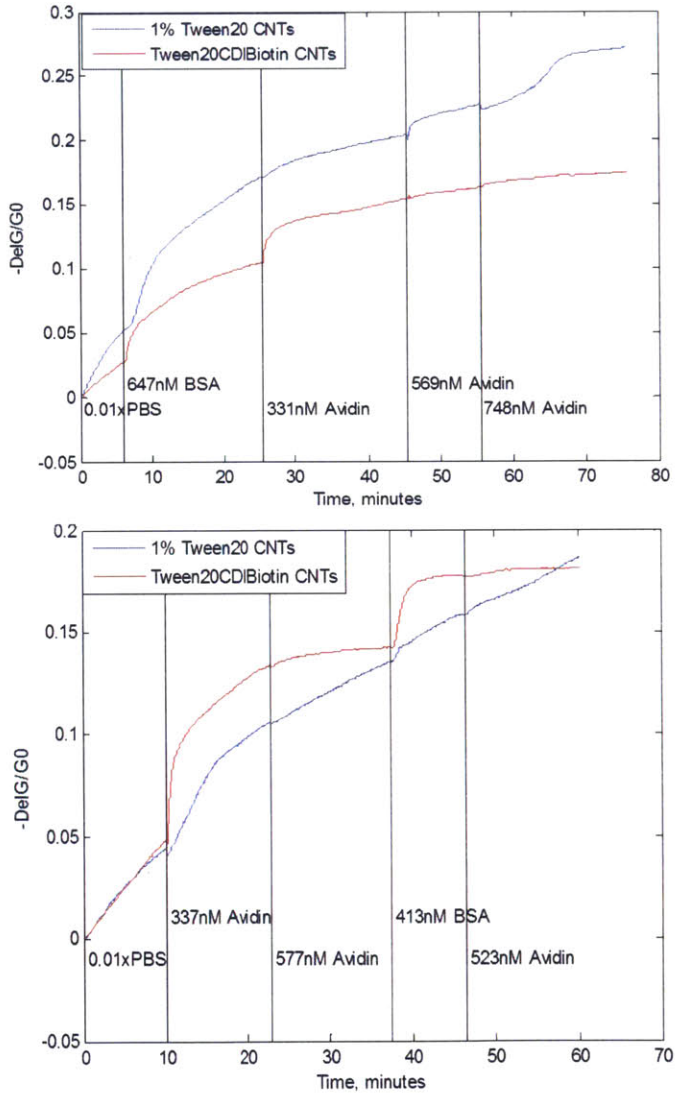


**Figure 9-7** Examples of conductance change of a biotin-functionalized vs non-functionalized CNT channels when exposed to bovine serum albumin (BSA) and avidin in 0.01x PBS diluted with water.

Despite multiple linkers, setups, variations in salt concentration, bias, and polymer coverage as well as surfactant buffers, the system did not provide reproducible sensing results. Unfortunately, the simplified CNT-deposition step also limits our ability to further control variables in this sensing system. Although the CNT-mesh provides a large surface area of interaction and is found to be very promising for gas-sensors developed in the Swager lab, this mesh intrinsically limits our ability to control the interaction-area of the CNTs and linkers, proteins, and polymers. If one attempts to properly cover the CNTs with surfactant while in solution, before deposition on the sensor surface, the CNT-mesh becomes a lot more hydrophilic and is often lost during gentle rinse steps, under flow, or can even lead to dominant signal disruption from small additions of sample into the static well-based design. The advantage of adding surfactant in CNT-solution, however, is that it ensures that the CNTs are all evenly distributed in solution after sonication and is less likely to cause polymer clumping on top of the mesh. Pristine CNTs can often begin to irreversibly clump together, depending on the solution handling and age of the suspension, which could be another variable in this system, although we did not find fresh CNT suspensions a sufficient fix.

If the surfactant is added after pristine CNTs are deposited onto the surface, it is very hard to ensure that only a monolayer of polymer was created, while making sure that the entire sensing region is covered. Also, if this mesh shifts after any flow or handling disturbance, other areas that were previously hidden and unmodified could be exposed to the solution. Whenever the CNTs are functionalized, their intrinsic conductance and solubility can be sufficiently altered, thus making it even more difficult to control for consistent resistances across a set of electrodes. Functionalizing after CNT mesh deposition can alter the overall resistance, as well, although we did not find that to be as big of an issue. If the resistances are of different orders of magnitude, however, the signal readout can be limited and noise would plague our analysis. The literature provides CNT-mesh examples, although the mesh was chemical vapor deposited, which allows for the control of a monolayer of CNTs. The CVD approach is a lot more complex than simple drop-wise deposition, but produces a high fraction (~70%) of semiconducting CNTs, which is the type that exhibits the most change in chemical or biological sensors.[98, 149, 150] Therefore, our setup could also be suffering from a low percentage or low control of the metallic vs. semiconducting CNTs, which can vary greatly between manufacturers and batches, and can strongly influence the cost of the material.

Overall, we found it very difficult to yield reproducible results. Although we have isolated the electrode-CNT junction with the PDMS device, thus isolating only the CNT interaction with the solution, the protein-CNT interaction and its effect on CNT conductance is still debatable. More recently, studies have noted that the conductance always decreases from protein binding, no matter what the net charge of the protein is at that pH (basic or acidic pI).[98] Beyond that, the system is very sensitive to salt conditions, very quickly losing sensitivity possibly due to the decrease of the Debye layer. Therefore our sensing study was conducted in 10-100 times diluted PBS buffer, and publications feature similar dilution values. Thus the CNT-based system is still limited for biological applications, especially for proteins sensitive to the salt concentration and would require a dilution of blood plasma.

Although CNTs provide a very sensitive construct, unfortunately they are sensitive to everything in their environment. The balance of specific vs. nonspecific binding is very delicate, if possible, and therefore requires further understanding of the types of interactions and mechanisms between CNTs, polymers, proteins, and linkers. Future work focusing on very controlled CNT interactions with biological materials, and understanding of possible variables in the system , such as the electrodes, bias, sensing construct, are essential before this sensor component would be applicable for point of care applications. The removable PDMS device and chuck allowed us to study and evaluate which variables were important in our setup in order to ensure the stability of such a sensitive system. These results guided us in the design of microfluidic devices for other collaborative projects.

# CHAPTER 10. OTHER MICROFLUIDIC SENSOR CONSTRUCTS

## 10.1 Removable Microfluidic Device for a Hypermethylated DNA Sensor

Brandon Heimer and the Professor Hadley Sikes group developed an inexpensive epigenotyping assay for hypermethylation of deoxyribonucleic acid (DNA) gene promoter regions. More specifically, the sensor focused on detection of enzymatic hypermethylated regions containing CpG islands, or regions with high numbers of cytosine followed by guanosine nucleotides on the same DNA stand.[153] These genetic regions are indicative of certain types of cancer, as well as patient responsiveness to specific chemotherapy approaches. This project focused on direct detection of methylated $O^6$-methylguanine DNA methyltransferase (MGMT) fragments, which indicate patient responsiveness to treatment of glioblastoma using alkylating agents.

### 10.1.1 Sensor Design

The standard approach for methylated DNA detection requires sodium bisulfite conversion of unmethylated DNA to urasil using a lengthy methylation-specific polymerase chain reaction (PCR) step, and can lead to error amplification due to any incomplete deamination leading to poor primer performance. There has been some progress in the avoidance of the sodium bisulfite conversion step through the use of a methyl binding domain (MBD) protein, but no affordable, clinically relevant approach has yet been developed.

The Sikes group developed a detection method of methylated DNA duplexes using the MBD protein, producing a direct streptavidin-Cy3 fluorescent or streptavidin-eosin photo-polymerization colorimetric readout. As depicted in Figure 10-1, a standard glass slide was spotted with reactive aldehyde groups (300 μm in diameter), and then was coated in a 0.2% agarose layer. Single-strand DNA containing unmethylated, single methylated, and double methylated CpG regions were coupled to the reaction regions on the glass slide using covalent bonding of the 5' hydrazyde groups to the aldehyde groups on the surface. Nonspecific binding was blocked using bovine serum albumin (BSA) in PBS. Then dilutions of target single-stranded DNA were added to the chip for bonding to the captured DNA (step 1). Afterwards, biotinylated MBD in binding buffer was added to the biochip and allowed to

bond (step 2). Depending on the detection method, either streptavidin-Cy3 or streptavidin-eosin was allowed to bind to the biotin present on the MBD protein (step 3). Direct readout of the fluorescent cyanine dye Cy3 was possible as seen in Figure 10-2 bottom left, or a polyethylene glycol (PEG) diacrylate monomer was added and photopolymerized with an eosin solution in oxygen under 522 nm light.[154] The full sensor procedure can be found in reference [153].

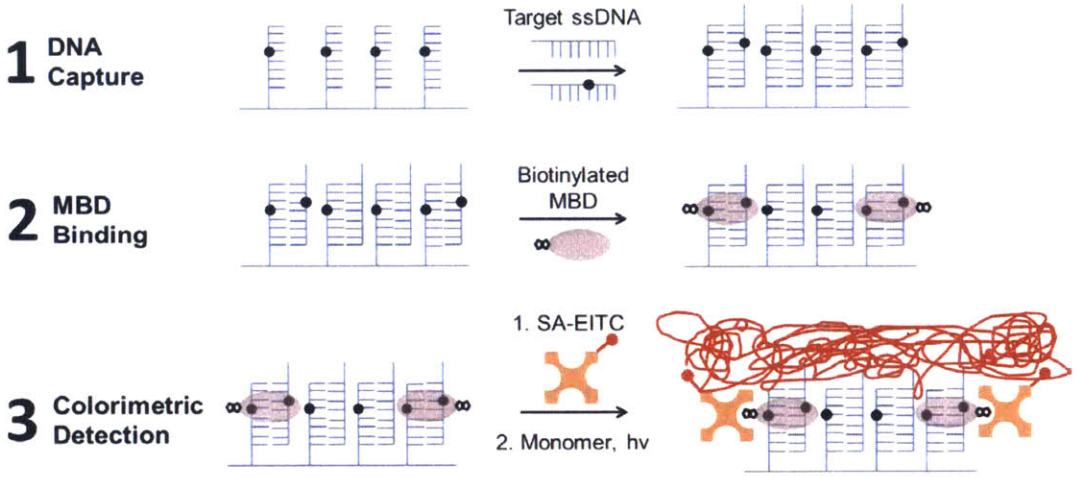


**Figure 10-1**[153] In brief, single stranded MGMT DNA fragments were reacted onto an agarose-coated glass slide. The black spots indicate the methylated CpG region. In step 1, target DNA was added to the surface and allowed to react to the surface-bound DNA. In step 2, MBD protein containing a biotin group was allowed to bond to the methylated region. In step 3, a fluorescent streptavidin (SA)-Cy3 protein was added, or a SA-eosin as well as a PEG diacrylate monomer was added and allowed to polymerize.

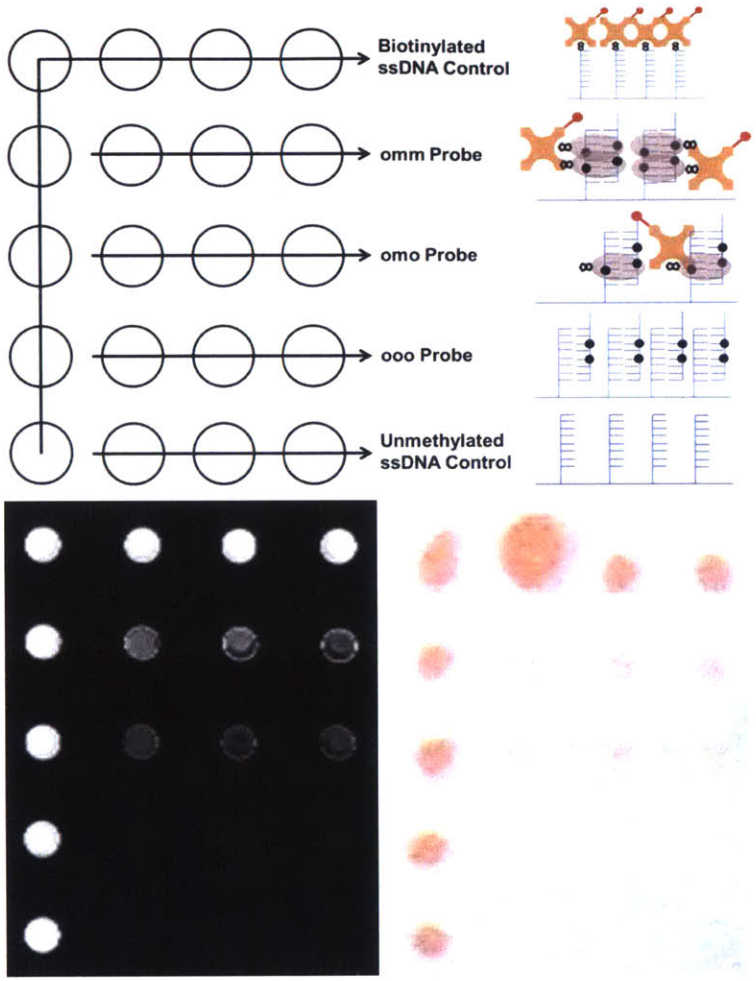


**Figure 10-2**[153] This figure depicts the reaction spot layout on the glass biochip. Ooo probes indicated unmethylated DNA strands, omo indicated single methylated CpG region, and omm indicates double methylated CpG region. Additional controls were also added. The bottom left shows a typical fluorescent readout, while the bottom right indicates a typical colorimetric readout.

The sensor's limit of detection was found to be 0.3 nM for double methylated CpG region, and 1 nM for single methylated CpG region. The detection was defined as 10 standard deviations above the unmethylated probe that is defined as the ooo probe in Figure 10-2. The detection signal vs. concentration of the target DNA that is bonded in (step 1 of Figure 10-1) is plotted in Figure 10-3.

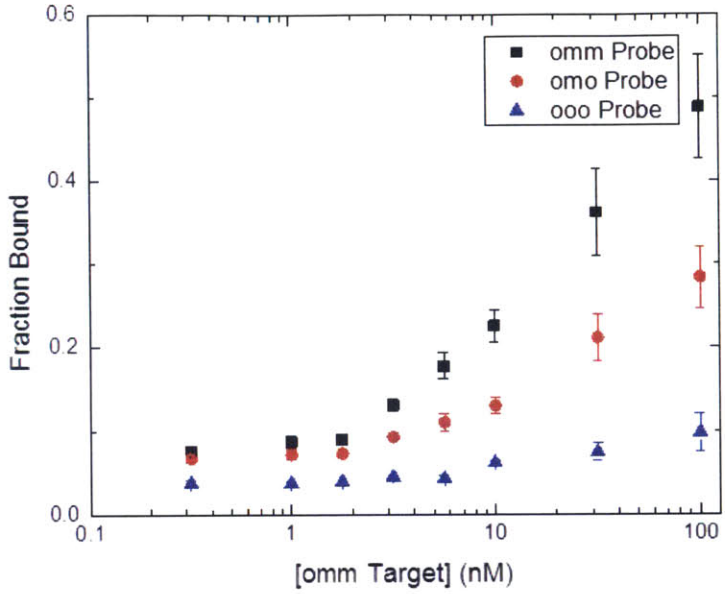


**Figure 10-3**[153] Fluorescent detection of the methylated CpG regions. The plot shows the MBD binding signal vs. the concentration of the target single stranded DNA that is bonded to the reaction regions.

### 10.1.2 Stationary and Microfluidic Approach

The direct fluorescent and colorimetric sensor was developed for both a stationary and a microfluidic flow system. The stationary reaction steps were done in a humidity box and the slide was simply rinsed between each binding step. In order to introduce the ability of multiplex sensing, as well as standardize and possibly limit biological solution volume, a recycle microfluidic system was set up for the sensor. This design featured a removable PDMS device that was reversibly bound to the glass slide containing reaction regions. (Figure 10-4) In order to ensure even flow across the entire reaction region, glass supports were included within the polymeric device as well as above the device so that the external binding pressure was even across the entire region. (Figure 10-5 and Figure 10-6) A peristaltic pump was connected to the inlet tubing and solution reservoir, while the outlet solution was similarly collected into another Eppendorf tube.[155] This allowed for backwards and forward flow and thus created essentially a recycled system.

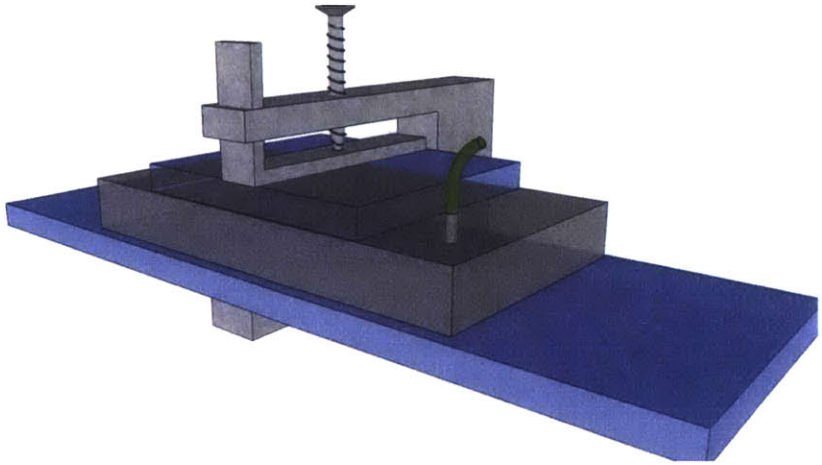

**Figure 10-4** Microfluidic device design depicted with a C-clamp, showing the overall footprint of the setup. Both C-clamps and binder clips were used for this device.

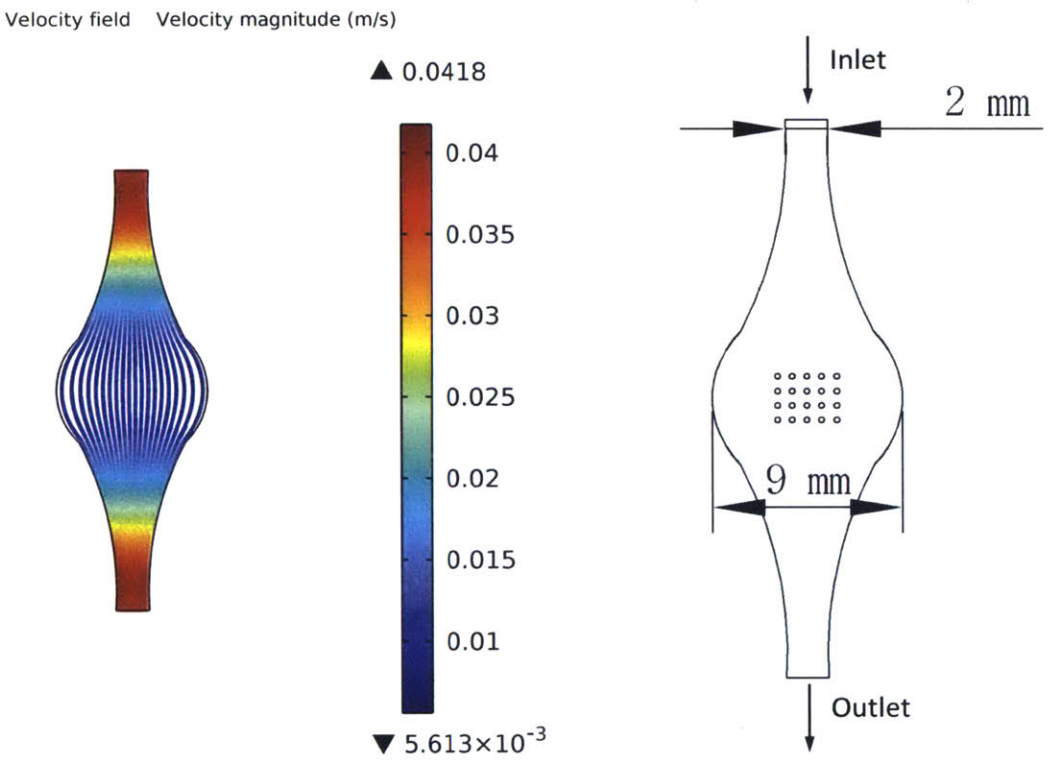


**Figure 10-5** COMSOL finite element simulation of the flow profile over the reaction spots.

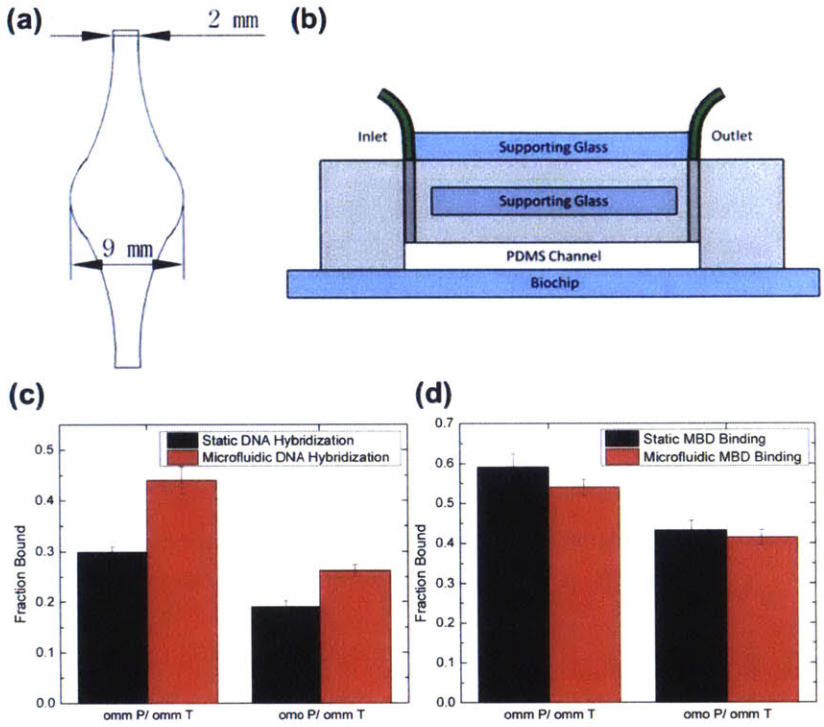


**Figure 10-6**[153] Microfluidic device design featuring two glass supports. The device was reversible clamped onto the biochip using standard binder clips. The glass support above the device ensured that the pressure was even across, and this was visually confirmed during experiments. Part (c) and (d) compare static vs. microfluidic signal for DNA and MBD binding, respectively.

By applying a microfluidic setup to the sensing system, we were able to limit some of the DNA diffusion limitations in a static system, as is depicted in Figure 10-6 (c) and as has been previously seen in the literature.[156, 157] The MBD binding, however, did not seem to improve with the addition of the flow system. This could be partially explained by the high concentration of the MBD protein in the binding solution as well as an excess of the reaction time, and then possibly a slight loss of this protein during the subsequent wash steps. Both static and flow system reactions were simulated for the MBD protein and were found to reach equilibrium, although the agarose layer and some of this gel layer binding effects had to be approximated for the numerical analysis. By systematically varying the reaction times and keeping them consistent for both the static and the flow systems, a further understanding could be acquired for this sensing construct. Overall, however, this new sensing construct was found to significantly improve the standard methylation detection method by minimizing the cost of the system as well as significantly decreasing the overall reaction time.

## 10.2 PDMS Wells and hPDMS Nanopores for Ion Sensing

In collaboration with Steven Shimizu in the Professor Michael Strano group, we applied photolithography and polymeric techniques to further progress the study of nanotube ion channels and to begin the development of microfluidic devices for single junction and double "Y" CNT junctions. The existing platform utilized chemical-vapor deposition (CVD) to grow ultra-long, aligned single-walled carbon nanotubes (SWCNTs). The diameter of the carbon nanotubes is measured through the radial breathing mode in Raman spectroscopy, to which it has an inversely proportional relationship. An epoxy barrier is then placed over the nanotubes to define two reservoirs, and the exposed nanotube regions are etched away using oxygen plasma. This leaves open nanotubes spanning the two reservoirs. The ends of the nanotubes contain carboxylic acids from the plasma etch and water exposure, and can be used as sites for further chemistry. The reservoirs are filled with an electrolyte solution, Ag/AgCl electrodes are inserted, and then the current is measured across the reservoirs, under a constant voltage. The Strano group proposed that the electric field drives the protons through the CNT-pores. This allows for the measurement of CNT-based pore blocking events, where protons can freely travel through the CNT-defined nanopore while cations would block the proton current and thus show a decrease in the measured value.[158, 159] This system has been applied to many model solutions, including KCl, NaCl, LiCl, CsCl, glycine, and β-alanine, but suffers from low percentage of CNT use with the current reservoir setup.

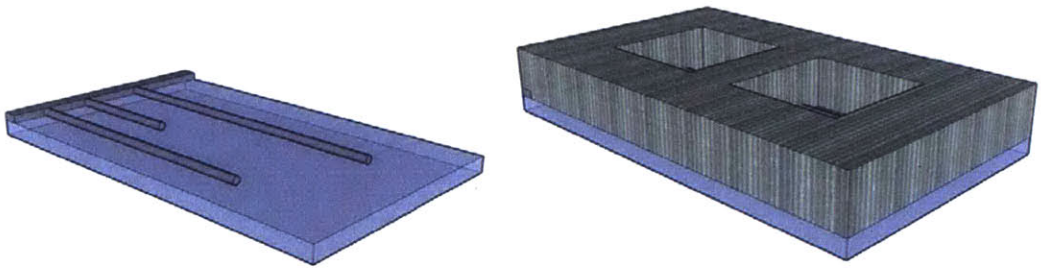

**Figure 10-7** Schematic of the CNT and PDMS well setup. On left, CNTs are depicted as long cylinders, CVD-grown along the surface. Then PDMS (grey, on right) is bonded on top of the surface, exposing the CNTs in the wells for further modification and sensing.

### 10.2.1 Dense PDMS-Well and hPDMS Nanopore Design

In order to increase the throughput of this setup, PDMS-based reservoirs were created with much smaller reservoir features. Initially, manual punching (Harris Uni-Core Punch) of thin PDMS sheets allowed for 350 μm in diameter wells that were about 1-2 mm apart. Eventually, using photolithography with an SU-8 mask defining the well-features, PDMS-based square wells with sides of 0.1-1 mm were developed. In order to ensure proper PDMS well formation, a large C-clamp or a piece of glass with a weight was added on top of the PDMS and mask, thus effectively pushing out any excess PDMS. (Figure 10-8 and Figure 10-9) Since oxygen plasma etches away CNTs, the designs were bonded to the silicon wafer containing CNTs using highly-crosslinked liquid PDMS glue, as explained in more detail in Section A.1.7.

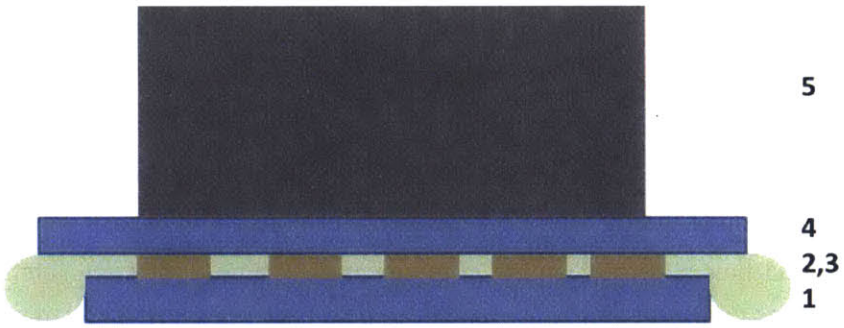


**Figure 10-8** Cross-sectional view of the PDMS-based wells. From the bottom, 1 is the silicon wafer containing SU-8 defined features (dark green, 2). A layer of PDMS is poured on top (light green, 3), and the excess is pushed out using a flat piece of glass (blue, 4) and a piece of weight on top (grey, 5). Alternatively, a c-clamp was also used with similar results.

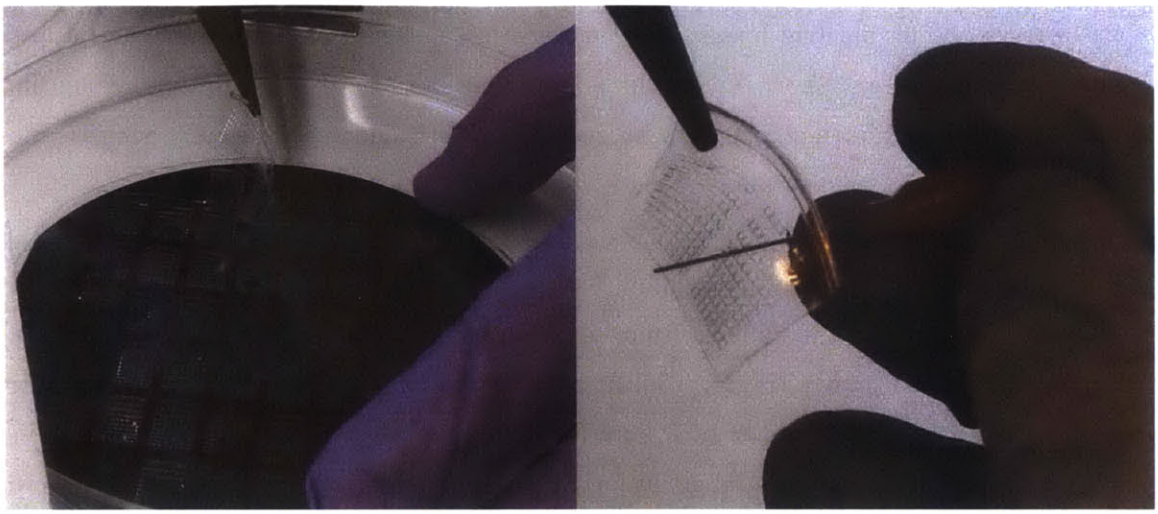

**Figure 10-9** Photograph of the silicon wafer with baked PDMS after deposition of weight on the top. The stub adapter shows that fully developed PDMS wells were produced at different distances apart.

The key component in this design is to ensure that the polymeric platform properly conforms around the CNT to guarantee no leaking or disturbance of the ion channel (Figure 10-10). Through the use of AFM, however, we have observed that PDMS was limited to replicating only 10s of nanometers, and was not the material appropriate for this application.

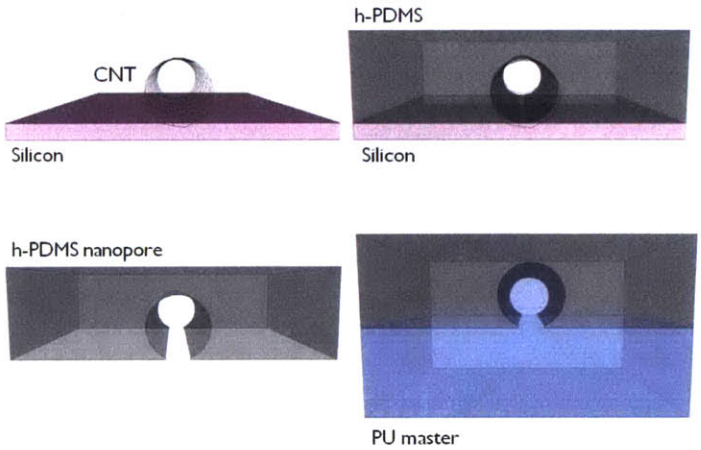


**Figure 10-10** Polymeric platform for CNT-based ion channel. CNTs are grown on the silicon using CVD. Liquid h-PDMS then conforms around the CNT and is hardened through baking. The stamping of the CNT onto the h-PDMS is further confirmed through the use of AFM on (PU).

In order to replicate smaller features on the nm scale, we replaced the PDMS-based polymeric construct with a more crosslinked hard-PDMS (h-PDMS) polymer. This polymer

has a much shorter bonding length of 0.2 nm and has shown to replicate features of a few nanometers in size and show limited shrinking during baking.[160-163] By optimizing the silanization of the silicon chip and the procedure, we were able to significantly decrease the roughness of the polymer surface and to improve feature size.

To further advance the study and allow for more consistent AFM tracking of the small features, we added an additional step of replicating a positive CNT feature onto a polyurethane (PU) master (Figure 10-10). PU is a much harder material and has shown improvements in AFM readouts of features, although further comparison of features on h-PDMS and PU is ongoing. By aligning the SEM image of silicon and the CNTs, we were able to isolate CNT replicates in the PU mold (Figure 10-11). Thus, although further improvements in the procedure and decrease in roughness are necessary, we have already shown two degrees of replication with the current setup.

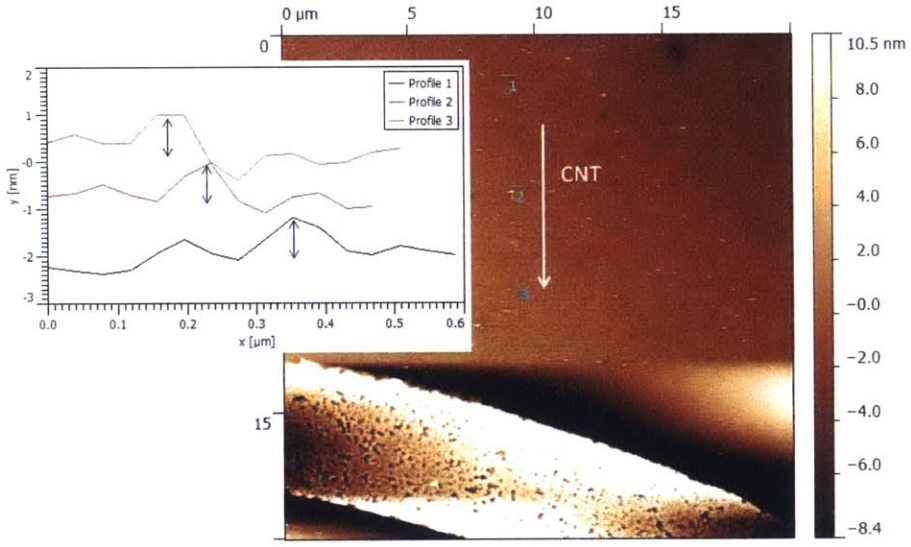


**Figure 10-11** AFM scan of a PU region near a specific marker. CNTs were identified by alignment with an SEM image of the silicon wafer in that same region prior to the polymeric replication. The height profiles further confirm replication of a CNT on the order of 1 nm in diameter.

Currently, the above mentioned setup produces about 60 CNT-based nanopores on each silicon wafer and allows the study of multiple PDMS-well experiments for each CVD-grown CNT. Future work will focus on applying this new polymeric system to the CNT ion channels, in order to increase the number of possible junctions studied on each chip. Further

studies of h-PDMS conformation need to be performed to eradicate any possible ion leaks. Also a constant use of rigorous controls would be needed to ensure the system is robust.

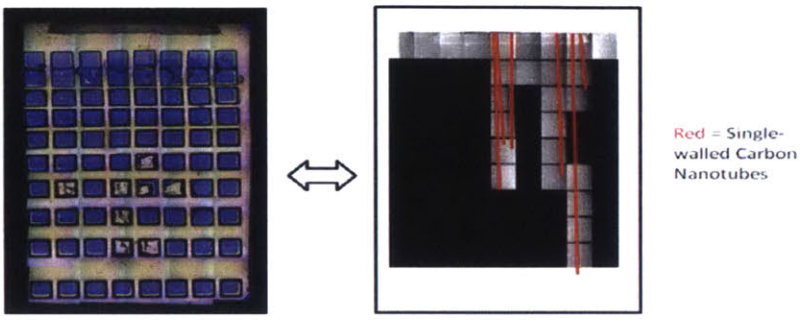


**Figure 10-12** Photograph of PDMS wells design defined by the SU-8 wafer. Clear blue rectangle means a well was cleanly-formed using PDMS. Distance between PDMS wells varies from 0.1-1 mm from top to bottom of photograph. On the right is an SEM image with CNTs marked with red. The PDMS wells will be attached on top of the silicon wafer containing these CVD-grown CNTs using PDMS glue.

### 10.2.2 Raman-Based CNT Solution Filling Study Setup

Similarly, Steven Shimizu, in Professor Michael Strano group, is developing a Raman-based measurement of CNT filling with solution, as an alternative and supplementary method to pore blocking. In this setup, the vibrational modes are shown to shift and change in intensity when a fluid enters the CNT. This allows a better understanding of the internal interactions and would further confirm that the CNT studied was properly etched on both edges. In this scenario, two PDMS-defined channels were bonded to the silicon surface, while the CNT spanned across the two devices, perpendicular to the flow channels. Therefore the CNT is exposed to open air, thus ensuring that it is indeed the CNT that is being filled and not a nearby leak. This also opens the CNT to Raman measurements. These measurements were not always consistent, thus further theoretical studies are currently being pursued before the behavior could be fully understood. The setup and an example of an occasional shift peak are presented in Figure 10-13.

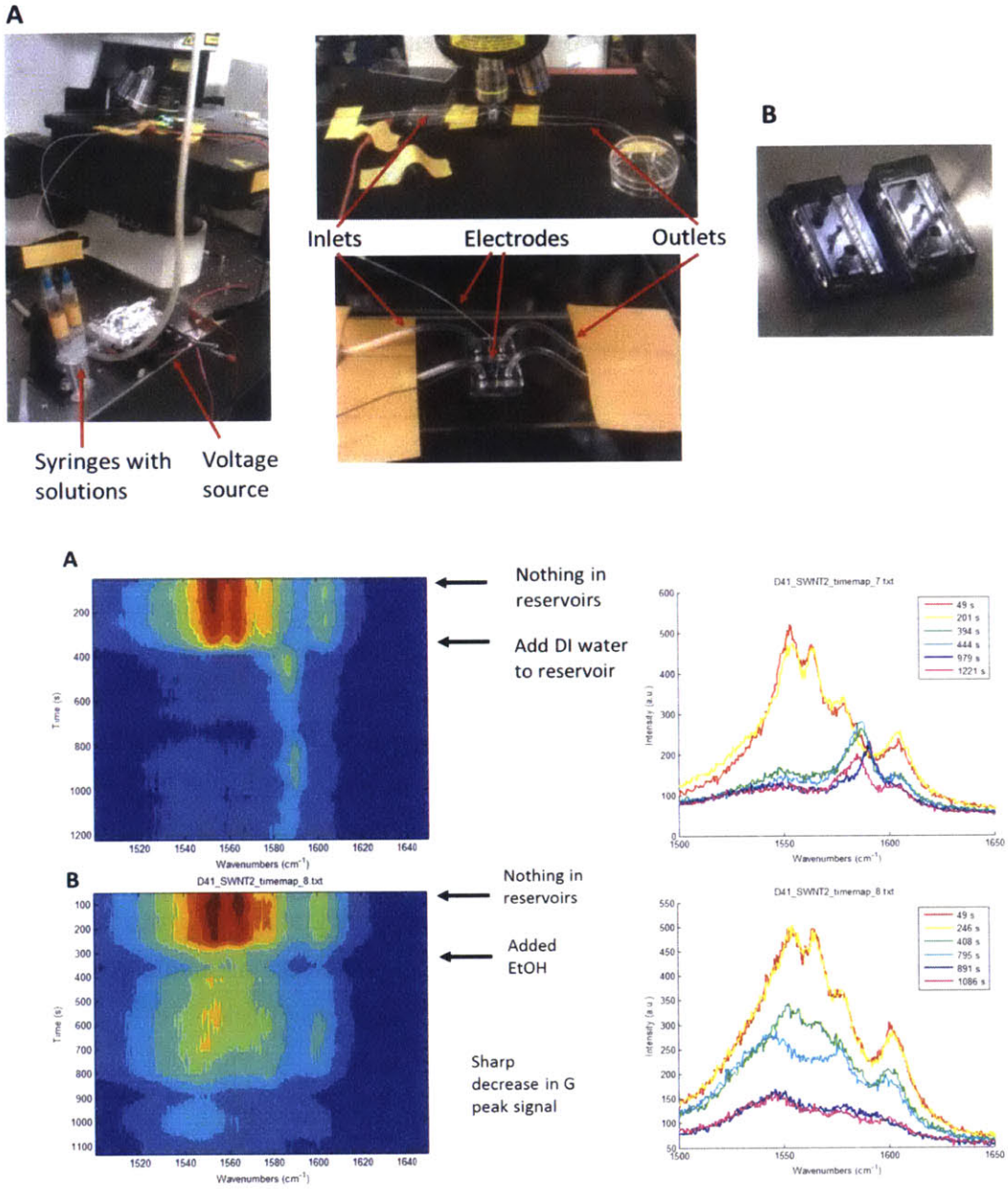


**Figure 10-13** Photograph of PDMS device design, with two channels flowing with solution, while the CNT is exposed to the air in between the devices. The bottom half of figure shows an example of the Raman absorbance measurement change over time for water and ethanol. Although this response needs to be further validated and theoretical work is ongoing to further understand the molecular interaction inside the CNT.

## 10.3 Abrasion-based Fabrication of Carbon Nanotube Surface Sensors, in Collaboration with the Swager Group

The Swager lab has developed a CNT deposition method through mechanical abrasion onto a paper surface.[103] SWCNTs are compressed into a pellet and are then mechanically deposited onto the paper surface with gold electrodes. This leads to a simple and solvent-free approach to fabricating resistance-based gas sensors. This abrasion method was further studied as a possible application to fabricating a liquid biomolecular sensor.

Although wax paper holds up well for gas sensing, it begins to soak up water and leak through within minutes for a liquid flow sensor. In order to improve water resistance, a layer of wax was added on top of the paper construct, as seen in Figure 10-14. The same flow setup, as described in CHAPTER 9, was used to define the PDMS-based microfluidic channel, which allows for solution flow at a rate of 20-50 μL/min above the paper sensor.

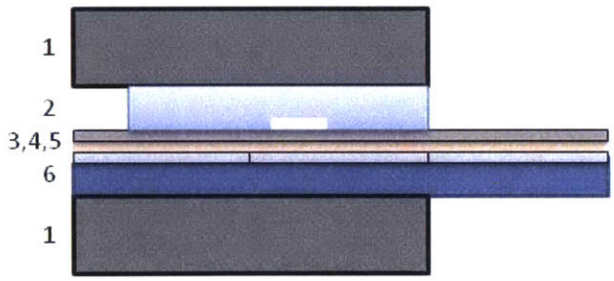


**Figure 10-14** Paper-based microfluidic device construct schematic, from the side. Each layer is numbered as follows: 1 is the aluminum chuck as described previously, 2 is the PDMS device defining the microfluidic channel which is attached above the deposited CNTs, 3 (top layer) is the melted wax, 4 (middle layer) is the wax paper, 5 (bottom layer) is the double sided tape, and 6 is the glass slide support.

In order to ensure a proper seal between the PDMS channel and the paper device, the deposited wax layer had to be even, without bumps, but thick enough to resist water leaks. This was accomplished through the use of wax paraffin pastilles, which were heated and then spread out using a light pressure from a razor blade. The electrodes were then thermally evaporated onto the paper device and then the CNTs were deposited using mechanical abrasion as described by the DRAFT technique in [103]. The wax provided sufficient friction for proper deposition. This wax paper device was then attached to a glass support using

double sided tape, and inserted into the aluminum chuck as described in Figure 9-1. This construct proved resistant to water for up to 80 minutes. This water-resistance time could be extended with increased wax thickness. Signal stability and selectivity of the CNT response is a future focus for this sensing method.

## CHAPTER 11. SUMMARY AND FUTURE DIRECTIONS

This thesis work presents a portable, hand-driven blood plasma separation construct that could replace centrifugation for point of care applications, where large equipment or proper user training is very limited. This device provides plasma separation orders of magnitude better than the literature, while at the same time shows minimal clogging or fouling of the microfluidic device. This separation system was applied to a portable, low power malaria protein sensor that produced an amplified color change in the presence of the malaria protein at a concentration of 7.5 nM and above for undiluted whole blood.

This work also presents great separation progress for undiluted blood and could be incorporated with standard laboratory sensors, such as bench-top ELISAs, since the plasma can be collected within a few minutes for diluted blood and within around 10-20 minutes for undiluted blood (assuming around 100 μL of plasma is needed for ELISA), although further improvements in stability for the undiluted blood separation would be important. Possible future improvements for undiluted blood separation could include incorporation of on-chip bubble traps[164], or partial blood degassing before loading. Although the blood-buffer Y-inlet system presents a robust setup, some plasma and buffer dye diffusion occurs during the experimental run, and part of the sample is not collected due to this diffusion. Eliminating the buffer with the dye could simplify the overall system. Further modification of the channel surface or possibly switching to a new material could also be advantageous for data reproducibility.

This expansion design could be an additional resource for cell free approximation in numerical analysis, as high detail numerical analysis and cell free layer prediction becomes a more feasible option in the coming years. Additives such as dextran or other cell-interaction and viscosity disrupting components could be of value in these expansion studies in order to isolate how different components contribute to the cell free layer formation. Also, incorporation of more plasma skimming channels could be of interest, as it could possibly show by how much the plasma purity decreases as each cell free layer section is skimmed off. This could be interesting for optimization of yield vs. isolate cell ratio. The numerical analysis and optimization of yield could also be beneficial for increasing throughput while keeping the same system stability.

Full incorporation of the colorimetric sensor onto the plasma separation device could also be of value, although presents new challenges in color readout and the ability of camera phone data collection. One possibility would be to have an open-air well with pre-functionalized antibody surface that would be connected to multiple microfluidic channels containing plasma with the protein, as well as the materials needed for the polymer amplification sensor. Other sensing constructs mentioned in CHAPTER 9 and CHAPTER 10 could possibly be incorporated with the portable blood plasma processing chip in order to expand the application of these sensors to the clinical field, although future improvements in CNT sensor stability and the ability to handle a complex plasma fluid would first be required.

# APPENDIX. A METHODS

## A.1 Device Fabrication and PDMS-Related Methods

### A.1.1 PDMS Devices Using Photolithography

Photolithography allows the fabrication of reusable masks that would support many generations of PDMS devices, thus lowering the overall cost of these polymer-based microfluidic devices.[165] Given that the featured heights were on the order of 100-180 μm, SU-8 2050 was used for all of the fabrication.[166] This negative photoresist is provided by the Microsystem Technologies Laboratories (MTL) at MIT.

1. Dehydrate new silicon wafers at 120 °C for at least 30 minutes, longer if a more humid day. Especially important to increase the length of time of dehydration if the aspect ratio is high (around 10).
2. Cover the SU-8 spinner in foil for future clean up. Wipe any old SU-8 off with propylene glycol monomethyl ether acetate (PM acetate). Using a dummy wafer, set the appropriate speed for steps 1 and 2, depending on the desired height of channels.[166]
3. Remove wafers from hot plate, one at a time, spray down with air to remove any particles and put on the SU-8 spinner. Pour around 4 mL of SU-8 at the center of the wafer (about 1 mL of SU-8 per inch of wafer) and spin.[166]
4. Once stopped, cover Q-tip with PM Acetate and wipe below and at edge of wafer to clean up. Could also wipe with Q-tip at the end of the spin cycle.
5. Move wafer to the hot plate for soft bake: 7 minutes at 65 °C and 30 minutes at 95 °C, depending on the resist and features.[166] For high aspect ratio designs, ramp up the temperature slowly. Clean up SU-8 spinner.
6. Let wafers cool; for high aspect ratio, let cool for longer. Cooling time can be optimized by cooling to room temperature and then putting back on the hot plate – if any wrinkling occurs, bake for longer.
7. Once wafers cool, attach transparency masks on top of SU-8 wafer using pieces of tape at edges. Expose the SU-8 and mask to UV light for an appropriate amount of power.[166] MTL features Electronic Visions Model EV620 Mask Aligner, which produces 10 $mW/cm^2/sec$ at 365-405 nm wavelengths.[167, 168] Addition of cooling intervals allows for more exact features.

8. Post bake the wafers: 5 minutes at 65 °C and 15 minutes at 95 °C, depending on the resist and features.[166] For high aspect ratio designs, ramp up the temperature slowly.
9. Develop wafers by agitating the masks in PM Acetate for about 5 minutes. Masks will be developed when spraying features with isopropyl alcohol does not form a white film.
10. Check feature height if desired, under microscope.
11. To minimize PDMS-adhesion to the SU-8 mask, evaporate a few droplets of 3-mercaptopropyltrimethoxysilane on the mask housed in a covered container. This could be done for 24 hours in a chemical hood, or for a few hours in a vacuum chamber.

### A.1.2 PDMS Devices Using Tape-Based Masks

For features on the millimeter scale, scotch tape-based masks can be made to define PDMS devices.[169]

1. Attach tape to a clean silicon wafer or glass slide, depending on device design size. It helps to use another small glass slide to slide down the tape as you attach it, in order to minimize bubbles.
2. 3M 810 Scotch tape is 62.5 μm thick. If a channel with a larger height is preferred, 2 or 3 layers can be attached. (Other tape brands or types can be used for slightly different thickness values).
3. Draw the preferred design on the tape. Or if available, use a printed mask or a solid mask to help define the design.
4. Cut the design using a microscope glass slide as the guide for straight lines. Make sure to cut through corners, and go over the line multiple times whenever using multiple layers of tape.
5. Peel off the rest of the tape and bake at 60-70 °C for 3-5 minutes in order to increase the adhesive strength. Without pre-baking, a new mask will most likely need to be defined after every PDMS device.

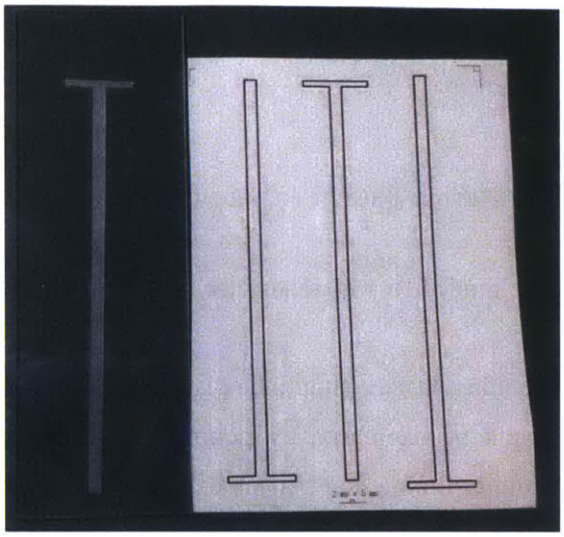

**Figure A-1** Photograph of a T-based design defined with scotch tape master.

### A.1.3 Making PDMS Devices from a Mask

1. PDMS is fabricated using Sylgard 184, according to manufacturer's instructions.[168] Briefly, the elastomer and curing agent are mixed 10:1, respectively, by weight. If less flexible PDMS is preferred, the elastomer to curing agent ratio can be increased to 5:1 or 3:1.
2. Degas PDMS in a vacuum chamber, ensuring no spillover, pour on mask and bake. Generally baking for 2 hours at 60-70 °C is sufficient. For more crosslinked, less flexible, PDMS – bake at a higher temperature (80 °C+). Do not use a plastic petri dish to house mask and PDMS above 70 °C.
3. Let PDMS cool and cut out the design. To help release the PDMS from the mask surface, 70% ethanol in water could be sprayed along the cut edges.

### A.1.4 PDMS Support for Long or Wide Channels

If the channel is more than 2 mm longer or wide, the channel is likely to sag or expand dramatically under pressure, depending on the pressure input. In order to minimize channel feature variation, a channel support using a glass slide is inserted. Briefly, bake a thin layer of PDMS on top of the mask for about 10-15 minutes such that the PDMS is sticky but mostly solid. Position a piece of microscope glass, cut down to size, above the desired features. Pour

the rest of the PDMS on top of the mask and bake for 2 hours; double check that the glass is properly aligned once in the oven.

### A.1.5 Plasma-Based Permanent PDMS Bonding

PDMS can be permanently bonded to a glass surface or itself, but oxidation through oxygen or air plasma.

1. PDMS and glass bonding surface should be placed in plasma etcher, facing up.
2. Oxygen levels should be decreased by pumping down the plasma etcher using a vacuum pump. Vacuum timing and plasma exposure timing should be optimized for each surface and system, such as to ensure sufficient oxygen species are present to optimal plasma production and timing should be sufficient for full surface activation. For our system, timing was about 30 seconds of vacuum pumping, followed by 30 seconds of plasma exposure. Plasma, consisting of reactive oxygen species, attacks the methyl groups and replaces them with hydroxyl groups, forming silanol groups on the surface. This surface can form covalent bonds with other activated surfaces containing silanol groups, thus creating a permanent bond.[170] The silanol groups render the surface hydrophilic. This feature, however, only lasts for about an hour, before PDMS recovers its hydrophobic nature.
3. To ensure a strong bond and possibly improve covalent bond formation, newly bonded devices could be baked at 60-70 °C for 2-8 hours. Allowing the devices to rest for about 24 hours after bonding has also shown improvement in bond strength.

### A.1.6 Corona-Based Bonding

A hand-held corona (Electro-Technic Products, BD-10AS) discharge unit was used for PDMS-PDMS bonding, based on the procedure defined in reference [170]. Briefly, both PDMS pieces were positioned facing up. The corona unit was plugged in and very slowly moved over the PDMS piece (around 30 seconds for 1 $cm^2$ of PDMS). The two surfaces were quickly attached together and allowed to bond for at least one hour.

### A.1.7 PDMS "Glue" for Permanent Bonding

PDMS "glue" can be formed by mixing a high ratio of elastomer to curing agent (about 3:1). This allows for quick crosslinking when heated and better control of feature size.[160] The PDMS was degassed for a shorter period of time, around 10 minutes before use. By hand, we were able to glue PDMS layers featuring sizes down to around 750 μm with minimal PDMS bleeding (on the order of 100-200 μm). In order to minimize this bleeding and create an even thin layer, PDMS glue was spin coated on a clean glass slide at 3000 rpm for 45 seconds. After which, the PDMS layer with our device features that we want to bond was deposited on the glass slide, lifted off and placed (now with glue) onto the silicon substrate that contains CNTs. The glue was then cured at 65 °C for 2-3 hours.

### A.1.8 Temporary PDMS Bonding – design and materials

For certain applications, such as for CNT sensing, permanently attaching PDMS to a surface is not preferable. Therefore, temporary attachment methods are preferable. For initial testing of designs, temporary attachment could be achieved with a glass slide and binder clips of appropriate size. Glass should be attached on top of PDMS in order to diffuse the pressure from the binder clips and prevent any channel sagging. Glass slides can be cut to use using a diamond cutter, as described in Section A.1.4. For a cross-section view of the temporary attachment, see Figure 10-4.

### A.1.9 hPDMS Tips and Tricks

hPDMS is a more crosslinked, harder PDMS-based material alternative that was used for small-feature replication.

1. Weigh out 3.4 g of 7-8% vinylmethylsiloxane-dimethylsiloxane copolymer (for 1 $cm^2$ cover).[160-162]
2. Add 2 drops of 1,3,5,7-tetramethylcyclotetrasiloxane. Add 1 drop of platinum divinyltetramethyldisiloxane. Use wooden stick to mix together in a small petri dish (55 mm in diameter).[163]
3. Place petri dish in dessicator connected to a vacuum line, turn on vacuum for 5 minutes to remove bubbles.

4. Add 1 g of (25–30% methylhydrosiloxane)–(dimethylsiloxane). Add quickly, stir with the same stick. This mixture will solidify within 5 minutes, so no time to put under vacuum, the bubbles will be removed during the spin-coating procedure.
5. Load master onto spin-coater (silicon with carbon nanotubes), add h-PDMS small amount in center. Spin coat at 500 r.p.m. for 5 seconds, then 1000 r.p.m. for 40 s. Creates a h-PDMS layer on the order of 1 μm.
6. Bake in oven at 60°C for 10 min.
7. Add Sylgard PDMS (10:1, procedure described in Section A.1.3) on top, bake at 70°C for 6 hours. The softer PDMS minimize cracks during lift and creates a more malleable piece.

## A.2 Microfluidic Device Setup for Blood Separation

### A.2.1 Tubing Y-split Setup for Blood Separation

The full setup is pictured in Figure 3-2. Fluorinated ethylene propylene (FEP) tubing with 0.02" inner diameter (ID) and 1/16" outer diameter (OD) was used for all of the connections and most outlet tubing. The on-off valves were purchased from Idex P-732 (UpChurch), and the Y-splitter was Idex P-512 (UpChurch), both for 1/16" OD tubing. The blood tubing was minimized for the blood region to be minimal while still fitting the tubings – lengths from 1.5"-4" depending on convenience. Majority of the outlet tubing was 4-6", depending on the height resistance to be added. The outlet tubing was taped down onto a glass slide for proper height control and 1.5 mL Eppendorf tubes were placed below the tubing exit. Inner volume of the device is less than 1 μL, and tubing inner diameter varied from 30-100 μL, depending on whether the lengths were minimized.

### A.2.2 Blood Handling and Storage

Blood is ordered undiluted in a Becton Dickinson 10 mL vacutainer collection tube with spray coated K2-EDTA coating. The blood is shipped same day, with an ice pack not directly touching the sample. Blood is stored in the same vacutainer tube, in refrigerator. The blood can be stored for about a week, although the chance of clotting increases after about 5 days.

The aging of blood was less of an issue for diluted blood experiments, but caused significant clotting after 3-5 days for undiluted blood.

To mix the cells, the tube is inverted 5-10 times, and for small volumes, a gentle vortex can be applied (4-6 out of 10 maximum setting). It is best to use a fluorescent lamp, as halogen lamp can heat up the sample or device cause clotting (blood can turn solid!). It is best to minimize blood contact with metal or long-term glass surface storage.

### A.2.3 Blood Separation Procedure

1. Blood is diluted using phosphate buffered saline (PBS) in a 20 mL glass vial. Or blood is simply poured into the vial if using undiluted blood.
2. A Beckton Dickinson (BD) Luer-lock Syringe is loaded with the blood, while minimizing bubbles. If bubbles are trapped near the bottom of the syringe, do not fully fill the syringe. Stop filling halfway and then take in air, allow the large amount of air to combine with the trapped bubble, by tapping if necessary, and then releasing the extra air before loading the full syringe.
3. Syringe is attached to the luer-tubing fitting as described in Section A.2.1.
4. The syringe is either loaded into a syringe pump (set with the correct diameter for the syringe used) or is pushed by hand. For the pump, flow rate is set between 30-250 μL/min and a small amount of blood is loaded just past the Y junction. This gets rid of the entrance bubble. Then blood flow is stopped (or stopped by hand). Then the on-off valve is closed for the blood channel and opened for the buffer channel containing 1-10% glycerol in PBS, and a green dye. This buffer is loaded onto the device, washing out any trapped bubbles. The buffer channel is closed off with the on-off valve and the blood channel is reopened and restarted.
5. The blood plasma is collected once it is visually clear that the "yellow" or "clear" plasma region is at the outlet (after the dye/buffer exits). The plasma is collected into an Eppendorf tube. Both plasma and outlet tubes are weighed to calculate the yield.

### A.2.4 Blood Cell Counting – Hemocytometer

If there are red blood cells in the blood plasma, solution should be diluted to a barely-pink color. Undiluted blood has to be diluted 1000 times to count. If it's undiluted blood plasma, it helps to do a two times dilution in order to be able to count despite the large number of small platelets. To count cells, load 10 μL of solution onto a hemocytometer. Load the hemocytometer onto the microscope and count the appropriate number of squares to get around 50 cells if possible. The solution depth is 0.1 mm and therefore the volume counted can be calculated from the number of squares counted. The square areas are defined on the hemocytometer. If low cell count, counting two solution sets on each side of the hemocytometer is helpful.

### A.2.5 Blood Plasma Volume Approximation

To approximate blood plasma volume, blood was mixed and loaded into a glass capillary tube (Thomas Scientific), which was sealed using putty capillary tubes sealant (Critoseal). The capillary tubes were inserted into 15 mL falcon tube covered with styrofome pieces for cushion. The tubes were inserted into a large centrifuge and spun down at 3000 rpm for 10 minutes two times. Measure the total height and the plasma height both times to make sure the plasma volume is extracted properly. This is an approximation as little bits of plasma get trapped between the cells. It is a balance of centrifuging intensity and making sure the clay does not begin to melt due to the heat in the centrifuge.

## A.3 Sensing Procedures

### A.3.1 CNT-deposition assembly

The glass slide sensor consists of electrodes made using a metal evaporator, which deposited 10 nm layer of chromium and 75 nm gold. The CNTs were suspended usually in ethanol (except when surfactants were added at which point other solvents could be used), and were sonicated for 2 minutes with in the water bath. Then 1 μL droplets were deposited between electrodes and were evaporated under vacuum for a few minutes. Resistances were measured and droplets were added until all of the channels had around 100 kΩ of resistance. Ensuring

the resistances were comparable significantly limited the noise. The sensor was plugged into an edge connector (Digikey 1-5530843-8-ND) and into a breadboard connected to a potentiostat and computer. The bias was usually set at 0.1V, and the current was read out as solution was pulled into the device. The Y-tubing setup is very similar to the setup for blood separation, described in Section A.2.1. The solution was pulled at a flow rate of around 20-50 μL/min (100 μL/min led to CNT loss). The data were exported using a .txt file and was manipulated in Matlab, with sample code included at the end of this chapter.

### A.3.2 Fluorescence and Colorimetric ELISA CRP Sensing

The fluorescence measurements featured glutaraldehyde surface coverage process and protein A – antibody binding for the initial surface coverage. References [2, 171, 172] describe the full procedures used for this method. The fluorescein isothiocyanate (FITC) – antibody marker is the fluorescent component that leads to readout. This surface-readout method did not lead to detectable camera phone readout.

The HRP-based Colorimetric Sensing system is based on 96-well plate study, which was initially replicated from references [76, 77]. A few PDMS-based surfaces were also studied by incorporating the procedure defined in the references above for surface coverage and binding, using the antibody-protein-antibody procedure.

### A.3.3 Colorimetric Detection System

The colorimetric detection procedure is detailed in reference [75]. Briefly, the group saturates the chromatography paper with aldehyde groups. The paper is then taped to normal printer paper for support, and is covered with a wax layer on top (Xerox Color Cube printer that uses solid ink), leaving 3 mm diameter circular reaction regions. The reaction regions are then spotted with the antibody of interest, and are then exposed to either the protein of interest (at a number of concentrations) or to a control sample with no protein, and then to a reporter antibody with a covalent eosin tag. The eosin tag allows for fluorescence measurement using a microscope setup, with ImageJ being used for quantification of fluorescence. This fluorescence is a measurement of the protein presence using a typical "sandwich ELISA"

method. These background fluorescence measurements are then used to define the timing of the polymerization method, in order to ensure no background polymer signal.

For colorimetric detection, an aqueous amplification solution with a pH of 7.9 was used containing poly(ethylene glycol) diacrylate (PEGDA), triethanolamine (TEA), 1-vinyl-2-pyrrolidine (VP), phenolphthalein, and free eosin. The eosin that is free and is attached to the reporter antibody, as well as the tertiary amine (TEA) are the photoinitiator system for the PEGDA-VP polymer that can overcome oxygen inhibition and produce a colored polymer (with phenolphthalein) in under 100 seconds using LED light centered at the $\lambda$=522 nm, with 30 mW/cm$^2$. The polymerization time is adjusted so that the readout controls were colorless. The pH was adjusted to be below 8 using hydrochloric acid to ensure that the phenolphthalein was colorless initially and eosin was the dominant photoinitiator absorbing light. After polymerization and wash steps, NaOH was added to raise the pH of the solution, and the results were imaged either by eye or using a cell phone camera. The image analysis is done using ImageJ, by subtracting the blue channel intensity from the green channel intensity.[75]

For the plasma separation, up to four 5° expansion devices were run in parallel on a syringe pump, with flow rates ranging from 50-100 μL/min. The solution was loaded using a 3mL syringe (since the 1mL syringe does not have a luer-lock). Each plasma collected fraction is combined for the total plasma volume.

For protein spiking, the plasma volume was approximated using the glass capillary and centrifuge method described above. Then the protein standard was diluted using plasma collected in the separation device and added in the appropriate amounts based on the plasma volume in the total blood sample. The space taken up by cells was not counted for protein spiking. A concentration of 5-130 nM was used with 10 samples spaced out evenly on the logarithmic scale (logspace in Matlab). Around 30 μL of plasma sample was collected for each concentration and used for the 3 replicated in the colorimetric sensor.

### A.3.4 Paper and Wax Microfluidics

Weighing paper put on a glass slide and attached to PDMS channel leaks within 5minutes. In order to make paper more hydrophobic, we found that melting wax (parrafin wax beads are

the best, but wax sticks work as well) at 80 °C is ideal. Once melted, take a clean weighing paper and rub the wax all over the sheets. If too much wax is present, take a razor edge blade or better yet, microscope glass slide, and scrape off the extra wax from the paper. 80 °C is ideal because if it cools a little, it gets hardened on the glass quickly, for easier removal. Procedure was based on references [173, 174].

Ideally you want to see a clear layer of glass, no white regions, or else it's too bumpy to allow for flow if solution is being pulled. Pushing flow is easier and can handle more rough surfaces. The paper-based device was taped down on a glass slide using double-sided tape (centering the tape on the channel region to minimize leaking). Using this set up, 80 minutes of flow without any detectable leaks was possible, although the glass slide below was wet along the channel region. The CNTs that were drawn on the waxed paper stayed and looked the same for 80 minutes at 50 µl/min. This method was then applied to mechanical drawing of CNTs described in reference .[102, 103]

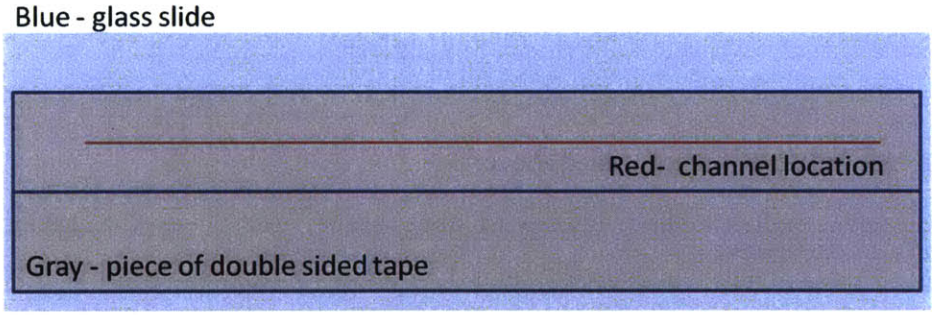


**Figure A-2** Wax paper-based sensor schematic of the layout. Two pieces of double sided tape are placed between the glass slide and weighing paper containing melted max that saturated the paper. The channel is centered with the tape to ensure it does not encounter any edges and to minimize sources of leaks.

## A.4 Sample Matlab Codes

Comsol-MATLAB LiveLink sample code used to modify Comsol and run multiple parameters/models/designs:

```
% Uploading Comsol model and defining file paths
model=mphload('ComsolModelFileName');
filepath='C:\Users\FilePathForComsolFile';
importpath='C:\Users\ImportPathForAutoCADDesignFile';
```

```
% varied parameters
bounds=[10 2 7]; % "inlet, plasma, outlet" boundary #s based on how Comsol
numbers them
outp=[0 147 294 441 588 735 882 1029 1176]; % outlet pressure parametric
sweep
uini=0.5555555555555555555; % inlet flow rate [m/s], average for 100 uL/min
flowrate=[uini uini/2 uini/3 uini/4 uini/5 uini/6 uini/7 uini/8 uini/9
uini/10]; % range of inlet flow rates

% number of refinements for different regions
refs(1)=1; % full refinement
refs(2)=1; % expansion refinement
refs(3)=1; % plasma refinement
% % % % % % % % % % do not change above, constant % % % % % % % % % %

display('Now calculating Design#')
tic

importfile='AutoCADDesign.dxf'; % autoCAD file design
filetxt='DesignResults.txt'; % export file name for results

fullimport=fullfile(importpath, importfile);
ModelParams(model, filepath, fullimport, refs, outp, filetxt, bounds,
flowrate);

toc % prints which model it is calculating and calculates how long the
model run takes
```

**Function "ModelParams" that is called above:**

```
function ModelParams(model, filepath, importpath, refs, outp, filetxt,
boundaries, flowrate)
% changing parameters in a comsol model

format longEng

filename=fullfile(filepath, filetxt);

fid=fopen(filename,'wt');
fprintf(fid,'*** run parametric study ***\n');
fprintf(fid,'Outlet Pressure [Pa] | Inlet [m^2/s] | Plasma [m^2/s] | Outlet
[m^2/s]\n');

model.hist.disable; % to save memory
model.geom('geom1').feature('imp1').set('filename', importpath); %set which
design using

for j=1:length(flowrate) % try out all the inlet velocities

    model.physics('spf').feature('inl1').set('U0in', flowrate(j));
    fprintf(fid,['Flow Rate is (m/s): ', num2str(flowrate(j)),' \n ']);%
open text file

    for i=1:length(outp) % try out all the output pressure values
```

```
        model.param.set('outp', outp(i));

        fprintf(fid,[num2str(outp(i)),' | ']);% open text file

        % define # of refinements
        model.mesh('mesh1').feature('ref1').set('numrefine',
{num2str(refs(1))});
        model.mesh('mesh1').feature('ref2').set('numrefine',
{num2str(refs(2))});
        model.mesh('mesh1').feature('ref3').set('numrefine',
{num2str(refs(3))});

        % run model
        model.sol('sol1').run;

        % integrate the values of interest and write to export file
        inlet=mphint2(model, 'v', 'line', 'selection', boundaries(1));
        plasma=mphint2(model, 'v', 'line', 'selection', boundaries(2));
        outlet=mphint2(model, 'v', 'line', 'selection', boundaries(3));
        fprintf(fid,[num2str(inlet),' | ',num2str(plasma),...
            ' | ',num2str(outlet),' \n']);

    end

    stats = mphmeshstats(model);
    numelem=stats.numelem(2)+stats.numelem(3);

    fprintf(fid, ['Number of mesh elements: ', num2str(numelem), ' \n']);

end

fclose(fid);

end
```

Code for 2 channel potentiostat exporting a text file containing the current values. Code allows for import of multiple files at once for direct comparison between experiments.

```
% main file to deal with CNT sensing data
clc; % clears matlab window
clearvars; % clears any variables that were saved from previous runs

% input the files of interest for data manipulation
% these text files would be added to the full location specified inside
% import function, can add multiple files
filenames={'20140829 Expt2 Tween20CDI and Biotin.txt'};
% these are shorter "names" for the files so it's easier to deal with
fileshorts={'Op1PBSswitch'};

% sometimes initially the device is equilibrating at first
% and we don't want to include the messy data
timestart=[0]; %minutes
```

```
% decide whether you want to add a filter to the data
filterQ=1; % if 1, filter is on; otherwise no filter
secfilter=5; % how many seconds to filter over
% ex. if =5 - average over previous 5 seconds and forward 5 seconds (25 pts
each way)

% baseline correction
baselineQ=1; %1 for yes, 0 for no



% filenames and fileshorts correlate, so it helps to make sure all the
% inputs are complete
if length(filenames) ~= length(fileshorts)
    % if not the same, stop running the program and display the error
    error('Please name each experiment in fileshorts');
end


% import data from each file with the starting point specified above
for i=1:length(filenames) % loop over each file so everything is imported

    % calling the matlab function importfile that's in the same location as
    % this main file
    [time, ch1, ch2]=importfile(filenames{i}, timestart);

    % creating structures to assign each variable, structures allow for
    % different lengths of variables from different experiments
    minutes.(char(fileshorts(i)))=time;
    ch1uamps.(char(fileshorts(i)))=ch1;
    ch2uamps.(char(fileshorts(i)))=ch2;


end


% assigning number of total points for each file
numpts=zeros(1, length(filenames)); %preallocation saves on speed
for i=1:length(filenames)
    numpts(i)=length(minutes.(char(fileshorts(i))));
end


% filtering data if turned on (i.e. =1)
if filterQ == 1

    % data is recorded every 0.2 seconds (5 points/second)
    ptsfilter=secfilter*5; % how many points to average for filtering

    for i=1:length(filenames) % loop over each file

        % handling the first ptsfilter points we have to average from the
        % start (less than -ptsfilter points)
        for j=1:ptsfilter
```

```
ch1filt.(char(fileshorts(i)))(j)=mean(ch1uamps.(char(fileshorts(i)))(1:j+pt
sfilter));

ch2filt.(char(fileshorts(i)))(j)=mean(ch2uamps.(char(fileshorts(i)))(1:j+pt
sfilter));
        end

        % middle section filter
        for j=(ptsfilter+1):numpts(i)-(ptsfilter+1)

ch1filt.(char(fileshorts(i)))(j)=mean(ch1uamps.(char(fileshorts(i)))(j-
ptsfilter:j+ptsfilter));

ch2filt.(char(fileshorts(i)))(j)=mean(ch2uamps.(char(fileshorts(i)))(j-
ptsfilter:j+ptsfilter));
        end

        % for the last ptsfilter points, can only filter until the end of
data
        for j=numpts(i)-ptsfilter:numpts(i)

            ptsleft=numpts(i)-j; % number of points to the end of the array

ch1filt.(char(fileshorts(i)))(j)=mean(ch1uamps.(char(fileshorts(i)))(j-
ptsfilter:j+ptsleft));

ch2filt.(char(fileshorts(i)))(j)=mean(ch2uamps.(char(fileshorts(i)))(j-
ptsfilter:j+ptsleft));

        end


    end

else
    % if did not filter, still need to rename in order to use in later
    % loops so that data is now stored in ch1filt etc
    for i=1:length(filenames)

        ch1filt.(char(fileshorts(i)))=ch1uamps.(char(fileshorts(i)))';
        ch2filt.(char(fileshorts(i)))=ch2uamps.(char(fileshorts(i)))';

    end

end


% calculate -delG/G0 = -(G-G0)/G0
% calculate G0 by taking the average of the first 20 seconds (100 points)
secave=20; % how many seconds to average over
ptsave=secave*5; % converting to number of points collected (every 0.2
seconds)

for i=1:length(filenames) % apply this to every file

    % G0 is calculated by averaging the initial value from 20 seconds
```

```
ch1G0.(char(fileshorts(i)))=mean(ch1filt.(char(fileshorts(i)))(1:ptsave));

ch2G0.(char(fileshorts(i)))=mean(ch2filt.(char(fileshorts(i)))(1:ptsave));

    % calculating -delG/G0
    ch1delG.(char(fileshorts(i)))=-(ch1filt.(char(fileshorts(i)))-
ch1G0.(char(fileshorts(i))))/ch1G0.(char(fileshorts(i)));
    ch2delG.(char(fileshorts(i)))=-(ch2filt.(char(fileshorts(i)))-
ch2G0.(char(fileshorts(i))))/ch2G0.(char(fileshorts(i)));

end


% baseline correction
if baselineQ == 1
    % calculate average points for beginning and ending deltaG values
    for i=1:length(filenames)

        % calculating beginning deltaG values
        ch1Gbeg=mean(ch1delG.(char(fileshorts(i)))((1:ptsave)));
        ch2Gbeg=mean(ch2delG.(char(fileshorts(i)))((1:ptsave)));

        %calculating ending deltaG values
        ch1Gend=mean(ch1delG.(char(fileshorts(i)))((numpts(i)-
ptsave):numpts(i)));
        ch2Gend=mean(ch2delG.(char(fileshorts(i)))((numpts(i)-
ptsave):numpts(i)));

        %calculating slope of deltaG from beginning to end based on pt#
        slopech1=(ch1Gend-ch1Gbeg)/numpts(i);
        slopech2=(ch2Gend-ch2Gbeg)/numpts(i);

        % baseline correction on data based on point number, not time
        % first, calcuating slope-offset for each point
        slopech1offset=zeros(1,numpts(i));
        slopech2offset=zeros(1,numpts(i));

        for j=1:numpts(i)
            slopech1offset(j)=slopech1*j;
            slopech2offset(j)=slopech2*j;
        end

        ch1delGcorr.(char(fileshorts(i)))=ch1delG.(char(fileshorts(i)))-
slopech1offset;
        ch2delGcorr.(char(fileshorts(i)))=ch2delG.(char(fileshorts(i)))-
slopech2offset;
    end

else
    for i=1:length(filenames)

        % even if no baseline correction, need to reassign variables for
plot
        ch1delGcorr.(char(fileshorts(i)))=ch1delG.(char(fileshorts(i)));
        ch2delGcorr.(char(fileshorts(i)))=ch2delG.(char(fileshorts(i)));

    end
```

```
end


% plotting loop
% define plots colors
plotcolors=['b' 'r'; 'm' 'k'; 'y' 'g'];
for i=1:length(filenames)

    plot(minutes.(char(fileshorts(i))), ch1delGcorr.(char(fileshorts(i))),
plotcolors(i,1),...
        minutes.(char(fileshorts(i))), ch2delGcorr.(char(fileshorts(i))),
plotcolors(i,2))
    hold on;
end

ymax=0.04; % manual set of maximum y-axis value plotted
ymin=-0.03; % manual set of minimum y-axis value plotted
time=[0, 9.9, 21.4, 35.9, 55.9]; % times of protein injection
time=time+0.02; %time-offset to account for how long it takes protein to
reach channel
ycoord=-0.028; % y-coordinate where the text will be printed
offset=0.004; % offset between two different text locations
strtext= {'0.01xPBS',  '337nM Avidin', '577nM Avidin','413nM BSA', '748nM
Avidin' }; %concentration fo protein injected

%loop for plotting in order to plot multiple vertical lines and files
for i=1:length(time)
    plot([time(i) time(i)], [ymin ymax], 'k')
    hold on;
end


for i=1:length(time)
    if mod(i,2) == 0
        ycoordnew=ycoord+offset;
    else
        ycoordnew=ycoord;
    end
    text(time(i)+0.5,ycoordnew,strtext(i));
end

title('NSB Sensing 0.01x PBS, 1mm gap, 1%Tween20 30min Soak')
xlabel('Time, minutes')
ylabel('-DelG/G0')
legend('Tween20CDIBiotin CNTs', 'Tween20CDIBiotin CNTs')
% axis([0 50 ymin ymax])
```

importfile.m Function used in the file above:

```
function [minutes, ch1uamps, ch2uamps] = importfile(filename, timestart)
% function to import the text file generated from the experiment
% returns data in variable form
% seconds are converted to minutes
% the electrode readout is converted to microamps
```

```
% specify location of file
filetoread=strcat('C:\Data\ElectroChem\Exported Data\', filename);

ElectroData=importdata(filetoread);

minutestemp=ElectroData.data(:,1)/60; % import minutes from experiment
ch1uampstemp=ElectroData.data(:,2)*10^6; % channel 1 readout, microamps
ch2uampstemp=ElectroData.data(:,4)*10^6; % channel 2 readout, microamps
%


% sometimes channel 2 has 1 less point than channel 1
% and therefore channel 2 imports "NaN" as the last value
% if this occurs, cut all the variables by 1 point
if isnan(ch2uampstemp(length(ch2uampstemp))) %check if last point is NaN

    %assign a 1pt shorter length and re-assign the values
    newlength=length(ch2uampstemp)-1;
    minutestemp=minutestemp(1:newlength);
    ch1uampstemp=ch1uampstemp(1:newlength);
    ch2uampstemp=ch2uampstemp(1:newlength);

end

% sometimes channel 2 has 2 less point than channel 1
% and therefore channel 2 imports "NaN" as the 2 last values
% if this occurs, cut all the variables by another point
if isnan(ch2uampstemp(length(ch2uampstemp))) %check if last point is NaN

    %assign a 1pt shorter length and re-assign the values
    newlength=length(ch2uampstemp)-1;
    minutestemp=minutestemp(1:newlength);
    ch1uampstemp=ch1uampstemp(1:newlength);
    ch2uampstemp=ch2uampstemp(1:newlength);

end


% cutting off any data that's "prefilling", if specified in main file
if timestart ~= 0
    lengthdata=length(minutestemp);
    startingpt=timestart*60*5; % 5 points/second and 60 seconds/minute

    minutes=minutestemp(startingpt:lengthdata);
    ch1uamps=ch1uampstemp(startingpt:lengthdata);
    ch2uamps=ch2uampstemp(startingpt:lengthdata);
else
    minutes=minutestemp;
    ch1uamps=ch1uampstemp;
    ch2uamps=ch2uampstemp;
end

%  size(minutes)
%  size(ch1uamps)
%  size(ch2uamps)

end
```

## REFERENCES


1. Sackmann, E.K., A.L. Fulton, and D.J. Beebe, *The present and future role of microfluidics in biomedical research.* Nature, 2014. **507**(7491): p. 181-189.
2. Jenkins, G. and C.D. Mansfield, *Microfluidic Diagnostics: Methods and Protocols*2013: Humana Press.
3. Whitesides, G.M., *The origins and the future of microfluidics.* Nature, 2006. **442**(7101): p. 368-373.
4. El-Ali, J., P.K. Sorger, and K.F. Jensen, *Cells on chips.* Nature, 2006. **442**(7101): p. 403-411.
5. Yager, P., T. Edwards, E. Fu, K. Helton, K. Nelson, M.R. Tam, and B.H. Weigl, *Microfluidic diagnostic technologies for global public health.* Nature, 2006. **442**(7101): p. 412-418.
6. Gossett, D., W. Weaver, A. Mach, S. Hur, H. Tse, W. Lee, H. Amini, and D. Di Carlo, *Label-free cell separation and sorting in microfluidic systems.* Analytical and Bioanalytical Chemistry, 2010. **397**(8): p. 3249-3267.
7. Yu, Z.T.F., K.M. Aw Yong, and J. Fu, *Microfluidic Blood Cell Sorting: Now and Beyond.* Small, 2014. **10**(9): p. 1687-1703.
8. Kersaudy-Kerhoas, M. and E. Sollier, *Micro-scale blood plasma separation: from acoustophoresis to egg-beaters.* Lab on a Chip, 2013. **13**(17): p. 3323-3346.
9. Peyman, S.A., E.Y. Kwan, O. Margarson, A. Iles, and N. Pamme, *Diamagnetic repulsion - A versatile tool for label-free particle handling in microfluidic devices.* Journal of Chromatography A, 2009. **1216**(52): p. 9055-9062.
10. Boron, W.F. and E.L. Boulpaep, *Medical physiology :a cellular and molecular approach.* 2nd ed. ed2009, Philadelphia: Saunders Elsevier. 1-1337.
11. Rodriguez-Villarreal, A.I., M.D. Tarn, L.A. Madden, J.B. Lutz, J. Greenman, J. Samitier, and N. Pamme, *Flow focussing of particles and cells based on their intrinsic properties using a simple diamagnetic repulsion setup.* Lab on a Chip, 2011. **11**(7): p. 1240-1248.
12. Yung, C.W., J. Fiering, A.J. Mueller, and D.E. Ingber, *Micromagnetic-microfluidic blood cleansing device.* Lab on a Chip, 2009. **9**(9): p. 1171-1177.
13. Melville, D., F. Paul, and S. Roath, *Direct magnetic separation of red cells from whole blood.* Nature, 1975. **255**(5511): p. 706-706.
14. Takayasu, M., D.R. Kelland, and J.V. Minervini, *Continuous magnetic separation of blood components from whole blood.* Applied Superconductivity, IEEE Transactions on, 2000. **10**(1): p. 927-930.
15. Jung, J. and K.-H. Han, *Lateral-driven continuous magnetophoretic separation of blood cells.* Applied Physics Letters, 2008. **93**(22): p. -.
16. Han, K.-H. and A.B. Frazier, *Paramagnetic capture mode magnetophoretic microseparator for high efficiency blood cell separations.* Lab on a Chip, 2006. **6**(2): p. 265-273.
17. Wen, J., E.W. Wilker, M.B. Yaffe, and K.F. Jensen, *Microfluidic Preparative Free-Flow Isoelectric Focusing: System Optimization for Protein Complex Separation.* Analytical Chemistry, 2010. **82**(4): p. 1253-1260.
18. Jiang, H., X. Weng, C.H. Chon, X. Wu, and D. Li, *A microfluidic chip for blood plasma separation using electro-osmotic flow control.* Journal of Micromechanics and Microengineering, 2011. **21**(8): p. 085019.
19. Bruus, H., *Acoustofluidics 1: Governing equations in microfluidics*, in *Lab on a Chip*2011, The Royal Society of Chemistry. p. 3742-3751.

20. Lenshof, A. and T. Laurell, *Continuous separation of cells and particles in microfluidic systems.* Chemical Society Reviews, 2010. **39**(3): p. 1203-1217.
21. Sung, J.S. *Dielectrophoresis and Optoelectronic Tweezers for Nanomanipulation.* http://large.stanford.edu/courses/2007/ph210/sung2/, 2010.
22. Nakashima, Y., S. Hata, and T. Yasuda, *Blood plasma separation and extraction from a minute amount of blood using dielectrophoretic and capillary forces.* Sensors and Actuators B: Chemical, 2010. **145**(1): p. 561-569.
23. Chen, C.-C., P.-H. Lin, and C.-K. Chung, *Microfluidic chip for plasma separation from undiluted human whole blood samples using low voltage contactless dielectrophoresis and capillary force.* Lab on a Chip, 2014. **14**(12): p. 1996-2001.
24. Gascoyne, P.R.C., W. Xiao-Bo, H. Ying, and F.F. Becker, *Dielectrophoretic separation of cancer cells from blood.* Industry Applications, IEEE Transactions on, 1997. **33**(3): p. 670-678.
25. Pommer, M.S., Y. Zhang, N. Keerthi, D. Chen, J.A. Thomson, C.D. Meinhart, and H.T. Soh, *Dielectrophoretic separation of platelets from diluted whole blood in microfluidic channels.* ELECTROPHORESIS, 2008. **29**(6): p. 1213-1218.
26. Zhou, H., L.R. White, and R.D. Tilton, *Lateral separation of colloids or cells by dielectrophoresis augmented by AC electroosmosis.* Journal of Colloid and Interface Science, 2005. **285**(1): p. 179-191.
27. Yan, S., J. Zhang, G. Alici, H. Du, Y. Zhu, and W. Li, *Isolating plasma from blood using a dielectrophoresis-active hydrophoretic device.* Lab on a Chip, 2014. **14**(16): p. 2993-3003.
28. Lenshof, A., A. Ahmad-Tajudin, K. JÃ¤rÃ¥s, A.-M. SwÃ¤rd-Nilsson, L. Ã…berg, G.r. Marko-Varga, J. Malm, H. Lilja, and T. Laurell, *Acoustic Whole Blood Plasmapheresis Chip for Prostate Specific Antigen Microarray Diagnostics.* Analytical Chemistry, 2009. **81**(15): p. 6030-6037.
29. Tajudin, A.A., K. Petersson, A. Lenshof, A.M. Sward-Nilsson, L. Aberg, G. Marko-Varga, J. Malm, H. Lilja, and T. Laurell, *Integrated acoustic immunoaffinity-capture (IAI) platform for detection of PSA from whole blood samples.* Lab on a Chip, 2013. **13**(9): p. 1790-1796.
30. Wiklund, M., *Acoustofluidics 12: Biocompatibility and cell viability in microfluidic acoustic resonators.* Lab on a Chip, 2012. **12**(11): p. 2018-2028.
31. Ding, X., S.-C.S. Lin, B. Kiraly, H. Yue, S. Li, I.-K. Chiang, J. Shi, S.J. Benkovic, and T.J. Huang, *On-chip manipulation of single microparticles, cells, and organisms using surface acoustic waves.* Proceedings of the National Academy of Sciences, 2012. **109**(28): p. 11105-11109.
32. Petersson, F., A. Nilsson, C. Holm, H. Jonsson, and T. Laurell, *Continuous separation of lipid particles from erythrocytes by means of laminar flow and acoustic standing wave forces.* Lab on a Chip, 2005. **5**(1): p. 20-22.
33. Park, J., V. Sunkara, T.-H. Kim, H. Hwang, and Y.-K. Cho, *Lab-on-a-Disc for Fully Integrated Multiplex Immunoassays.* Analytical Chemistry, 2012. **84**(5): p. 2133-2140.
34. Kim, T.-H., H. Hwang, R. Gorkin, M. Madou, and Y.-K. Cho, *Geometry effects on blood separation rate on a rotating disc.* Sensors and Actuators B: Chemical, 2013. **178**(0): p. 648-655.
35. Robert, B., R. Nuno, F. João Garcia da, and D. Jens, *Plasma extraction by centrifugo-pneumatically induced gating of flow.* Journal of Micromechanics and Microengineering, 2013. **23**(3): p. 035035.

36. Lee, B.S., J.-N. Lee, J.-M. Park, J.-G. Lee, S. Kim, Y.-K. Cho, and C. Ko, *A fully automated immunoassay from whole blood on a disc.* Lab on a Chip, 2009. **9**(11): p. 1548-1555.
37. Haeberle, S., T. Brenner, R. Zengerle, and J. Ducree, *Centrifugal extraction of plasma from whole blood on a rotating disk.* Lab on a Chip, 2006. **6**(6): p. 776-781.
38. Gorkin, R., J. Park, J. Siegrist, M. Amasia, B.S. Lee, J.-M. Park, J. Kim, H. Kim, M. Madou, and Y.-K. Cho, *Centrifugal microfluidics for biomedical applications.* Lab on a Chip, 2010. **10**(14): p. 1758-1773.
39. Brigden, M.L., *Clinical utility of the erythrocyte sedimentation rate.* American family physician, 1999. **60**(5): p. 1443-1450.
40. Tachi, T., N. Kaji, M. Tokeshi, and Y. Baba, *Simultaneous Separation, Metering, and Dilution of Plasma from Human Whole Blood in a Microfluidic System.* Analytical Chemistry, 2009. **81**(8): p. 3194-3198.
41. Crowley, T.A. and V. Pizziconi, *Isolation of plasma from whole blood using planar microfilters for lab-on-a-chip applications.* Lab on a Chip, 2005. **5**(9): p. 922-929.
42. Wang, S., D. Sarenac, M.H. Chen, S.-H. Huang, F.F. Giguel, D.R. Kuritzkes, and U. Demirci, *Simple filter microchip for rapid separation of plasma and viruses from whole blood.* International journal of nanomedicine, 2012. **7**: p. 5019.
43. Thorslund, S., O. Klett, F. Nikolajeff, K. Markides, and J. Bergquist, *A hybrid poly(dimethylsiloxane) microsystem for on-chip whole blood filtration optimized for steroid screening.* Biomedical Microdevices, 2006. **8**(1): p. 73-79.
44. Son, J.H., S.H. Lee, S. Hong, S.-m. Park, J. Lee, A.M. Dickey, and L.P. Lee, *Hemolysis-free blood plasma separation.* Lab on a Chip, 2014. **14**(13): p. 2287-2292.
45. VanDelinder, V. and A. Groisman, *Separation of Plasma from Whole Human Blood in a Continuous Cross-Flow in a Molded Microfluidic Device.* Analytical Chemistry, 2006. **78**(11): p. 3765-3771.
46. Aran, K., A. Fok, L.A. Sasso, N. Kamdar, Y. Guan, Q. Sun, A. Undar, and J.D. Zahn, *Microfiltration platform for continuous blood plasma protein extraction from whole blood during cardiac surgery.* Lab on a Chip, 2011. **11**(17): p. 2858-2868.
47. Choi, S., S. Song, C. Choi, and J.-K. Park, *Sheathless Focusing of Microbeads and Blood Cells Based on Hydrophoresis.* Small, 2008. **4**(5): p. 634-641.
48. Davis, J.A., D.W. Inglis, K.J. Morton, D.A. Lawrence, L.R. Huang, S.Y. Chou, J.C. Sturm, and R.H. Austin, *Deterministic hydrodynamics: Taking blood apart.* Proceedings of the National Academy of Sciences, 2006. **103**(40): p. 14779-14784.
49. Deen, W.M., *Analysis of Transport Phenomena (Topics in Chemical Engineering).* Vol. 3. 1998: Oxford University Press, New York.
50. Bird, R.B., W.E. Stewart, and E.N. Lightfoot, *Transport phenomena*2007: John Wiley & Sons.
51. Geislinger, T.M. and T. Franke, *Hydrodynamic lift of vesicles and red blood cells in flow — from Fåhræus & Lindqvist to microfluidic cell sorting.* Advances in Colloid and Interface Science, 2014. **208**(0): p. 161-176.
52. Di Carlo, D., D. Irimia, R.G. Tompkins, and M. Toner, *Continuous inertial focusing, ordering, and separation of particles in microchannels.* Proceedings of the National Academy of Sciences, 2007. **104**(48): p. 18892-18897.
53. Amini, H., W. Lee, and D. Di Carlo, *Inertial microfluidic physics.* Lab on a Chip, 2014. **14**(15): p. 2739-2761.
54. Whittaker, S.R.F. and F.R. Winton, *The apparent viscosity of blood flowing in the isolated hindlimb of the dog, and its variation with corpuscular concentration.* The Journal of Physiology, 1933. **78**(4): p. 339-369.

55. DOYEUX, V., T. PODGORSKI, S. PEPONAS, M. ISMAIL, and G. COUPIER, *Spheres in the vicinity of a bifurcation: elucidating the Zweifach–Fung effect.* Journal of Fluid Mechanics, 2011. **674**: p. 359-388.
56. Yang, S., A. Ündar, and J.D. Zahn, *Blood Plasma Separation in Microfluidic Channels Using Flow Rate Control.* ASAIO Journal, 2005. **51**(5): p. 585-590.
57. Yang, S., A. Undar, and J.D. Zahn, *A microfluidic device for continuous, real time blood plasma separation.* Lab on a Chip, 2006. **6**(7): p. 871-880.
58. Fan, R., O. Vermesh, A. Srivastava, B.K.H. Yen, L. Qin, H. Ahmad, G.A. Kwong, C.-C. Liu, J. Gould, L. Hood, and J.R. Heath, *Integrated barcode chips for rapid, multiplexed analysis of proteins in microliter quantities of blood.* Nat Biotech, 2008. **26**(12): p. 1373-1378.
59. Qin, L., O. Vermesh, Q. Shi, and J.R. Heath, *Self-powered microfluidic chips for multiplexed protein assays from whole blood.* Lab on a Chip, 2009. **9**(14): p. 2016-2020.
60. Jäggi, R., R. Sandoz, and C. Effenhauser, *Microfluidic depletion of red blood cells from whole blood in high-aspect-ratio microchannels.* Microfluidics and Nanofluidics, 2007. **3**(1): p. 47-53.
61. Tripathi, S., A. Prabhakar, N. Kumar, S. Singh, and A. Agrawal, *Blood plasma separation in elevated dimension T-shaped microchannel.* Biomedical Microdevices, 2013. **15**(3): p. 415-425.
62. Kersaudy-Kerhoas, M., R. Dhariwal, M.Y. Desmulliez, and L. Jouvet, *Hydrodynamic blood plasma separation in microfluidic channels.* Microfluidics and Nanofluidics, 2010. **8**(1): p. 105-114.
63. Kersaudy-Kerhoas, M., D.M. Kavanagh, R.S. Dhariwal, C.J. Campbell, and M.P.Y. Desmulliez, *Validation of a blood plasma separation system by biomarker detection.* Lab on a Chip, 2010. **10**(12): p. 1587-1595.
64. Wu, L., G. Guan, H.W. Hou, A.A.S. Bhagat, and J. Han, *Separation of Leukocytes from Blood Using Spiral Channel with Trapezoid Cross-Section.* Analytical Chemistry, 2012. **84**(21): p. 9324-9331.
65. Nivedita, N. and I. Papautsky, *Continuous separation of blood cells in spiral microfluidic devices.* Biomicrofluidics, 2013. **7**(5): p. 054101.
66. Geng, Z., Y. Ju, Q. Wang, W. Wang, and Z. Li, *Multi-component continuous separation chip composed of micropillar arrays in a split-level spiral channel.* RSC Advances, 2013. **3**(34): p. 14798-14806.
67. Browne, A.W., L. Ramasamy, T.P. Cripe, and C.H. Ahn, *A lab-on-a-chip for rapid blood separation and quantification of hematocrit and serum analytes.* Lab on a Chip, 2011. **11**(14): p. 2440-2446.
68. Yang, X., O. Forouzan, T.P. Brown, and S.S. Shevkoplyas, *Integrated separation of blood plasma from whole blood for microfluidic paper-based analytical devices.* Lab on a Chip, 2012. **12**(2): p. 274-280.
69. Vella, S.J., P. Beattie, R. Cademartiri, A. Laromaine, A.W. Martinez, S.T. Phillips, K.A. Mirica, and G.M. Whitesides, *Measuring Markers of Liver Function Using a Micropatterned Paper Device Designed for Blood from a Fingerstick.* Analytical Chemistry, 2012. **84**(6): p. 2883-2891.
70. Songjaroen, T., W. Dungchai, O. Chailapakul, C.S. Henry, and W. Laiwattanapaisal, *Blood separation on microfluidic paper-based analytical devices.* Lab on a Chip, 2012. **12**(18): p. 3392-3398.
71. Kindt, T.J.O., Barbara A.; Goldsby, Richard A., *Immunology*. 6th ed2006: W.H. Freeman and Co.

72. Shin, K.-S., S.W. Lee, K.-C. Han, S.K. Kim, E.K. Yang, J.H. Park, B.-K. Ju, J.Y. Kang, and T.S. Kim, *Amplification of fluorescence with packed beads to enhance the sensitivity of miniaturized detection in microfluidic chip.* Biosensors and Bioelectronics, 2007. **22**(9–10): p. 2261-2267.
73. Ng, A.C., U. Uddayasankar, and A. Wheeler, *Immunoassays in microfluidic systems.* Analytical and Bioanalytical Chemistry, 2010. **397**(3): p. 991-1007.
74. Qureshi, A., Y. Gurbuz, and J.H. Niazi, *Biosensors for cardiac biomarkers detection: A review.* Sensors and Actuators B: Chemical, 2012. **171–172**(0): p. 62-76.
75. Badu-Tawiah, A.K., S. Lathwal, K. Kaastrup, M. Al-Sayah, D.C. Christodouleas, B.S. Smith, G.M. Whitesides, and H.D. Sikes, *Polymerization-based signal amplification for paper-based immunoassays.* Lab on a Chip, 2015. **15**(3): p. 655-659.
76. McGeough, C.M. and S. O'Driscoll, *Camera Phone-Based Quantitative Analysis of C-Reactive Protein ELISA.* Biomedical Circuits and Systems, IEEE Transactions on, 2013. **7**(5): p. 655-659.
77. Vashist, S.K., T. van Oordt, E.M. Schneider, R. Zengerle, F. von Stetten, and J.H.T. Luong, *A smartphone-based colorimetric reader for bioanalytical applications using the screen-based bottom illumination provided by gadgets.* Biosensors and Bioelectronics, 2015. **67**(0): p. 248-255.
78. Breslauer, D.N., R.N. Maamari, N.A. Switz, W.A. Lam, and D.A. Fletcher, *Mobile Phone Based Clinical Microscopy for Global Health Applications.* PLoS ONE, 2009. **4**(7): p. e6320.
79. Zhu, H., S. Mavandadi, A.F. Coskun, O. Yaglidere, and A. Ozcan, *Optofluidic Fluorescent Imaging Cytometry on a Cell Phone.* Analytical Chemistry, 2011. **83**(17): p. 6641-6647.
80. Cetin, A.E., A.F. Coskun, B.C. Galarreta, M. Huang, D. Herman, A. Ozcan, and H. Altug, *Handheld high-throughput plasmonic biosensor using computational on-chip imaging.* Light Sci Appl, 2014. **3**: p. e122.
81. Ozcan, A., *Mobile phones democratize and cultivate next-generation imaging, diagnostics and measurement tools.* Lab on a Chip, 2014. **14**(17): p. 3187-3194.
82. Rajendran, V., P. Bakthavathsalam, and B. Jaffar Ali, *Smartphone based bacterial detection using biofunctionalized fluorescent nanoparticles.* Microchimica Acta, 2014. **181**(15-16): p. 1815-1821.
83. Balsam, J., H.A. Bruck, and A. Rasooly, *Capillary array waveguide amplified fluorescence detector for mHealth.* Sensors and Actuators B: Chemical, 2013. **186**(0): p. 711-717.
84. Vashist, S.K., G. Czilwik, T. van Oordt, F. von Stetten, R. Zengerle, E. Marion Schneider, and J.H.T. Luong, *One-step kinetics-based immunoassay for the highly sensitive detection of C-reactive protein in less than 30 min.* Analytical Biochemistry, 2014. **456**(0): p. 32-37.
85. Patolsky, F., G. Zheng, and C.M. Lieber, *Fabrication of silicon nanowire devices for ultrasensitive, label-free, real-time detection of biological and chemical species.* Nat. Protocols, 2006. **1**(4): p. 1711-1724.
86. Patolsky, F., B.P. Timko, G. Zheng, and C.M. Lieber, *Nanowire-Based Nanoelectronic Devices in the Life Sciences.* MRS Bulletin, 2007. **32**(02): p. 142-149.
87. Zheng, G., F. Patolsky, Y. Cui, W.U. Wang, and C.M. Lieber, *Multiplexed electrical detection of cancer markers with nanowire sensor arrays.* Nat Biotech, 2005. **23**(10): p. 1294-1301.
88. Maehashi, K., T. Katsura, K. Kerman, Y. Takamura, K. Matsumoto, and E. Tamiya, *Label-Free Protein Biosensor Based on Aptamer-Modified Carbon Nanotube Field-Effect Transistors.* Analytical Chemistry, 2007. **79**(2): p. 782-787.

89. Makowski, M.S. and A. Ivanisevic, *Molecular Analysis of Blood with Micro-/Nanoscale Field-Effect-Transistor Biosensors.* Small, 2011. **7**(14): p. 1863-1875.
90. Balasubramanian, K. and K. Kern, *25th Anniversary Article: Label-Free Electrical Biodetection Using Carbon Nanostructures.* Advanced Materials, 2014. **26**(8): p. 1154-1175.
91. Allen, B.L., P.D. Kichambare, and A. Star, *Carbon Nanotube Field-Effect-Transistor-Based Biosensors.* Advanced Materials, 2007. **19**(11): p. 1439-1451.
92. Li, J., H. Ng, and H. Chen, *Carbon Nanotubes and Nanowires for Biological Sensing*, in *Protein Nanotechnology*, T. Vo-Dinh, Editor 2005, Humana Press. p. 191-223.
93. Balasubramanian, K. and M. Burghard, *Biosensors based on carbon nanotubes.* Analytical and Bioanalytical Chemistry, 2006. **385**(3): p. 452-468.
94. Lieber, C.M. and Z.L. Wang, *Functional Nanowires.* MRS Bulletin, 2007. **32**(02): p. 99-108.
95. Lee, H.-S., K.S. Kim, C.-J. Kim, S.K. Hahn, and M.-H. Jo, *Electrical detection of VEGFs for cancer diagnoses using anti-vascular endotherial growth factor aptamer-modified Si nanowire FETs.* Biosensors and Bioelectronics, 2009. **24**(6): p. 1801-1805.
96. Wang, J., *Carbon-Nanotube Based Electrochemical Biosensors: A Review.* Electroanalysis, 2005. **17**(1): p. 7-14.
97. Timko, B.P., T. Cohen-Karni, Q. Quan, T. Bozhi, and C.M. Lieber, *Design and Implementation of Functional Nanoelectronic Interfaces With Biomolecules, Cells, and Tissue Using Nanowire Device Arrays.* Nanotechnology, IEEE Transactions on, 2010. **9**(3): p. 269-280.
98. Chen, R.J., S. Bangsaruntip, K.A. Drouvalakis, N. Wong Shi Kam, M. Shim, Y. Li, W. Kim, P.J. Utz, and H. Dai, *Noncovalent functionalization of carbon nanotubes for highly specific electronic biosensors.* Proceedings of the National Academy of Sciences, 2003. **100**(9): p. 4984-4989.
99. Alexander, T., H. Kyle, S.F. Michael, P. Makarand, and B. Paola, *A photolithographic process for fabrication of devices with isolated single-walled carbon nanotubes.* Nanotechnology, 2004. **15**(11): p. 1475.
100. McNicholas, T.P., K. Zhao, C. Yang, S.C. Hernandez, A. Mulchandani, N.V. Myung, and M.A. Deshusses, *Sensitive Detection of Elemental Mercury Vapor by Gold-Nanoparticle-Decorated Carbon Nanotube Sensors.* The Journal of Physical Chemistry C, 2011. **115**(28): p. 13927-13931.
101. Weizmann, Y., D.M. Chenoweth, and T.M. Swager, *DNA−CNT Nanowire Networks for DNA Detection.* Journal of the American Chemical Society, 2011. **133**(10): p. 3238-3241.
102. Mirica, K.A., J.G. Weis, J.M. Schnorr, B. Esser, and T.M. Swager, *Mechanical Drawing of Gas Sensors on Paper.* Angewandte Chemie International Edition, 2012. **51**(43): p. 10740-10745.
103. Mirica, K.A., J.M. Azzarelli, J.G. Weis, J.M. Schnorr, and T.M. Swager, *Rapid prototyping of carbon-based chemiresistive gas sensors on paper.* Proceedings of the National Academy of Sciences, 2013. **110**(35): p. E3265-E3270.
104. Heinze, S., J. Tersoff, R. Martel, V. Derycke, J. Appenzeller, and P. Avouris, *Carbon Nanotubes as Schottky Barrier Transistors.* Physical Review Letters, 2002. **89**(10): p. 106801.
105. Balasubramanian, K., M. Burghard, K. Kern, M. Scolari, and A. Mews, *Photocurrent Imaging of Charge Transport Barriers in Carbon Nanotube Devices.* Nano Letters, 2005. **5**(3): p. 507-510.

106. Chen, R.J., H.C. Choi, S. Bangsaruntip, E. Yenilmez, X. Tang, Q. Wang, Y.-L. Chang, and H. Dai, *An Investigation of the Mechanisms of Electronic Sensing of Protein Adsorption on Carbon Nanotube Devices.* Journal of the American Chemical Society, 2004. **126**(5): p. 1563-1568.
107. Fu, Q. and J. Liu, *Integrated Single-Walled Carbon Nanotube/Microfluidic Devices for the Study of the Sensing Mechanism of Nanotube Sensors.* The Journal of Physical Chemistry B, 2005. **109**(28): p. 13406-13408.
108. Kenis, P.J.A., R.F. Ismagilov, S. Takayama, G.M. Whitesides, S. Li, and H.S. White, *Fabrication inside Microchannels Using Fluid Flow.* Accounts of Chemical Research, 2000. **33**(12): p. 841-847.
109. Gao, Y. and L. Chen, *Versatile control of multiphase laminar flow for in-channel microfabrication.* Lab on a Chip, 2008. **8**(10): p. 1695-1699.
110. Kamholz, A.E., B.H. Weigl, B.A. Finlayson, and P. Yager, *Quantitative Analysis of Molecular Interaction in a Microfluidic Channel: The T-Sensor.* Analytical Chemistry, 1999. **71**(23): p. 5340-5347.
111. Hofmann, O., G. Voirin, P. Niedermann, and A. Manz, *Three-Dimensional Microfluidic Confinement for Efficient Sample Delivery to Biosensor Surfaces. Application to Immunoassays on Planar Optical Waveguides.* Analytical Chemistry, 2002. **74**(20): p. 5243-5250.
112. Kim, J.P., B.Y. Lee, J. Lee, S. Hong, and S.J. Sim, *Enhancement of sensitivity and specificity by surface modification of carbon nanotubes in diagnosis of prostate cancer based on carbon nanotube field effect transistors.* Biosensors and Bioelectronics, 2009. **24**(11): p. 3372-3378.
113. Chen, R.J., Y. Zhang, D. Wang, and H. Dai, *Noncovalent sidewall functionalization of single-walled carbon nanotubes for protein immobilization.* Journal of the American Chemical Society, 2001. **123**(16): p. 3838-3839.
114. Chi, Y.S., H.R. Byon, H.C. Choi, and I.S. Choi, *A Noncovalent Approach to the Construction of Tween 20-Based Protein Microarrays.* ChemBioChem, 2007. **8**(12): p. 1380-1387.
115. Wu, Z. and K. Hjort, *Surface modification of PDMS by gradient-induced migration of embedded Pluronic.* Lab on a Chip, 2009. **9**(11): p. 1500-1503.
116. Reinke, W., P. Gaehtgens, and P.C. Johnson, *Blood viscosity in small tubes: effect of shear rate, aggregation, and sedimentation.* Vol. 253. 1987. H540-H547.
117. Goldsmith, H.L., G.R. Cokelet, and P. Gaehtgens, *Robin Fahraeus: evolution of his concepts in cardiovascular physiology.* Vol. 257. 1989. H1005-H1015.
118. Pries, A.R., D. Neuhaus, and P. Gaehtgens, *Blood viscosity in tube flow: dependence on diameter and hematocrit.* Vol. 263. 1992. H1770-H1778.
119. Baskurt, O.K. and H.J. Meiselman. *Blood rheology and hemodynamics.* in *Seminars in thrombosis and hemostasis.* 2003. New York: Stratton Intercontinental Medical Book Corporation, c1974-.
120. Park, J.-S., S.-H. Song, and H.-I. Jung, *Continuous focusing of microparticles using inertial lift force and vorticity via multi-orifice microfluidic channels.* Lab on a Chip, 2009. **9**(7): p. 939-948.
121. Mayer, G.A. and O. Kiss, *Blood viscosity and in vitro anticoagulants.* Vol. 208. 1965. 795-797.
122. Jain, A. and L.L. Munn, *Biomimetic postcapillary expansions for enhancing rare blood cell separation on a microfluidic chip.* Lab on a Chip, 2011. **11**(17): p. 2941-2947.

123. Beebe, D.J., G.A. Mensing, and G.M. Walker, *PHYSICS AND APPLICATIONS OF MICROFLUIDICS IN BIOLOGY.* Annual Review of Biomedical Engineering, 2002. **4**(1): p. 261-286.
124. Perry, R.H., D.W. Green, J.O. Maloney, M.M. Abbott, C.M. Ambler, and R.C. Amero, *Perry's chemical engineers' handbook.* Vol. 7. 1997: McGraw-hill New York.
125. Sowemimo-Coker, S.O., *Red blood cell hemolysis during processing.* Transfusion medicine reviews, 2002. **16**(1): p. 46-60.
126. Cripps, C.M., *Rapid method for the estimation of plasma haemoglobin levels.* Journal of Clinical Pathology, 1968. **21**(1): p. 110-112.
127. Malinauskas, R.A., *Plasma Hemoglobin Measurement Techniques for the In Vitro Evaluation of Blood Damage Caused by Medical Devices.* Artificial Organs, 1997. **21**(12): p. 1255-1267.
128. Han, V., K. Serrano, and D.V. Devine, *A comparative study of common techniques used to measure haemolysis in stored red cell concentrates.* Vox Sanguinis, 2010. **98**(2): p. 116-123.
129. Spagnolie, S.E., A. Kumar, and M.D. Graham, *Complex Fluids in Biological Systems. Ch 11: Cell Distribution and Segregation Phenomena During Blood Flow*2014: Springer.
130. Kumar, A., R.G. Henríquez Rivera, and M.D. Graham, *Flow-induced segregation in confined multicomponent suspensions: effects of particle size and rigidity.* Journal of Fluid Mechanics, 2014. **738**: p. 423-462.
131. Brust, M., C. Schaefer, R. Doerr, L. Pan, M. Garcia, P.E. Arratia, and C. Wagner, *Rheology of Human Blood Plasma: Viscoelastic Versus Newtonian Behavior.* Physical Review Letters, 2013. **110**(7): p. 078305.
132. Neu, B. and H.J. Meiselman, *Depletion-Mediated Red Blood Cell Aggregation in Polymer Solutions.* Biophysical Journal, 2002. **83**(5): p. 2482-2490.
133. Fabry, T., *Mechanism of erythrocyte aggregation and sedimentation.* Vol. 70. 1987. 1572-1576.
134. Xu, D., E. Kaliviotis, A. Munjiza, E. Avital, C. Ji, and J. Williams, *Large scale simulation of red blood cell aggregation in shear flows.* Journal of Biomechanics, 2013. **46**(11): p. 1810-1817.
135. Bagchi, P., *Mesoscale Simulation of Blood Flow in Small Vessels.* Biophysical Journal, 2007. **92**(6): p. 1858-1877.
136. Chesnutt, J.K.W. and J.S. Marshall, *Effect of particle collisions and aggregation on red blood cell passage through a bifurcation.* Microvascular Research, 2009. **78**(3): p. 301-313.
137. Liu, Y. and W.K. Liu, *Rheology of red blood cell aggregation by computer simulation.* Journal of Computational Physics, 2006. **220**(1): p. 139-154.
138. Dupin, M.M., I. Halliday, C.M. Care, and L.L. Munn, *Lattice Boltzmann modelling of blood cell dynamics.* International Journal of Computational Fluid Dynamics, 2008. **22**(7): p. 481-492.
139. Zhao, H., E.S.G. Shaqfeh, and V. Narsimhan, *Shear-induced particle migration and margination in a cellular suspension.* Physics of Fluids (1994-present), 2012. **24**(1): p. 011902.
140. Narsimhan, V., H. Zhao, and E.S.G. Shaqfeh, *Coarse-grained theory to predict the concentration distribution of red blood cells in wall-bounded Couette flow at zero Reynolds number.* Physics of Fluids (1994-present), 2013. **25**(6): p. 061901.
141. Pranay, P., R.G. Henríquez-Rivera, and M.D. Graham, *Depletion layer formation in suspensions of elastic capsules in Newtonian and viscoelastic fluids.* Physics of Fluids (1994-present), 2012. **24**(6): p. 061902.

142. Baskurt, O.K. and H.J. Meiselman, *Blood Rheology and Hemodynamics.* Semin Thromb Hemost, 2003. **29**(05): p. 435-450.
143. Johnston, B.M., P.R. Johnston, S. Corney, and D. Kilpatrick, *Non-Newtonian blood flow in human right coronary arteries: steady state simulations.* Journal of Biomechanics, 2004. **37**(5): p. 709-720.
144. Siebert, M.W. and P.S. Fodor. *Newtonian and non-newtonian blood flow over a backward-facing step–a case study.* in *Proceedings of the COMSOL Conference, Boston*. 2009.
145. Balsam, J., H.A. Bruck, and A. Rasooly, *Capillary Array Waveguide Amplified Fluorescence Detector for mHealth.* Sensors and actuators. B, Chemical, 2013. **186**: p. 711-717.
146. Gibbs, J. and M. Kennebunk, *Selecting the detection system—colorimetric, fluorescent, luminescent methods.* http://csmedia2.corning.com/LifeSciences/media/pdf/elisa5.pdf.
147. Dondorp, A.M., V. Desakorn, W. Pongtavornpinyo, D. Sahassananda, K. Silamut, K. Chotivanich, P.N. Newton, P. Pitisuttithum, A.M. Smithyman, N.J. White, and N.P.J. Day, *Estimation of the Total Parasite Biomass in Acute Falciparum Malaria from Plasma PfHRP2.* PLoS Med, 2005. **2**(8): p. e204.
148. Katz, E. and I. Willner, *Biomolecule-Functionalized Carbon Nanotubes: Applications in Nanobioelectronics.* ChemPhysChem, 2004. **5**(8): p. 1084-1104.
149. Salehi-Khojin, A., F. Khalili-Araghi, M.A. Kuroda, K.Y. Lin, J.-P. Leburton, and R.I. Masel, *On the Sensing Mechanism in Carbon Nanotube Chemiresistors.* ACS Nano, 2011. **5**(1): p. 153-158.
150. Robinson, J.A., E.S. Snow, Ş.C. Bădescu, T.L. Reinecke, and F.K. Perkins, *Role of Defects in Single-Walled Carbon Nanotube Chemical Sensors.* Nano Letters, 2006. **6**(8): p. 1747-1751.
151. Bilitewski, U., *Protein-sensing assay formats and devices.* Analytica Chimica Acta, 2006. **568**(1–2): p. 232-247.
152. So, H.-M., D.-W. Park, H. Chang, and J.-O. Lee, *Carbon Nanotube Biosensors with Aptamers as Molecular Recognition Elements*, in *Carbon Nanotubes*, K. Balasubramanian and M. Burghard, Editors. 2010, Humana Press. p. 239-249.
153. Heimer, B.W., T.A. Shatova, J.K. Lee, K. Kaastrup, and H.D. Sikes, *Evaluating the sensitivity of hybridization-based epigenotyping using a methyl binding domain protein.* Analyst, 2014. **139**(15): p. 3695-3701.
154. Kaastrup, K., L. Chan, and H.D. Sikes, *Impact of Dissociation Constant on the Detection Sensitivity of Polymerization-Based Signal Amplification Reactions.* Analytical Chemistry, 2013. **85**(17): p. 8055-8060.
155. Lee, H.H., J. Smoot, Z. McMurray, D.A. Stahl, and P. Yager, *Recirculating flow accelerates DNA microarray hybridization in a microfluidic device.* Lab on a Chip, 2006. **6**(9): p. 1163-1170.
156. Liu, J., B.A. Williams, R.M. Gwirtz, B.J. Wold, and S. Quake, *Enhanced Signals and Fast Nucleic Acid Hybridization By Microfluidic Chaotic Mixing.* Angewandte Chemie International Edition, 2006. **45**(22): p. 3618-3623.
157. Liu, R.H., R. Lenigk, R.L. Druyor-Sanchez, J. Yang, and P. Grodzinski, *Hybridization Enhancement Using Cavitation Microstreaming.* Analytical Chemistry, 2003. **75**(8): p. 1911-1917.
158. Lee, C.Y., W. Choi, J.-H. Han, and M.S. Strano, *Coherence Resonance in a Single-Walled Carbon Nanotube Ion Channel.* Science, 2010. **329**(5997): p. 1320-1324.
159. Choi, W., C.Y. Lee, M.-H. Ham, S. Shimizu, and M.S. Strano, *Dynamics of Simultaneous, Single Ion Transport through Two Single-Walled Carbon Nanotubes:*

*Observation of a Three-State System.* Journal of the American Chemical Society, 2011. **133**(2): p. 203-205.
160. Hua, F., Y. Sun, A. Gaur, M.A. Meitl, L. Bilhaut, L. Rotkina, J. Wang, P. Geil, M. Shim, J.A. Rogers, and A. Shim, *Polymer Imprint Lithography with Molecular-Scale Resolution.* Nano Letters, 2004. **4**(12): p. 2467-2471.
161. Feng, H., A. Gaur, Y. Sun, M. Word, J. Niu, I. Adesida, M. Shim, A. Shim, and J.A. Rogers, *Processing dependent behavior of soft imprint lithography on the 1-10-nm scale.* Nanotechnology, IEEE Transactions on, 2006. **5**(3): p. 301-308.
162. Huo, F., Z. Zheng, G. Zheng, L.R. Giam, H. Zhang, and C.A. Mirkin, *Polymer Pen Lithography.* Science, 2008. **321**(5896): p. 1658-1660.
163. Qin, D., Y. Xia, and G.M. Whitesides, *Soft lithography for micro- and nanoscale patterning.* Nat. Protocols, 2010. **5**(3): p. 491-502.
164. Lochovsky, C., S. Yasotharan, and A. Gunther, *Bubbles no more: in-plane trapping and removal of bubbles in microfluidic devices.* Lab on a Chip, 2012. **12**(3): p. 595-601.
165. Duffy, D.C., J.C. McDonald, O.J.A. Schueller, and G.M. Whitesides, *Rapid Prototyping of Microfluidic Systems in Poly(dimethylsiloxane).* Analytical Chemistry, 1998. **70**(23): p. 4974-4984.
166. MicroChem, C. *SU-8 2000 Permanent Epoxy Negative Photoresist PROCESSING GUIDELINES.* Available from: http://microchem.com/pdf/SU-82000DataSheet2025thru2075Ver4.pdf.
167. TRL, M.M. *EV1 Standard Operating Procedure*. Available from: http://www-mtl.mit.edu/services/fabrication/sops/ev1.html.
168. Corning, D. *SYLGARD® 184 SILICONE ELASTOMER KIT.*
169. Shrirao, A. and R. Perez-Castillejos, *Simple fabrication of microfluidic devices by replicating Scotch-tape masters.* Lab Chip. Chips & Tips, 2010.
170. Mark, A.E., A.J. Michael, and K.G. Bruce, *Determining the optimal PDMS–PDMS bonding technique for microfluidic devices.* Journal of Micromechanics and Microengineering, 2008. **18**(6): p. 067001.
171. Li, P., R. Narayanan, A.J. Sherry, J.A. Cortes, A. Marchesseault, C. Anagnostopoulos, and M. Faghri. *A Blocking-free Microfluidic Fluorescence Heterogeneous Immunoassay for Quantitative Detection of Human C-Reactive Protein*. in *ASME 2009 International Mechanical Engineering Congress and Exposition*. 2009. American Society of Mechanical Engineers.
172. Li, P., A. Sherry, J. Cortes, C. Anagnostopoulos, and M. Faghri, *A blocking-free microfluidic fluorescence heterogeneous immunoassay for point-of-care diagnostics.* Biomedical Microdevices, 2011. **13**(3): p. 475-483.
173. Lu, Y., W. Shi, J. Qin, and B. Lin, *Fabrication and Characterization of Paper-Based Microfluidics Prepared in Nitrocellulose Membrane By Wax Printing.* Analytical Chemistry, 2010. **82**(1): p. 329-335.
174. Dungchai, W., O. Chailapakul, and C.S. Henry, *A low-cost, simple, and rapid fabrication method for paper-based microfluidics using wax screen-printing.* Analyst, 2011. **136**(1): p. 77-82.